Check for updates

# Insights into N2O decomposition in environmental catalysis: evaluation and an advanced outlook

Khezina Rafiq, [ID] [a] Mamoona Sabir, [a] Iqra Sadia, [a] Muhammad Zeeshan Abid, [ID] [a] Muhammad Arif Nadeem [ID] [b] and Ejaz Hussain [ID] *[ab]

Nitrous oxide (N2O) is a potent greenhouse gas and a significant contributor to stratospheric ozone depletion. Its emission arises from a combination of natural and anthropogenic sources, including microbial processes such as nitrification, denitrification, nitrifier denitrification and abiotic chemical pathways such as chemodenitrification and hydroxylamine oxidation. Effective decomposition of N2O into harmless nitrogen and oxygen is therefore critical for climate mitigation. This review provides a comprehensive overview of the current state of N2O decomposition, with a focus on mechanisms, catalyst composition and material design strategies. Catalysts are systematically classified based on their decomposition pathways *i.e.* direct catalytic decomposition (DCD), selective catalytic reduction (SCR), and surface-mediated redox processes. In addition, they are further classified on the basis of their compositional attributes, encompassing both precious as well as and non-precious metal-based catalysts systems. Furthermore, a progress-based classification is presented, encompassing classical metal oxides, spinel oxides, layered double hydroxides, MXenes, and metal–organic frameworks (MOFs). Emerging systems such as antenna-reactor catalysts and quantum dots have also been discussed based on their unique properties and potential. Mechanistic insights into N2O activation, including thermal, surface-catalysed, Mars–van Krevelen-type redox, radical and photocatalytic pathways, are explored in depth. This review highlights the significance of catalyst design, oxygen vacancy engineering and atomically dispersed active sites in enhancing activity and selectivity. Future perspectives emphasize the development of low-cost, thermally stable and environmentally benign catalysts, along with gaining a mechanistic understanding through *in situ* studies and computational modelling. This review aims to guide the rational design of next-generation catalysts for efficient N2O abatement across industrial and environmental systems.

## 1. Introduction

Climate change has become a challenge to international agencies such as the WHO, EPA, IPCC (Intergovernmental Panel on Climate Change), AFED (Arab Forum for Environment and Development), APAN (Asian Pacific Adaptation Network), CCCCC (Caribbean Community Climate Change Centre), CAN (Climate Action Network), CCL (Citizens' Climate Lobby), CJA (Climate Justice Alliance), EDF (Environmental Defense Fund, USA), HEA (Health and Environmental Alliance) and NRDC (Natural Resources Defense Council).[1] For a long time, nitrous oxide (N2O) was not considered a significant environmental pollutant, and it did not receive much attention from an environmental perspective. In recent decades, N2O has been recognized as a potent greenhouse gas. It contributes to the greenhouse effect by trapping the heat in Earth's atmosphere

and leading to global warming. In addition, it is believed to play a role in the destruction of ozone in the stratosphere, contributing to ozone layer depletion.[2] The presence of N2O in the atmosphere causes acid rain, which can have detrimental effects on the ecosystem and environment. Moreover, N2O raises a particular concern due to its long atmospheric lifetime, estimated at approximately 120 years. This means that once released into the atmosphere, it persists for a very long time.[3] The global warming potential (GWP) of N2O is nearly 310 times that of carbon dioxide (CO2). This high GWP makes it a significant contributor to climate change.[4] Chemical industries, especially those involving processes such as nitric acid production and the industrial synthesis of adipic acid, are major sources of anthropogenic N2O emissions. Specifically, in the synthesis of adipic acid, N2O is produced when a cyclohexanone/cyclohexanol mixture reacts with nitric acid. It is noted that N2O emissions from the adipic acid industry contribute a substantial percentage (5–8%) to anthropogenic sources of N2O in the atmosphere.[5,6] Both natural and anthropogenic sources of N2O exist, with industrial sources responsible for emitting a significant amount (400–500 kt) annually.[7]

*[a] Institute of Chemistry, Inorganic Materials Laboratory 52S, The Islamia University of Bahawalpur, 63100, Pakistan. E-mail: ejaz.hussain@iub.edu.pk, khezina.rafiq@iub.edu.pk*

*[b] Catalysis and Nanomaterials Lab 27, Department of Chemistry, Quaid-i-Azam University, Islamabad 45320, Pakistan*

# 2. N$_2$O generation mechanisms

N$_2$O is generated through multiple pathways, primarily mediated by microbial processes, and also *via* abiotic chemical reactions. Key mechanisms include nitrification, where ammonia is oxidized and N$_2$O is formed as a by-product, and denitrification, where nitrate is reduced to nitrogen gases, often realising N$_2$O when the process in incomplete. Nitrifier denitrification also plays a role under oxygen-limiting conditions, while abiotic chemical reactions, such as nitrate reduction by iron or manganese, contribute to additional N$_2$O fluxes. On top of natural processes, human activities significantly amplify these emissions, particularly through intensive agriculture, wastewater management and industrial processes. Different mechanisms are summarized in this section, shown in Fig. 1.

## 2.1. Nitrification

Nitrification is an aerobic microbial process where ammonium (NH$_4^+$) or ammonia (NH$_3$) is oxidized to nitrate (NO$_3^-$) *via* nitrite (NO$_2^-$). This process is mediated by ammonia-oxidizing archaea (AOA), as well as nitrate-oxidizing bacteria (NOB) in a two-step sequence. The oxidation of hydroxylamine (NH$_2$OH), a key intermediate, can inadvertently release N$_2$O as a by-product. N$_2$O production during nitrification is particularly pronounced under suboptimal oxygen conditions, low pH, or high substrate (ammonia) availability, which destabilize the electron transport chain in AOB. Moreover, recent studies have suggested that AOA contribute significantly to N$_2$O emissions in acidic soils, where bacterial nitrification is less efficient. Thus, nitrification represents both a fundamental nitrogen cycle process and a critical source of N$_2$O in agricultural and natural soils.[8]

## 2.2. Denitrification

Denitrification is an anaerobic respiratory process in which nitrate (NO$_3^-$) is sequentially reduced to nitrite (NO$_2^-$), nitric oxide (NO), nitrous oxide (N$_2$O) and finally dinitrogen gas (N$_2$). This pathway is primarily driven by facultative anaerobic bacteria such as *Pseudomonas*, *Paracoccus*, and *Bacillus* species under low-oxygen or anoxic conditions. The process requires organic carbon as an electron donor, linking it closely to carbon cycling. The accumulation of N$_2$O often occurs when the enzyme nitrous oxide reductase (NosZ), responsible for reducing N$_2$O to N$_2$, is inhibited by low pH, low copper availability, or the presence of oxygen. As a result, soils and sediments under fluctuating oxygen conditions, such as wetlands, wastewater systems, and agricultural fields after irrigation, often exhibit high N$_2$O fluxes. Denitrification is considered the largest single biological source of N$_2$O globally.[9]

## 2.3. Nitrifier denitrification

Nitrifier denitrification is a hybrid pathway in which nitrifying organisms, under oxygen-limited or microaerophilic conditions, reduce nitrite (NO$_2^-$) to nitric oxide (NO), nitrous oxide (N$_2$O) and nitrogen gas (N$_2$). Unlike conventional denitrification carried out by facultative anaerobes, this process is mediated by ammonia-oxidizing bacteria (AOB). The pathway is particularly relevant in soils, sediments, and wastewater treatment systems where oxygen availability fluctuates. Nitrifier denitrification can account for substantial N$_2$O emissions when ammonia and nitrite are both abundant, such as in fertilized agricultural soils. It provides a mechanistic link between nitrification and denitrification, highlighting the versatility of microbial nitrogen metabolism under transitional redox conditions.[8]
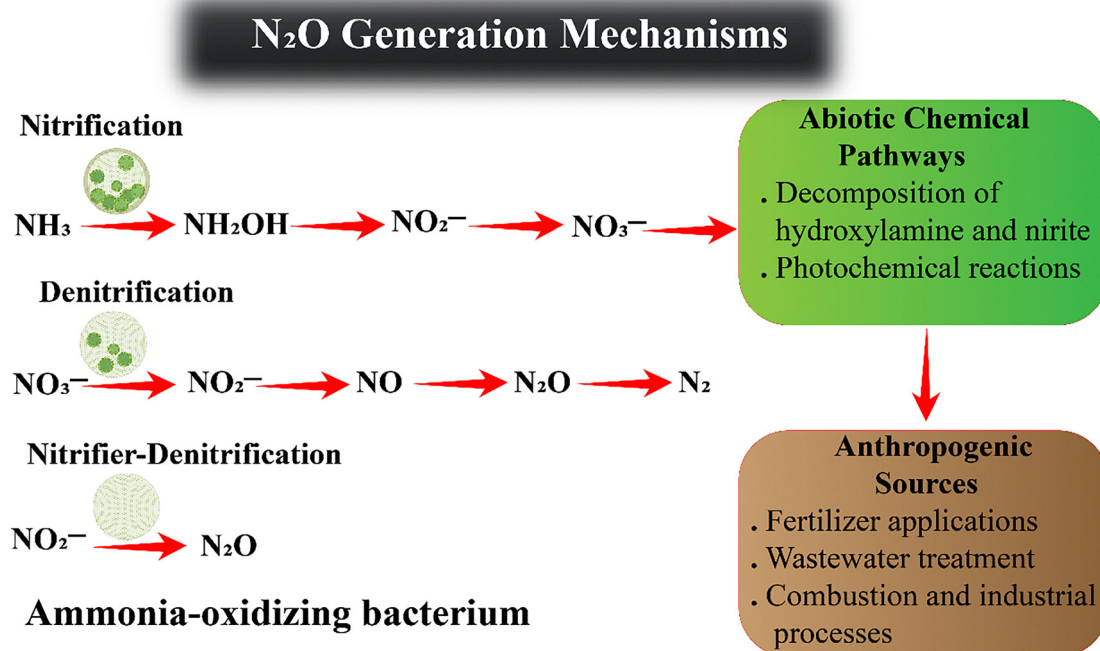


**Fig. 1** Key mechanisms of N$_2$O generation.

## 2.4. Abiotic chemical pathways

Although microbial processes dominate, abiotic pathways also contribute to $N_2O$ formation. These include: (i) chemodenitrification: it involves the reduction of nitrites by ferrous ions ($Fe^{2+}$) or other reductants, leading to $N_2O$ release. This mechanism is common in waterlogged soils, sediments and mining-impacted environments with high levels of reduced metals. (ii) Oxidation of hydroxylamine can occur through reactions with metal oxides, particularly ferric ($Fe^{3+}$) and manganese ($Mn^{4+}$) oxides, producing $N_2O$ and NO. Additionally, photochemical reactions in sunlit waters and soils have been reported to drive abiotic $N_2O$ formation from nitrite. While biotic pathways may represent a smaller fraction globally, they can dominate under specific geochemical conditions, especially in soils rich in iron or manganese.[10]

## 2.5. Anthropogenic sources

Human activities have amplified $N_2O$ emissions far beyond natural background levels. These include (i) agriculture: excessive application of nitrogen-based fertilizers (urea, ammonium nitrate) and livestock manure leads to surplus reactive nitrogen in soils, fueling nitrification, denitrification and nitrifier denitrification. Agricultural soils are estimated to contribute more than 60% of global anthropogenic $N_2O$ emissions. (ii) Wastewater treatment: biological nitrogen removal processes, particularly in activated sludge and sequencing batch reactors, release $N_2O$ due to incomplete nitrification and denitrification under variable oxygen conditions. Emerging evidence shows that wastewater plants may be hotspots of $N_2O$ release if not properly managed. (iii) Industrial processes: $N_2O$ is also released during the production of nitric acid (used in fertilizers) and adipic acid (used in nylon manufacture). Though mitigation technologies exist, incomplete adoption leads to continued emissions. (iv) Biomass burning and fossil fuel combustion: smaller but notable contributions come from burning crop residues, forests, and fossil fuels, releasing reactive nitrogen that indirectly contributes to $N_2O$ formation. Together, these anthropogenic sources have increased atmospheric $N_2O$ concentrations to record highs, making it the third most important long-lived greenhouse gas and a major contributor to stratospheric ozone depletion. Fig. 2a shows the distribution of natural *versus* anthropogenic sources.

# 3. Categories of $N_2O$ decomposition catalysts based on their mechanisms and compositions

Catalysts for $N_2O$ decomposition are generally classified into different categories depending on their catalytic mechanism, composition, and support material. This classification helps us
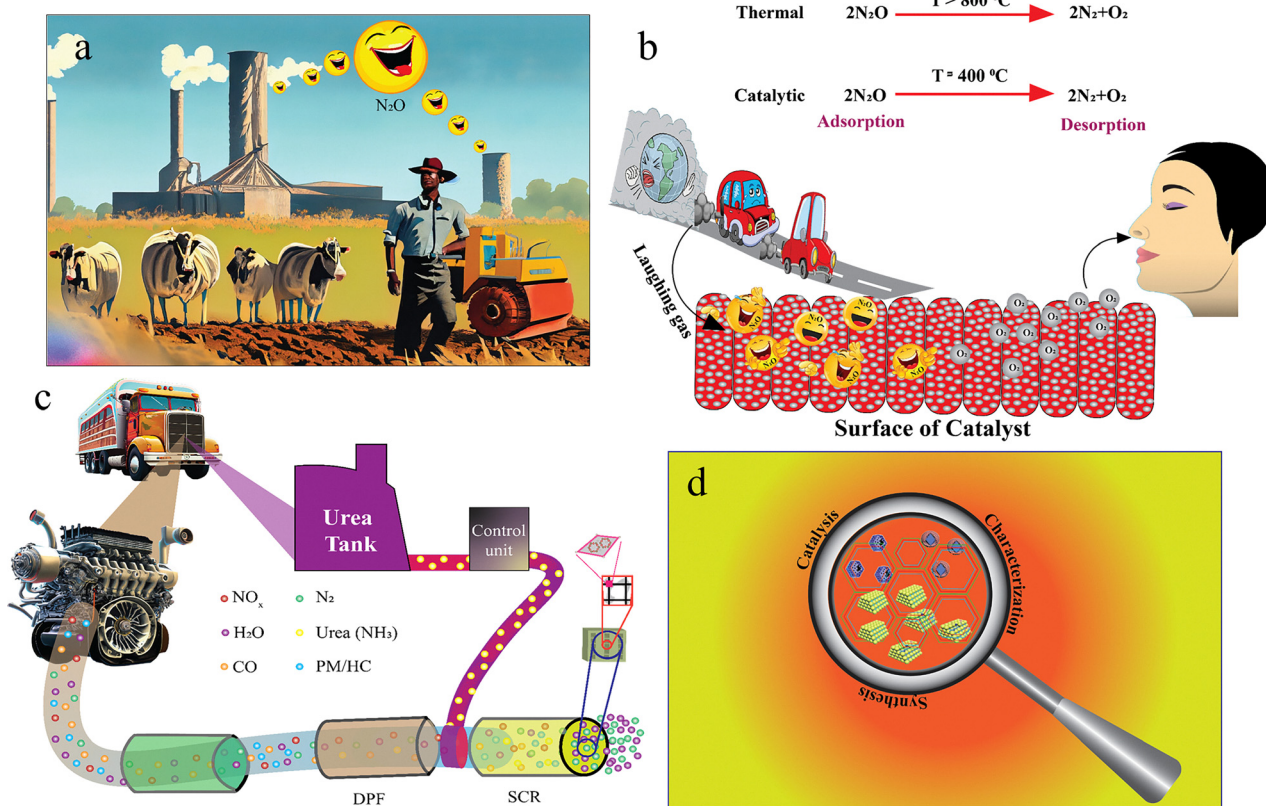


**Fig. 2** (a) Natural and anthropogenic sources of $N_2O$ (infamous laughing gas). (b) Thermal and catalytic paths of $N_2O$ decomposition. (c) Functioning of Cu-exchanged zeolites in the selective catalytic reduction of $NO_x$ from mobile sources.[11] Reproduced with permission from the American Chemical Society (Copyright©2013) (d). Advances in zeolite synthesis and characterization techniques for heterogeneous catalysis.

in understanding theory operational principles, activity under industrial conditions, cost-effectiveness and long-term stability. A detailed overview of each category is presented below.

### 3.1. Based on catalytic mechanisms

**3.1.1. Direct catalytic decomposition (DCD).** In this mechanism, catalysts decompose nitrous oxide ($N_2O$) directly into $N_2$ and $O_2$ without the need for a reducing agent:

$$2N_2O \rightarrow 2N_2 + O_2$$
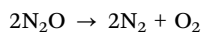
Examples of such catalysts include metal oxides [such as cobalt oxides ($Co_3O_4$), iron oxide ($Fe_2O_3$) and manganese oxide ($MnO_2$)], perovskites (e.g. $La_{1-x}Sr_xCoO_3$ with tunable oxygen vacancies that improve oxygen mobility and enhance $N_2O$ activation) and spinels (e.g. $CuFe_2O_4$, $MnAl_2O_4$) known for their stable structures and redox properties. In DCD, oxygen vacancies on these catalysts adsorb and activate $N_2O$, leading to bond cleavage and release of $N_2$. The oxygen atoms are either released as $O_2$ or incorporated temporarily into the lattice. These catalysts are widely considered for industrial emission control (e.g. nitric acid plants) where large volumes of $N_2O$ are generated.

**3.1.2. Selective catalytic reduction (SCR).** In SCR, a reducing agent (such as $NH_3$, CO or hydrocarbons like $CH_4$ and $C_3H_6$) is introduced to facilitate the reduction of $N_2O$ into $N_2$:

$$N_2O + 2CO \rightarrow N_2 + 2CO_2$$

$$N_2O + 2NH_3 \rightarrow 2N_2 + 3H_2O$$
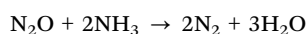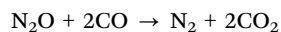
Examples of these catalysts include Fe- or Cu-exchanged zeolites (Fe–ZSM-5, Cu–SSZ-13, and Cu–ZSM-5) and vanadium-based catalysts ($V_2O_5/TiO_2$ and $V_2O_5$–$WO_3/TiO_2$). The reducing agent reacts with oxygen species from $N_2O$ decomposition, enhancing $N_2$ formation. SCR can operate at relatively low temperatures compared to DCD, making it practical for vehicular exhaust systems and stationary sources. SCR is often applied in mixed gas systems such as automotive exhausts, power plants, and mobile sources. Fig. 2c demonstrates the role of Cu-zeolites in ammonia-assisted SCR of $N_2O$, particularly effective in diesel engines.

### 3.2 Based on catalyst compositions

**3.2.1. Precious metal-based catalysts.** Precious metals such as Rh, Ru, Pt and Pd are highly active for $N_2O$ decomposition. They promote rapid N–O bond cleavage due to their strong adsorption capacity for $N_2O$. Examples include $Rh/Al_2O_3$, $Ru/CeO_2$, and $Pt/ZrO_2$. High catalytic activity and efficiency at relatively low temperatures are their key advantages. Their limitations are high cost (that makes them less suitable for large-scale industrial use) and susceptibility to deactivation due to sintering or poisoning (e.g. by sulphur or water vapours). They are often used in niche or specialized applications where high efficiency is required despite high costs (e.g. medical gas purification or research setups).

**3.2.2. Non-precious metal-based catalysts.** Non-precious metals (mainly transition metals and mixed oxides) are more cost-effective and environmentally sustainable, making them widely used in industrial processes. Examples include transition metal oxides (e.g. $Co_3O_4$, $MnO_x$, CuO, and $Fe_2O_3$), perovskites ($LaCoO_3$, $LaMnO_3$, and Sr-doped cobaltites with enhanced oxygen mobility), spinels ($CuFe_2O_4$ and $MnAl_2O_4$) and zeolites (Fe–ZSM-5 and Cu–SSZ-13 with high hydrothermal stability). Their advantages include low cost, abundant raw materials and high thermal stability. They generally require higher operating temperatures than that needed for precious metals, but can be optimized by doping or adding promoters. These are widely employed in industrial emission abatement systems, including nitric acid and adipic acid plants, as well as power generation facilities.

### 3.3 Based on support types

The support material plays a crucial role in dispersing active catalytic sites, enhancing redox behaviour, and providing structural stability under harsh reaction conditions. Common supports include metal oxides such as $Al_2O_3$, $TiO_2$ and $CeO_2$ due to their high surface area and redox properties. $CeO_2$, in particular, enhances oxygen storage and mobility, improving the catalytic efficiency. Zeolites include framework structures (such as ZSM-5, SSZ-13 and beta-zeolites) provide high surface area and microporosity. Their ion-exchange ability allows the incorporation of Fe or Cu cations, which significantly enhances SCR activity. SSZ-13 is particularly noted for high hydrothermal stability under automotive exhaust conditions. In carbon-based supports, activated carbon and graphene are sometimes used due to their large surface area and electrical conductivity. However, they are less common for $N_2O$ decomposition because of limited thermal stability at high operating temperatures. The choice of support directly influences catalyst dispersion, durability, oxygen mobility and tolerance to poisons (e.g. $SO_2$ and $H_2O$). Hence, support selection is as important as the active catalytic phase itself.

## 4. Significance of catalytic decomposition of $N_2O$

$N_2O$ is also a by-product in various industrial processes, including the catalytic abatement of nitrogen oxides ($NO_x$) in three-way catalytic converters and selective catalytic reduction (SCR) of $NO_x$ with $NH_3$. As $N_2O$ is a significant greenhouse gas and its emission contributes to the global warming and climate change, there is a pressing need to reduce $N_2O$ emissions from anthropogenic sources. One effective and economical method to reduce $N_2O$ emissions is the catalytic decomposition of $N_2O$ into its elemental components (nitrogen and oxygen), which is known as catalytic decomposition of $N_2O$.[12,13] To make it effective, the catalyst must be durable and selective. Durability ensures long-term effectiveness of the catalyst and selectivity ensures that $N_2O$ is effectively converted into nitrogen and oxygen without the formation of undesirable by-products.[14] Catalysts designed for $N_2O$ decomposition should be stable even in the presence of moisture, as they may encounter atmospheric moisture during real-world applications. $N_2O$ decomposition is an exothermic

reaction, meaning that it releases heat during the process. This can occur either thermally (without any catalyst) or catalytically (Fig. 2b). The choice between these paths depends on the factors such as operating temperature and the amount of catalysts used.[15] However, noble metal-based photocatalysts are among reliable options for $N_2O$ decomposition. These catalysts utilize noble metals (e.g. Pt and Pd) to facilitate the decomposition of $N_2O$ under the influence of light, making them a potential choice for efficient $N_2O$ abatement.[16]

A considerable amount of work has been done in the catalytic decomposition of $N_2O$, and a number of catalyst systems with various compositions such as zinc, platinum, copper oxides and zeolites have been developed.[17] Metal surfaces,[18] supported metals,[19] metal oxides,[20,21] supported oxides,[22] ternary oxides,[23] spinel oxides,[24] perovskite-type oxides,[25] hydrotalcites,[26] and transition metal exchanged zeolites[27] are well-known catalysts that can decompose $N_2O$ into its elements even at low temperatures. In this review, important categories of $N_2O$ decomposition catalysts are covered, which include transition metal-based zeolites, hydrotalcites, spinel oxides, mixed metal oxides, metal/ metal oxides in mesoporous silica, metal oxides, metal-doped nanotubes, nanosheets and nanocages, graphene and graphitic oxides/nitrides, metal–organic frameworks (MOFs), and MOF-derived catalysts. This review compares the different synthesis strategies of catalyst fabrication, experimental conditions, catalyst characterization techniques, $N_2O$ decomposition temperatures and catalytic efficiencies of various catalysts (Fig. 2d).

# 5. Progress-based systematic classification of $N_2O$ decomposition catalysts

$N_2O$ decomposition catalytic materials are classified into five main categories based on their structure, composition and research progress/maturity. Each category includes subtypes ordered by their level of maturity, from well-established (extensively studied) to emerging (recently developed or still under intense research).

## 5.1. Classical metal oxide-based catalysts

Classical metal oxide-based catalysts such as $Fe_2O_3$, $Co_3O_4$ and $MnO_2$ are most well-established and extensively studied for decades. They are renowned for their thermal stability, redox flexibility, and cost-effectiveness. These oxides typically possess high oxygen mobility and variable oxidation states, enabling efficient $N_2O$ decomposition via lattice oxygen participation. Their simple structures allow for easy synthesis, scalability, and tunability through doping or morphology control. Spinel-type oxides, in particular, exhibit strong metal–oxygen interactions and good resistance to sintering. Despite their maturity, continued research enhances their surface area, dispersion, and durability under reaction conditions. Their robustness and versatility make them fundamental benchmarks in both industrial and environmental catalytic applications. Four categories

of these catalysts are particularly important with respect to $N_2O$ decomposition.

**5.1.1. Metal oxide catalysts.** Transition metal oxides such as $NiO$, $Co_3O_4$, $MnO_2$, $CuO$, $Cr_2O_3$ and $Fe_2O_3$ exhibit high catalytic activity for the decomposition of $N_2O$. The transition metal oxides are known for their high thermal and chemical stability, making them suitable candidates for catalytic applications.[28–30] For example, Gaidei and co-workers synthesized a series of oxide catalysts containing up to 30% active metal components on an alumina carrier. The temperature dependence of $N_2O$ decomposition on these catalysts follow a well-defined S-shaped curve, similar to Pt family metals, but these transition metal oxide catalysts are somewhat less active than Pt-based catalysts. The catalytic activity of these metal oxide catalysts was ranked as follows in the increasing order of decomposition temperature: $Fe_2O_3$ < $Cr_2O_3$ < $CuO$ < $MnO_2$ < $NiO$ < $Co_3O_4$. Among the catalysts based on non-noble metals, $Co_3O_4$ showed the highest catalytic activity. The calculated activation energy values for these catalysts vary, with $CuO$ and $Cr_2O_3$ having the highest $E_a$ (187–176 kJ mol$^{-1}$) and $MnO_2$, $Co_3O_4$ and $NiO$ having lower values (133–143 kJ mol$^{-1}$). Based on experimental data, Co, Cu, Mn and Cr oxides are recommended as active components for developing deposited catalysts based on non-noble metals.[31] Fig. 3 signifies the use of acidic and high valence metal sites on the various metal oxide catalysts based on $MnO_x$, $CeO_2$, $Fe_2O_3$, $VO_x$ and $CuO$ for the $NH_3$-assited SCR of $NO_x$.[32]

CaO obtained from the domestic limestone has also demonstrated its catalytic effect in $N_2O$ decomposition. The effects of CO and $CO_2$ on $N_2O$ conversion activity were found antagonistic to each other. On the one hand, CO increases the $N_2O$ decomposition activity. On the other hand, higher $CO_2$ concentrations slowly decrease the $N_2O$ decomposition activity. As NO was also a hindering factor in $N_2O$ decomposition, in order to lessen its concentration, $N_2O$ was concurrently passed in the circulating fluidized bed combustion (CFBC) reactor. Selective non-catalytic reduction (SNCR) is a method of choice for the NO removal from flue gas.[33] Similarly, various Bi-based semiconductors were fabricated by a hydrothermal strategy,[34–36] e.g. Liu group examined monoclinic $BiVO_4$, orthorhombic $Bi_2MoO_6$ and $Bi_2WO_6$ catalysts for the photocatalytic degradation of $N_2O$ into $N_2$ and $O_2$, as shown in Fig. 4a. They found that $BiVO_4$ exhibited the highest degradation activity due to stronger absorption of visible light and higher charge separation.[37]

Metal-supported metal oxide catalysts are also popular for $N_2O$ decomposition reactions. Komvokis et al. synthesized a series of $Ru/Al_2O_3$ nanocatalysts via in situ reduction with ethylene glycol (EG) and compared their $N_2O$ reduction activity with the catalysts prepared through the typical incipient wetness procedure. The EG reduction approach resulted in the formation of spherical Ru nanoparticles (particle size: 1–3 nm; dispersion: 70–35%). While impregnated calcined catalysts had larger sized nanoparticles with a very small dispersion degree (particle size: 10–80 nm; dispersion: 10%). The catalysts synthesized via EG reduction showed significantly higher $N_2O$ decomposition activity in an $O_2$-rich environment irrespective of CO, $CO_2$, NO, $H_2O$ and $SO_2$. The higher surface area of Ru metal
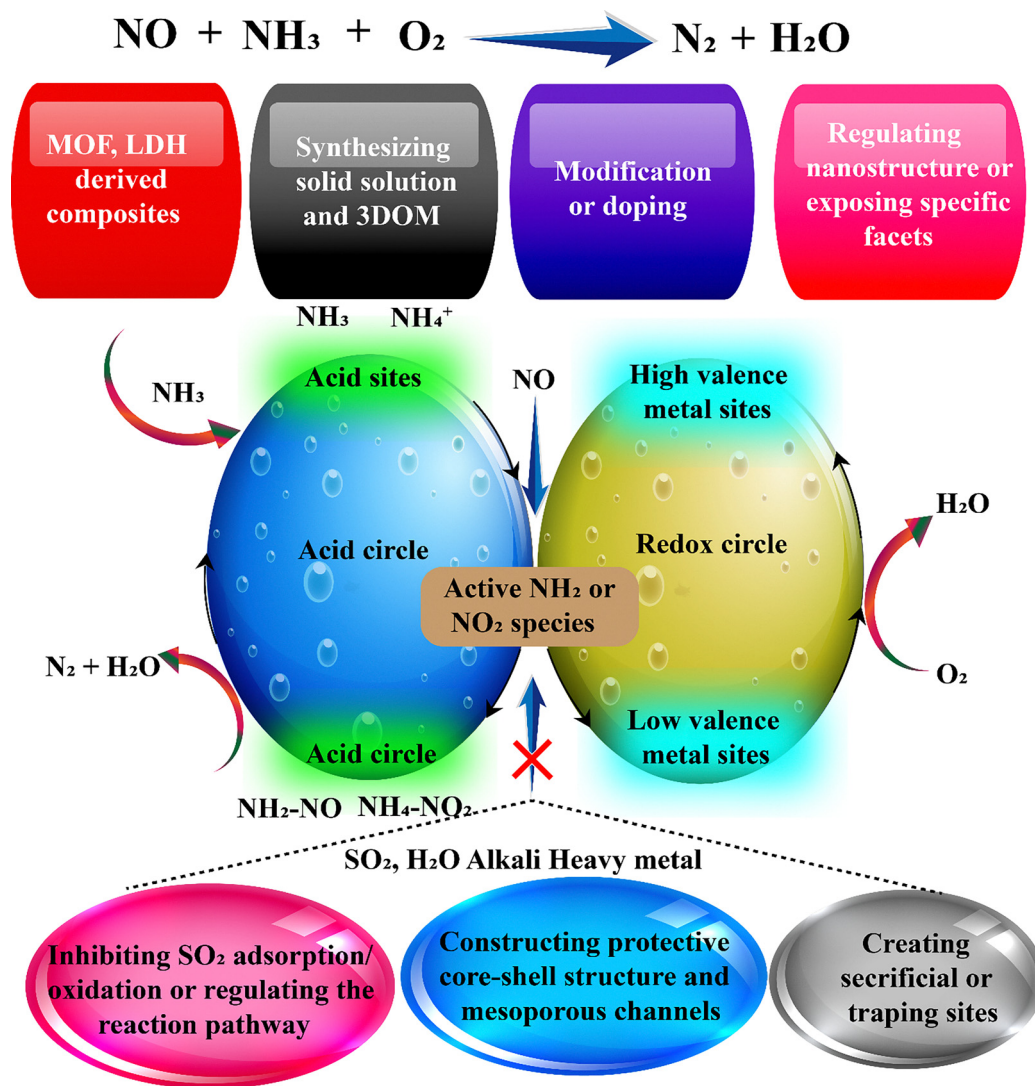
Fig. 3 Selective catalytic reduction of nitrogen oxides with $NH_3$ employing various acidic metal oxide composite catalysts.[32] Reproduced with permission from the American Chemical Society (Copyright©2019).

contributes to their higher catalytic activity. These catalysts have a low apparent activation energy, which suggests that they require less energy to initiate the chemical reaction. $Ru/Al_2O_3$ nanocatalysts can be regenerated effectively that helps to restore their catalytic activity, achieving a conversion rate of over 90%.[39] Similarly, Reddya et al. synthesized alumina-supported Pd catalysts ($Pd/Al_2O_3$) employing the deposition precipitation (DP) and impregnation (IMP) methods and studied their effect on $N_2O$ conversion activity. Higher catalytic efficiency was recorded for DP catalysts as compared to their IMP equivalents due to the formation of partially oxidized $Pd^{2+}$ species over the surface of the DP–Cl catalyst.[40]

In a general $N_2O$ decomposition reaction, CO is adsorbed over the surface of catalysts to reduce $N_2O$, but this strong adsorption of CO may lead to the catalyst's poisoning. For example, Zhang et al. have utilized the Mans-van-Krevelen mechanism by employing phosphotungstic acid (PTA)-supported single-atom catalysts (SACs), M/PTA, where M = Fe, Co, Mn, Rh, Ru, Ir,

Os, Pt and Pd. Adsorbed CO reacts with the surface oxygen atoms of PTA support and create holes on the M/PTA surface. $N_2O$ acts as an oxygen donor to regenerate catalyst and releases $N_2$. It was also demonstrated that among all metals, Pd/PTA, Rh/PTA and Pt/PTA are most efficient catalysts. Fig. 4b shows the mechanism for the reduction of $N_2O$ by CO over M/PTA catalysts.[38] Metals such as Co, Cu or Fe supported on $ZrO_2$ are also active in the decomposition of $N_2O$. The activity pattern is Co > Cu ≫ Fe. $ZrO_2$ catalysts have the advantage of hydrothermal stability. Unlike that of zeolite systems, their catalytic activity is recovered when $H_2O$ vapours are eliminated from the feed gas.[41]

Tuti et al. further investigated $N_2O$ adsorption and decomposition on $ZrO_2$. At 25 °C, $N_2O$ molecularly adsorbs through the $O_2$ end on $Zr^{4+}$ sites and dissociative adsorption of $N_2O$ occurs on surface defect sites, i.e. $Zr^{3+}$ sites. It was noted that N–N bond dissociation did not occur and oxygen atoms of the lattice become incorporated into the product $O_2$ molecules.[42]
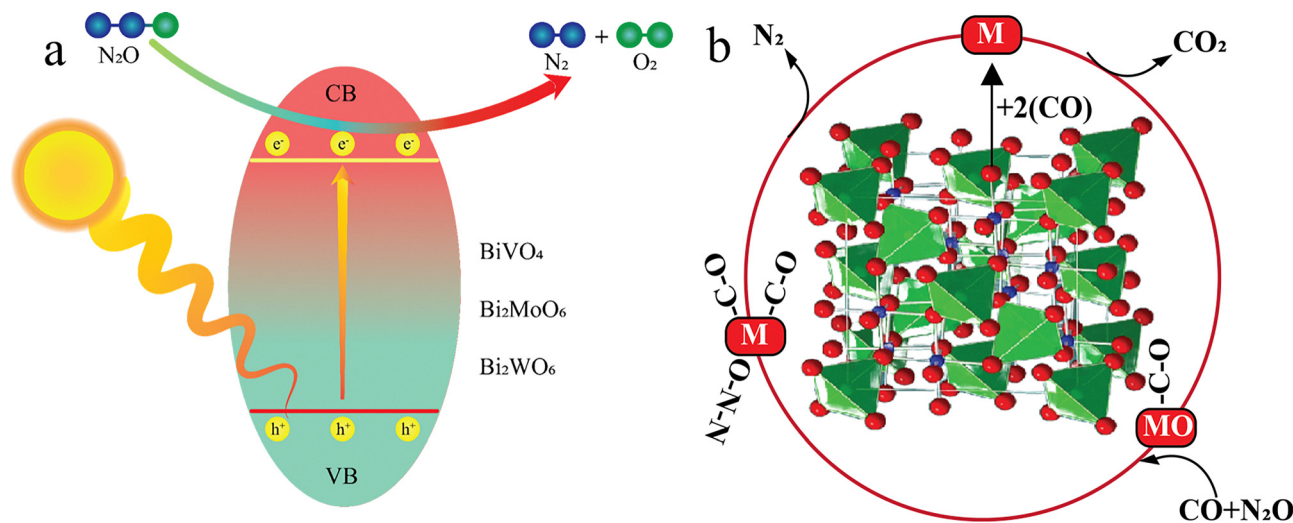
**Fig. 4** (a) Photocatalytic $N_2O$ decomposition *via* Bi-based photocatalysts (*i.e.* $BiVO_4$, $Bi_2MoO_6$ and $Bi_2WO_6$) under visible light irradiation.[37] Reproduced with permission from the American Chemical Society (Copyright©2018). (b) Mans–van Krevelen mechanism over phosphotungstic acid supported SACs for the reduction of $N_2O$ by CO.[38] Reproduced with permission from the American Chemical Society (Copyright©2019).

In a different study, researchers have used a cluster model represented by $M(OH)_3(H_2O)_2$, where M represents different transition metals such as Co, Fe and Rh. The results indicated that Rh and Co sites were more active for the $N_2O$ decomposition reaction as compared to Fe. The rate-limiting step is the formation of adsorbed $O_2$ molecules *via* the interaction of adsorbed oxygen atoms with $N_2O$. A correlation was observed between the activation energy ($E_a$) and the strength of the M–O bond. Weaker metal-adsorbed oxygen bonds for Co and Rh sites facilitated the decomposition of the second $N_2O$ molecule into $O_2$, lowering the activation barrier.[43] In the case of $Fe(OH)_3(H_2O)_2$, the transition state analysis suggested that $N_2O$ dissociation was achieved through electron density donation from the metal to an $N_2O$ molecule.[44] Various other examples of $N_2O$ decomposition metal oxide catalysts are provided in Table 1.

*5.1.1.1. Shortcomings of metal oxide catalysts.* Though pure metal oxides show the highest catalytic efficiencies in the cases of transition metal oxides of group VIII and some rare earth oxides (*e.g.* La), it is also worthwhile to note that, based upon

experimental conditions, metal oxides including $MnO_2$, MnO, $Cu_2O$ and CoO are not stable and are partially decomposed.[54] As a result, $N_2O$ decomposition studies took a turn towards the development of more active and stable catalytic systems. Another important fact about pure metal oxide catalysts is the utilization of high temperature for catalyzing $N_2O$ decomposition because of the limited availability of active sites at low temperatures due to adsorbed oxygen recombination. In addition, the presence of $H_2O$ exerts a negative effect on catalytic efficiency due to its competitive adsorption on active sites.[21]

*5.1.1.2. Application scenario: nitric acid plants.* Metal oxide catalysts such as $Co_3O_4$, $Fe_2O_3$ and $MnO_2$ are low-cost, stable, and effective for $N_2O$ decomposition under high-temperature conditions typical of nitric acid plants. They offer thermal robustness and environmental compatibility but require elevated activation temperatures, show reduced efficiency at intermediate ranges and are vulnerable to deactivation by $H_2O$ and $SO_2$ impurities.

**5.1.2. Spinel oxides.** Spinel oxides, having the structural formula of $AB_2O_4$, show high thermal stability and redox

**Table 1** Overview of synthesis methods, reaction conditions and various techniques employed during the course of analysis of metal oxide-based catalysts for $N_2O$ decomposition

| Catalysts | Method of preparation | Reaction atmosphere | Air speed (mL min$^{-1}$) | $N_2O$ decomposition temp-range (°C K$^{-1}$) | Techniques used for the characterization and assessing the activity of catalysts | Ref. |
|---|---|---|---|---|---|---|
| CaO catalysts | Hydrothermal | — | — | 1073–1273 K | DFT method, on-line gas flue analyzer, GC | 45 |
| $\gamma$-$Fe_2O_3$ | Co-precipitation | $N_2$ | 50 | 100–400 °C | XRD, XPS, FTIR | 46 |
| Al-doped $MoS_2$ | — | Ethylene oxide | — | — | DFT | 47 |
| 3.0F–$Co_3O_4$ | Sol–gel | Ar | 50 | 250–450 °C | TEM, HRTEM | 48 |
| $Ti_3O_6$@$TiO_2$ | — | — | — | — | DFT | 49 |
| Ni > Co > Fe > Cu | Impregnation | $N_2$ | 400 | 200–500 °C | DFT | 50 |
| $Co_3O_4$ | Sol–gel | — | — | — | UV-visible spectra, $H_2$-TPR, XPS, TEM, EXAFS, EDS, NAP-XPS | 51 |
| $Sm_{0.1}$–$Co_3O_4$ | Sol–gel | Ar | 50 | 300–500 °C | XRD, XPS, STEM, EELS, $H_2$-TPR | 52 |
| N-doped $Co_3O_4$ | Sol–gel | $H_2$/$N_2$ | 30 | 150–500 °C | FTIR, XRD, TEM, EDX, XPS, $O_2$-TPD | 53 |

activity. In several redox reactions such as the reduction of $N_2O$ and oxidation of higher hydrocarbons and CO, cobalt spinel catalysts have been widely investigated.[55] It has been demonstrated that $Co_3O_4$ is more active in CO oxidation than $Fe_2O_3$, $Cu_2O$, NiO, MnO, $V_2O_5$, $Cr_2O$, $CeO_2$ and ZnO. Because of its capability to bind quickly with oxygen and a very low M–O bond energy, cobalt spinel is believed to display the highest activity in hydrocarbon oxidation.[56] Fig. 5 represents the synthesis and use of various metal spinels in different electronic materials (ORR and OER).[57]

Shen *et al.* investigated the catalytic conversion of $N_2O$ using cobalt oxide catalysts supported on various materials and synthesized using a co-precipitation method. Among the supports tested, alkaline MgO was found to be the most effective due to its strong electron-donating properties. Here cobalt existed in the form of $Co_3O_4$ nanoparticles dispersed in the MgO matrix. Under specific conditions, the Co–MgO-15% catalyst demonstrated good activity on decomposing $N_2O$, making it a potential candidate for mitigating greenhouse gas emissions from anthropogenic sources.[58] The advantages of using Co oxide-based spinel catalysts lie in their capability to decompose $N_2O$ below 400 °C and sufficient catalytic activity. Another benefit of using spinel oxide catalysts containing Rh is that they exhibit unusual catalytic activities in the absence of water but these catalysts rapidly lose their activity upon exposure to water.[59,60]

Researchers have tried to find whether the catalytic activity of cobalt spinel oxide catalysts is influenced by the addition of gases such as $NO_2$, NO, $O_2$ and $H_2O$ vapours or not. It has been found that operating the reaction at 850 °C led to a higher $N_2O$ conversion rate than operating the reaction at 800 °C.

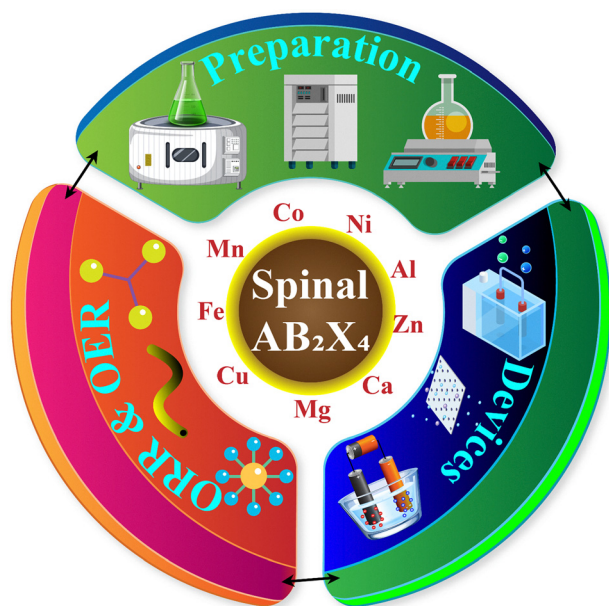This improvement was attributed to the presence of $O_2$, which altered the oxidation state of Co in the catalyst.[25]

However, at lower temperatures, the presence of $O_2$ reduced $N_2O$ conversion. $H_2O$ vapours also have a detrimental effect on the catalyst's activity at all temperatures. This was likely due to the competitive chemisorption of $H_2O$ vapours on the active sites, hindering $N_2O$ decomposition. Unlike $O_2$ and $H_2O$ vapours, however $NO_2$ did not decompose over the cobalt catalyst and it did not impact the catalyst's state. It had no effect on $N_2O$ conversion. However, the presence of NO in the feed gas mixture at 850 °C led to higher $N_2O$ reduction values. This was attributed to NO's influence on the process, possibly affecting the last phase of $N_2O$ decomposition. The state of catalyst was also influenced by temperature variations, particularly when exposed to a feed gas mixture containing $O_2$, $N_2O$ and Ar at temperatures ranging from 700 °C to 850 °C.[61] Extensive examples of the $N_2O$ decomposition by spinel oxide catalysts are enlisted in Table 2.

*5.1.2.1. Shortcomings of spinel oxide catalysts.* Spinel oxide catalysts often suffer from limited surface area and poor dispersion of active sites, reducing their catalytic efficiency. Their high-temperature synthesis can lead to particle sintering, decreasing reactivity. Additionally, some spinels exhibit slow oxygen mobility and reduced activity at low temperatures, limiting their applicability under mild reaction conditions. Stability under hydrothermal conditions can also be a concern.

*5.1.2.2. Application scenario: industrial flue gas treatment.* Spinel oxides are attractive for $N_2O$ decomposition in industrial flue gas streams due to their structural stability, redox flexibility and cost-effectiveness. They operate efficiently at high temperatures and tolerate thermal stress, but limitations include moderate activity at lower temperatures and susceptibility to poisoning by $SO_2$ and $H_2O$ commonly present in flue gases.

**5.1.3. Hydroxyapatites.** Hydroxyapatites, having the formula $Ca_{10}(PO_4)_6(OH)_2$, act as dual catalysts in acid-base and redox catalysis. They enable moderate activity for $N_2O$ decomposition. Their flexible structure allows ion substitution (*e.g.* with transition metals), enhancing catalytic sites. They exhibit good thermal stability and surface hydroxylation but generally require modification for high activity. Their tenability makes them suitable for multifunctional or hybrid catalytic systems under mild conditions.[81]

In the 1990s, hydroxyapatite catalysts (containing calcium and phosphate ions) were employed for indirect $N_2O$ decomposition *via* partial oxidation of methane.[82,83] However, during the last few years, hydroxyapatites have been used as supports for Rh and Ru catalysts in $N_2O$ abatement.[84,85] Galloni *et al.* evaluated Cu- and Fe-loaded hydroxyapatite catalysts for $N_2O$ decomposition, revealing superior Cu performance due to nanoparticle formation, with detailed structural, stability and resistance analyses supporting catalytic behaviour.[86] Wei *et al.* obtained natural hydroxyapatite from bone, and after doping it with Co ions, Co/nHAP catalysts were prepared and utilized for the investigation of $N_2O$ decomposition reaction.[62] Fig. 6a shows the mechanistic pathway of $N_2O$ reduction over a Co/nHAP catalyst, while Fig. 6b indicates $N_2O$ conversion profiles with respect to the increasing temperature. Similarly, Tan *et al.* synthesized hydroxyapatite-supported bimetallic (Fe, Rh) catalysts for plasma-



**Fig. 5** Synthesis routes and applications of spinel oxides $(AB_2X_4)$.[56] Reproduced with permission from the American Chemical Society (Copyright©2017).

**Table 2** Overview of synthesis methods, reaction conditions and various techniques employed during the course of analysis of different spinel oxide catalysts for $N_2O$ decomposition

| Catalysts | Methods | Reaction atmosphere | Air speed (mL min$^{-1}$) | $N_2O$ decomposition temp-range (°C K$^{-1}$) | Techniques used for characterization and activity of catalysts | Ref. |
|---|---|---|---|---|---|---|
| Co/nHAP | Hydrothermal | Ar | — | 200–600 °C | XRD, TEM, HADDF–STEM, XPS | 62 |
| ($Co_3O_4$) (CS–N) | Co-precipitation | — | — | 100–400 °C | XRD | 63 |
| $Co_3O_4$ | Hydrothermal | He | 30 | 100–600 °C | $O_2$-TPD, DFT calculations, XRD, FTIR, SEM, XRF, TPSR | 55 |
| $Co_3O_4$-based catalyst | Co-precipitation | $N_2$ | 50 | 400–600 °C | XRF, XRD, $H_2$-TPR, TEM, EDX, SAED | 64 |
| Cs-doped Co-spinel catalysts (Cs–$Co_3O_4$) | Wetness impregnation | — | — | <200 °C | XRF, XRD, SEM, XPS, Raman, TPCR, QMS | 65 |
| de$NO_x$ and de$N_2O$ | Precipitation | — | — | 425–450 °C | FTIR | 66 |
| $Cu_xCo_{1-x}Co_2O_4$ spinel-oxide catalysts | Co-precipitation | $N_2$ | 200 | 150–500 °C | TGA, DTA, FTIR, XRD | 67 |
| $Co_3O_4$ | PVA-assisted precipitation | $N_2$ | 65 | 300–600 °C | DFT, XRD, XPS, TEM, SEM, FTIR, EPR | 68 |
| $Co_3O_4$ | PVA-assisted precipitation | — | — | 150–450 °C | XRD | 69 |
| K-doped $Cu_xCo_{3-x}O_4$ catalysts | Thermal decomposition | $O_2$ | 20 | 250–650 °C | XRD, TGA, TPR, $N_2$-physisorption, $O_2$-TPD, ICP-OES, BET | 70 |
| Co–Mn–Al mixed oxide catalysts | Precipitation | $H_2$ | 50 | 40–450 °C | AAS, XRD, SEM, Raman, FTIR, TPR-$H_2$, TPD-$N_2O$, SEM, EDS, MS | 71 |
| Co-based spinel oxides | Impregnation | — | 50 | 25–400 °C | XRD, BET, $H_2$-TPR, $O_2$-TPD, XPS | 59 |
| $Ag_xCo$ (x = 0–0.08) oxide catalysts | Co-precipitation | Ar | 30 | 200–400 °C | XRD, TEM, $O_2$-TPD, BET, $H_2$-TPR, GC-TCD, XPS | 72 |
| Bi–$Co_3O_4$ catalysts | Co-precipitation | Ar | 50 | 200–500 °C | $O_2$-TPD, BET, XRD, GC | 73 |
| Alien cations doped-nanocrystalline Co-spinel catalysts | Co-precipitation | He | 30 | 100–600 °C | XRD, Raman, BET, XPS, $H_2$-TPR, TEM | 74 |
| LT-de$N_2O$ catalysts (K/$Zn_{0.4}Co_{2.6}O_4$/$\alpha Al_2O_3$) | Co-precipitation | — | — | 405–445 °C | FTIR using on-line analyzer | 75 |
| $Zn_xCo_{1-x}Co_2O_4$ spinel catalyst | Co-precipitation | $O_2$ | 10 | — | XRD, EDX | 76 |
| $Co_3O_4$–Cs | Wet impregnation | $H_2$ | 50 | 100–400 °C | XPS, SEM, $H_2$-TPR, XRD | 77 |
| Cd–$Co_3O_4$ spinel catalysts | Co-precipitation | — | — | — | TGA, DTA, XRD, FTIR, $N_2$-physisorption, AAS | 78 |
| N-doped $Co_3O_4$ | Sol–gel method | $H_2/N_2$ | 30 | 200–500 °C | XRD, FTIR, Raman, $N_2$-physisorption, TEM, EDX, HADDF–STEM, $H_2$-TPR, $O_2$-TPD, EPR, $CO_2$-TPD | 53 |
| $(CuMgNiZn)_1Co_2O_4$ catalysts | Co-precipitation | $H_2$ | 50 | 150–500 °C | DFT, TPSR | 79 |
| Mn–Fe spinel catalysts | Co-precipitation | $H_2$ | 100 | 100–400 °C | $NH_3$-TPD, NO-TPD, DRIFTS, FTIR, DFT | 80 |

assisted $N_2O$ decomposition studies. In this instance, reaction temperature was lowered to a higher degree as free radicals generated by plasma initiated the catalytic decomposition reaction faster even at low temperatures.[87] Fig. 6c and d indicate the mechanism and conversion profiles of $N_2O$. More examples are represented in Table 3.

*5.1.3.1. Shortcomings of hydroxyapatite catalysts.* These catalysts face several limitations including relatively low intrinsic activity compared to conventional metal oxides. Their performance heavily depends on metal ion doping, as pure HAP is largely inactive. Additionally, achieving uniform dispersion of active sites can be a challenge. They may also show reduced thermal stability under harsh conditions, and are susceptible to deactivation by sulphur or alkali contaminants without proper modification.

*5.1.3.2. Application scenario: wastewater treatment facilities.* These catalysts offer tunable surface properties, ion-exchange capacity and good thermal stability, making them promising for $N_2O$ decomposition in wastewater treatment off-gases. Their biocompatibility and low costs are additional advantages. However, they often show limited intrinsic activity, require modification with transition metals to enhance performance, and may suffer from deactivation under humid, impurity-rich gas conditions.

**5.1.4. Mixed metal oxide catalysts.** A lot of work has already been conducted on mixed metal oxide systems, *e.g.* metal-doped oxides and transition metal ions in inert matrices. Due to the unusual structure, thermal stability, synthesis at high temperature and low SSAs, the mixed metal oxides are famous for their $N_2O$ decomposition activity.[93] Transition metal ions are very specific in their activity based on their oxidation state, *e.g.* MgO matrix-dispersed Mn(III) ions showed the highest catalytic efficiency as compared to Mn(II) and Mn(IV).[94] However, the supported oxides possess better practical applications than pure and mixed metal oxides because of higher dispersion of metal ions in the large surface areas of different well-known supports including alumina, mesoporous silica, zirconia, ceria and titania. The catalytic efficiency is determined by metal loading, method of synthesis, and temperature.
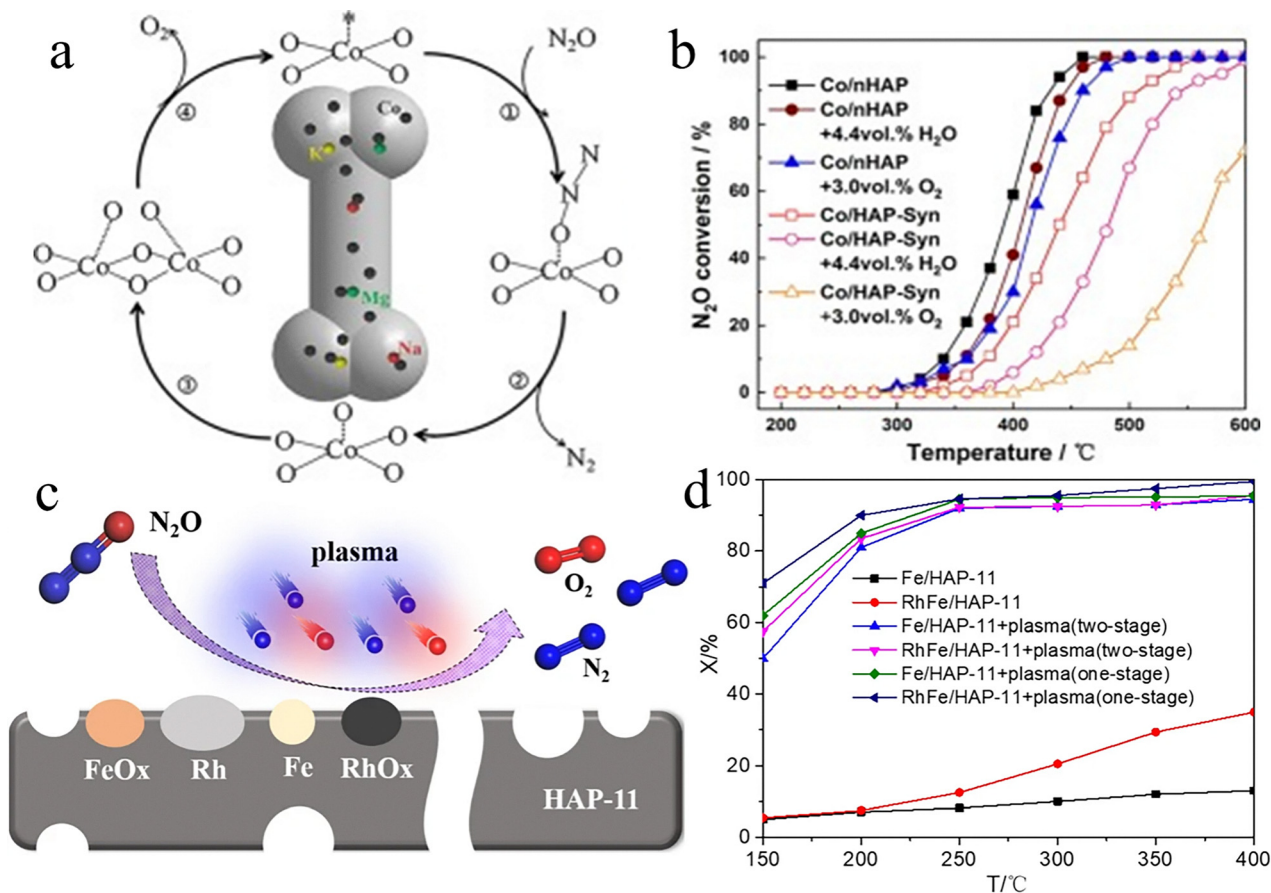
**Fig. 6** (a) Break down of $N_2O$ over the surface of Co-doped bone-derived hydroxyapatite (Co/nHAP) catalysts. (b) $N_2O$ decomposition profile.[62] Reproduced with permission from Elsevier (Copyright©2020). (c) Mechanism of plasma-assisted $N_2O$ degradation over the surface of bimetallic RhFe/HAP catalysts. (d) Variation in % $N_2O$ decomposition w.r.t. temperature on RhFe/HAP and Fe/HAP catalysts.[87] Reproduced with permission from Springer-Nature (Copyright©2023).

**Table 3** Overview of synthesis methods, reaction conditions and various techniques employed during the course of analysis of hydroxyapatite-based catalysts for $N_2O$ decomposition

| Catalysts | Method | Reaction atmosphere | Air speed (mL min$^{-1}$) | $N_2O$ decomposition temp-range (°C K$^{-1}$) | Techniques used for characterization and activity of catalysts | Ref. |
|---|---|---|---|---|---|---|
| Hydroxyapatite-supported RhO$_x$ catalysts (RhO$_x$-HAP) | Wet impregnation | O$_2$ | 30 | 150–400 °C | XRD, TEM, ICP, XPS, BET, CO$_2$-TPD, O$_2$-TPD, GC, FT-IR | 88 |
| RuO$_x$/M–P–O catalysts | Impregnating | H$_2$/He | 10 | 150–400 °C | ICP–OES, XRD, BET, TEM, XPS, CO$_2$-TPD, O$_2$-TPD, H$_2$-TPR, GC-TCD, QMS | 84 |
| Co/Hydroxyapatite | Hydrothermal | — | — | 100–900 °C | XRD, TEM, HRTEM, EDX, STEM, UV-vis | 89 |
| Hydroxyapatite supported Rh, Fe, and Rh–Fe catalysts | Impregnation | He | 60 | 150–200 °C | XRD, SEM, TEM, TG, XPS, CO$_2$-TPD | 87 |
| Hydroxyapatite (HAP, Ca$_{10}$(PO$_4$)$_6$(OH)$_2$) | Hydrothermal | NO | 15 | 400–450 °C | N$_2$-physisorption, XRPD, NH$_3$-titration, UV-DRS, Mössbauer, XPS, and EXAFS | 90 |
| Calcium hydroxyapatite (HAP, Ca$_{10}$(PO$_4$)$_6$(OH)$_2$) | Co-precipitation | — | — | 120–800 °C | UV-DRS and Mössbauer spectroscopies, NH$_3$ titration, N$_2$-physisorption and XRPD | 91 |
| Apatite-supported Co$_3$O$_4$ | Co-precipitation | H$_2$/N$_2$ | 30 | 300–600 °C | XRD, XPS, H$_2$-TPR, TEM, Raman, FT-IR | 92 |

For the purpose of efficient $N_2O$ abatement, mixed metal oxide catalysts have been proved to be very effective catalysts.[95–98] Beyer *et al.* studied the $N_2O$ decomposition over different Rh-supported metal and non-metal oxides, *e.g.* Rh/SiO$_2$, Rh/MgO, Rh/Al$_2$O$_3$, Rh/TiO$_2$ and Rh/CeO$_2$, in both the presence and the absence of O$_2$. Rh/SiO$_2$ and Rh/MgO showed high catalytic activity for $N_2O$

conversion, even at low temperatures in the presence of O$_2$. In Rh/Al$_2$O$_3$, Rh/TiO$_2$ and Rh/CeO$_2$, smaller sized Rh nanoparticles were abundant, resulting in lower catalytic activities. The particle size of Rh was a crucial factor affecting the overall catalytic performance.[99] The redox properties of active Rh components were affected by the acid-base properties of the support. The reduction

abilities of Rh species decreased as the basicity of the support increased, indicating a strong interaction of Rh species with $O_2$. Han *et al.* employed mesoporous $TiO_2@Fe_2O_3@Al_2O_3$ core-shell nanostructures for low-temperature selective catalytic reduction (SCR) of $NO_x$. It effectively prevented the deposition of sulphur compounds and accelerated the SCR of $NO_x$ by facilitating electron transfer at the $Fe_2O_3$–$TiO_2$ interface. Fig. 7a depicts the comparison of mechanisms for the standard SCR with the fast SCR that these catalysts follow.[100]

Similarly, Gaidei *et al.* also synthesized and compared $N_2O$ decomposition activities of various Rh-supported metal oxide catalysts, *i.e.* $Rh/ZrO_2$, $Rh/Al_2O_3$ and $Rh/Al_2O_3$–$SiO_2$. The catalysts were exposed to an intimal temperature of 450 °C in a reactor. As a result, they exhibited excellent dynamic characteristics to initiate and sustain the reaction. The catalyst's activity decreased over time. Unloaded catalysts achieved 100% decomposition of $N_2O$ within the temperature range of 460–480 °C that indicated its effectiveness in promoting decomposition reaction. X-ray analysis revealed the presence of phase transitions in carrier materials and oxidation of Rh during the operational time.[102] In yet another study, Ratanatawanate *et al.* have devised a method that combined PbS QD-decorated $TiO_2$ nanotubes with S-nitrosocysteine that released $NO_2$ that further produced singlet oxygen.[101] The whole setup for the attachment of PbS QDs with the surface of $TiO_2$ nanotubes and release of $NO_2$ is shown in Fig. 7b.

Imamura *et al.* investigated the impact of adding praseodymium (Pr) to $CeO_2$ to investigate the catalytic decomposition of $N_2O$. They prepared a catalyst by incorporating Rh on $Pr/CeO_2$ composites. These catalysts were then subjected to calcination at different temperatures. However, the presence of Pr alone did not significantly affect the catalytic activity. A significant acceleration in the $N_2O$ decomposition rate was observed, as the calcination temperature of the catalysts was increased. Notably, the catalytic performance of the Rh-supported composite oxides ($Pr$–$Rh/CeO_2$) calcined at 800 °C was found to be most effective.[103] One of the chief advantages of Rh-doped ceria catalysts is that they retain an exceptionally high catalytic efficiency even in the presence of oxygen and water. Because of the hydrophobic nature of $Rh/CeO_2$ catalysts, they are much less sensitive to moisture than the other catalysts.[104] In another investigation, Peck *et al.* fabricated a series of $CeO_2$-supported $Fe_2O_3$ and $Co_2O_3$ catalysts along with the increase in the metal loadings to determine monolayer surface coverage on the $CeO_2$ support. It results in higher catalytic activities through the maximization of supporting metal–oxygen bonds. $NO_x$ was reduced by CO in the presence of sufficient amounts of $O_2$.[105] Fig. 8 represents the overall layout of $NO_x$ reduction by CO.

$N_2O$ decomposition was also tested on mixed metal oxides containing noble metals (*i.e.* Pt and Pd) supported on various oxide materials. The type of support material has a significant impact on the initial decomposition of $N_2O$. Important support materials include $SiO_2$ and $Al_2O_3$. At low temperatures (298 K), the $Pt/SiO_2$–$Al_2O_3$ catalysts showed low activity compared to the other catalytic systems. However, their activity boosted at higher temperatures (573 K). This suggested that the support material's influence on $N_2O$ decomposition depends on the

reaction temperature.[106] Another important aspect of the support effect is change in the $N_2O$ conversion with pulse numbers. In most cases, $N_2O$ decomposition exhibited a steep decrease with the increase in pulse number. However, $Pt/SiO_2$–$Al_2O_3$ catalysts showed exceptionally high $N_2O$ conversion rates at the second and third pulses.[107]

Rh-, Ru-, and Ir-based mixed metal oxides exhibited the highest activity in decomposing $N_2O$. However these catalysts are susceptible to oxidation at high temperatures due to their oxidation potentials. Ru- and Ir-based metal oxide catalysts tend to form highly volatile oxides at elevated temperatures, leading to the loss of active metal components and a decrease in catalytic activity. Given its stability in the context of $N_2O$ decomposition, Rh is recommended as the preferred active component for catalysts used in this reaction.[108] Table 4 presents various examples of mixed metal oxide catalysts utilized for $N_2O$ abatement studies.

*5.1.4.1. Shortcomings of mixed metal oxide catalysts.* Mixed metal oxide catalysts, despite their tunable composition and synergistic effects, often suffer from limited control over active site uniformity and metal dispersion. Their synthesis can lead to phase separation or undesired crystallinity, reducing the catalytic efficiency. Additionally, some systems exhibit poor low-temperature activity and deactivation under long-term operation, especially in the presence of moisture or contaminants. Scalability and reproducibility also remain a challenge for complex multi-metal formulations.

*5.1.4.2. Application scenario: nitric acid plant emissions.* Mixed metal oxides are highly effective for $N_2O$ abatement in nitric acid plant emissions due to their synergistic redox properties, abundant oxygen vacancies and strong thermal stability. They are cost-efficient and tunable, but challenges include maintaining long-term stability under fluctuating gas conditions and vulnerability to poisoning by $SO_2$ and water vapour.

### 5.2. Layered and framework structures

Layered and framework structure-based catalysts such as zeolites, hydrotalcites and mesoporous silica-supported systems offer unique structural advantages for $N_2O$ decomposition. Their well-defined pores and channels facilitate controlled diffusion and confinement of reactants, enhancing the selectivity and activity. Transition metal ions incorporated into frameworks (*e.g.* Fe–ZSM-5) act as isolated redox centres, promoting effective N–O bond cleavage.

Hydrotalcites provide tunable acid-base sites and high dispersion of metal species upon calcination. These materials also support ion-exchange capabilities, allowing precise modifications of active sites. However, their catalytic performance can depend heavily on pore architecture, metal loading and thermal stability under reaction conditions. Three classes of this category are given in this section.

**5.2.1. Hydrotalcites (layered double hydroxides).** With the structural formula of $[M_{1-x}^{2+}M_x^{3+}(OH)_2]^{x+}(A^{n-})^{x-}\cdot yH_2O$, hydrotalcites (HTs) possess excellent anion exchange capacity and
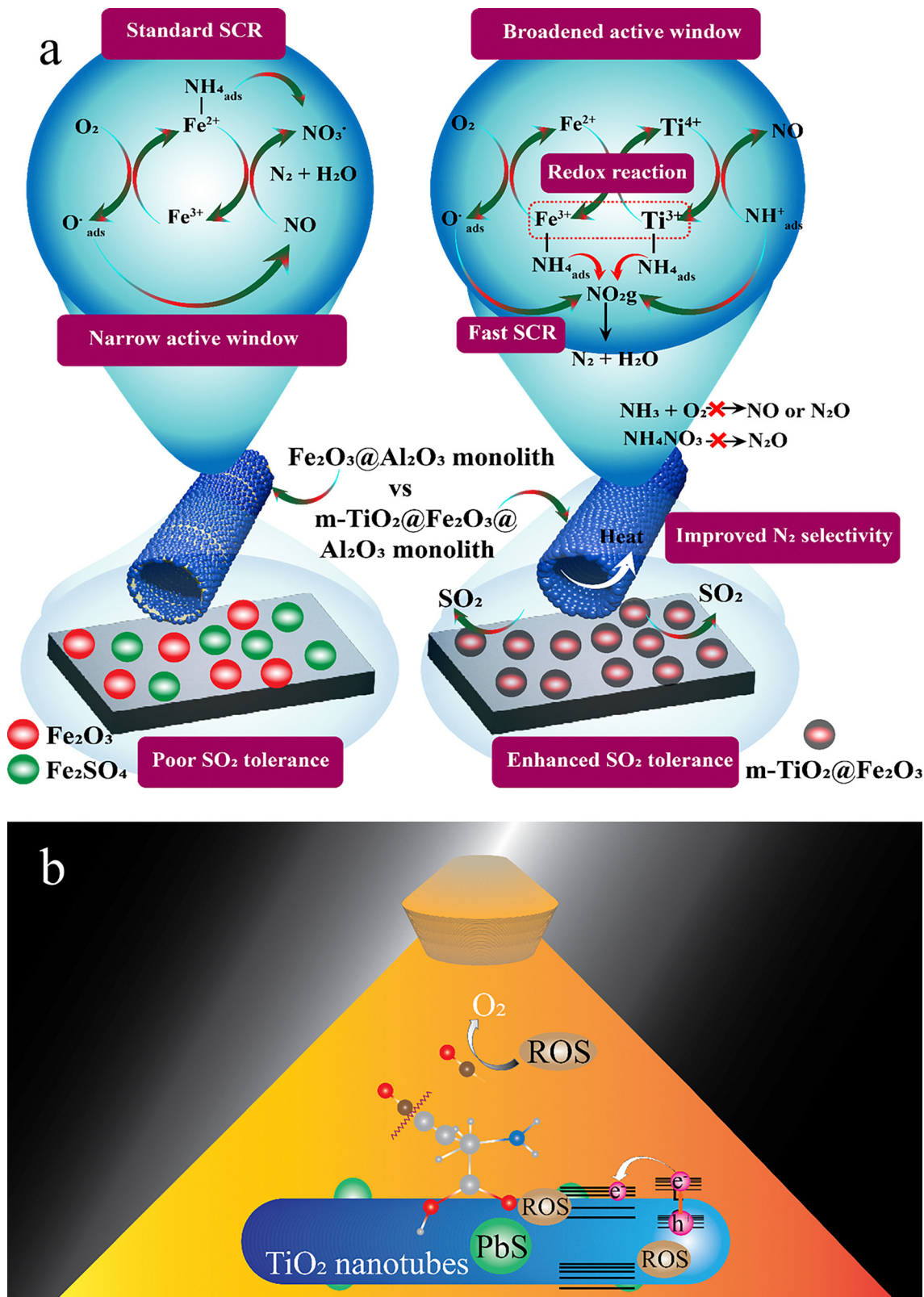
**Fig. 7**  (a) Mechanism of $SO_2$-tolerant selective catalytic reduction of $NO_x$ with $NH_3$ employing mesoporous $TiO_2$@$Fe_2O_3$@$Al_2O_3$ monolith composites at low temperatures.[80] Reproduced with permission from the American Chemical Society (Copyright©2019). (b) Mechanism of $NO_2$ release *via* the combination of *S*-nitrocysteine with PbS quantum dots decorated $TiO_2$ nanotubes.[101] Reproduced with permission from American Chemical Society (Copyright©2011).
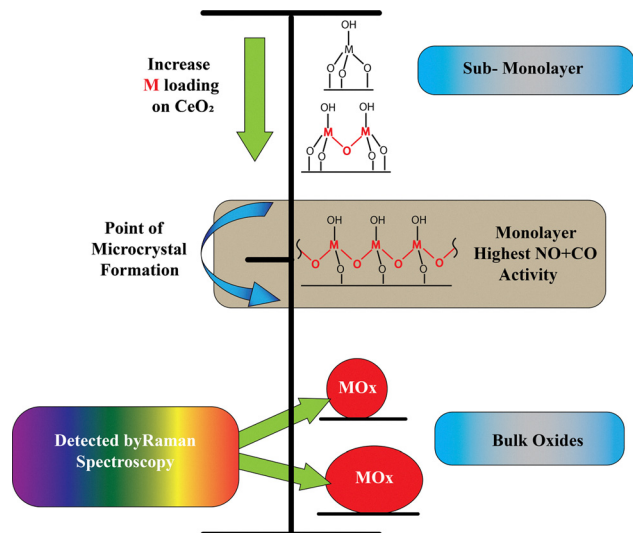
**Fig. 8** Structure and activity relationship of ceria-supported Fe and Co oxides for NO reduction by CO.[105] Reproduced with permission from the American Chemical Society (Copyright©2017).

basicity.[75] Their advantages include improved stability, control and efficiency compared to other reaction systems. Because of their flexible structure, hydrotalcite-derived transition metal oxides are considered very active and selective catalysts, even far more efficient than zeolitic catalysts. They are also thermally very stable. When using hydrotalcite catalysts, $N_2O$ decomposes below 500 K. Another benefit of calcined hydrotalcites is that they do not degrade at temperatures above 900 K, thus the high stability makes the hydrotalcite-derived catalysts quite promising for practical applications. Higher calcination temperatures combined with alkali promoters (i.e. K) have a great enhancing impact on the $N_2O$ decomposition activity. However, water and oxygen are strong inhibitors of the $N_2O$ conversion performance.[137]

The overall rate of $N_2O$ decomposition reaction depends on the adsorption of $N_2O$ molecules on the catalyst surface during the reaction. This adsorption is a crucial step in the decomposition process. The rapid formation of $O_2$ led to the fast desorption of adsorbed oxygen, making active sites on the catalyst surface available for further adsorption of $N_2O$. As a result of fast adsorption and desorption processes, the overall rate of $N_2O$ decomposition is higher. This led to the establishment of first-order rate equation w.r.t the concentration of $N_2O$.[138]

Layered double hydroxides (LDHs) are successfully employed as starting materials for metal-supported catalysts. Generally, they are synthesized via three distinct routes: (1) with elements of redox properties present in between the layer spacing, direct calcination and/or reduction of LDH precursors is required, (2) within the LDH sheets, anionic exchange with the desired metal precursors is crucial, followed by calcination and/or reduction and (3) pre-calcined LDH precursors are impregnated with different inorganic materials followed by calcination and/or reduction.[139] Fig. 9a summarizes all three routes for the synthesis of LDH-derived metal-supported catalysts.

Oxygen molecules tend to adsorb on the catalyst's surface and occupy the active sites, reducing the availability of free active sites for the $N_2O$ decomposition reaction. As a result, the overall $N_2O$ decomposition rate decreases. The Eley–Rideal reaction, that involves the desorption of oxygen, is not active enough to drive the overall $N_2O$ decomposition reaction within the temperature range of 250 °C and 500 °C. This behaviour of oxygen in $N_2O$ decomposition process is different from selective catalytic reduction (SCR) processes where oxygen plays a key role in breaking down organic molecules to produce $N_2$ from nitrogen oxides.[142] A first-order reaction rate model can be employed to describe the decomposition of $N_2O$, but it is only applicable when the concentration of $N_2O$ is less than 10 000 ppm. Beyond this range, the reaction kinetics deviate from the first-order behaviour. The presence of impurities in the feed gas can get adsorbed on the active sites of the catalysts, resulting in free defect sites on the surface, which can slowly decrease the rate of $N_2O$ decomposition.[21] De Stefanis et al. used catalysts consisting of alumina-pillared smectites, which are a type of layered clay material. These clay materials were exchanged with transition metals.[143] The main focus of this study was to reduce $N_2O$ via an eco-friendly decomposition reaction as follows:

$$N_2O \rightarrow N_2 + 1/2O_2$$
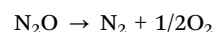
This reaction converts $N_2O$ into less harmful nitrogen ($N_2$) and oxygen ($O_2$). The results of this study showed that when pillared clays were exchanged with transition metals, the yield of decomposition reaction increased, suggesting that catalysts with transition metals are effective in promoting the $N_2O$ decomposition rate. It was noted that double-exchanged alumina-pillared montmorillonite/beidellite catalysts, exchanged with Ca and Co ions, exhibited the highest decomposition activity for $N_2O$. Overall, the mechanism suggested that $N_2O$ is first adsorbed on the catalyst surface. Then, it underwent decomposition through catalytic oxidation and reduction.[143] Similarly, Zhang et al. synthesized La-hexaaluminates ($LaFe_xAl_{12-x}O_{19}$) having abundant Al sites in the mirror plane (MP) phase, so that the degradation of $N_2O$ can be achieved efficiently. Fig. 9b demonstrates that Fe(III) ions prefer to occupy octahedral Al(III) sites in the MP of aluminate crystals confirming a high activity for $N_2O$ decomposition.[140] Kiss et al. reported AlFe–PILC-type catalysts having different metal/OH ratios and employed them for $N_2O$ decomposition reactions.[144] $N_2O$ was 100% converted into $N_2$ and $H_2O$ on treatment with $NH_3$ below 500 °C. However, in the direct conversion of $N_2O$ below 500 °C, the activity of catalysts did not exceed 40%. For the $N_2O$ abatement reaction, the catalytic activities of AlFe–PILC-type catalysts prepared with higher metal/OH ratios are higher than the apparent activity of AlFe–PILC-type catalysts having lower metal/OH ratios. It is attributed to the presence of free $FeO–Fe_2O_3$ particles.[145]

Hydrotalcites have been effectively utilized for dual decomposition of volatile organic compounds (VOCs) and gaseous pollutants. For instance, fabricated and calcined $Cu_xMg_{3-x}AlO$ were examined for 100% primary catalytic oxidation of n-butylamine and 83% secondary catalytic reduction of $NO_x$ at a lower temperature of 350 °C, as represented in Fig. 9c.[141]

**Table 4** Overview of synthesis methods, reaction conditions and various techniques employed during the course of analysis of different mixed metal oxide catalysts for $N_2O$ decomposition

| Catalysts | Methods | Reaction atmosphere | Air speed (mL min⁻¹) | N₂O decomposition temp-range (°C K⁻¹) | Techniques used for characterization and activity of catalysts | Ref. |
|---|---|---|---|---|---|---|
| Cu/CeO₂ | Hydrothermal | H₂/Ar | 25 | 300–450 °C | STEM-EDX, STEM-EELS, H₂-TPR, XPS, *operando* DRS-UV-Vis, DRIFTS, CO-DRIFTS | 109 |
| Rh/CeO₂ | Hydrothermal | H₂/Ar | 40 | 400 °C | CO-DRIFTS, N₂O-DRIFTS, MCT detector, IR | 110 |
| RuO₂/Al₂O₃ | Wet impregnation | N₂ | 1000 | 25–300 °C | BET surface area measurement, XRD, FT-IR, DBD reactor | 111 |
| Ru/Al₂O₃ | Impregnation | He | 20 | 250–500 °C | — | 112 |
| PrBaCoCO₃ | Hydrothermal | He | 100 | 200–600 °C | XPS, BET, H₂-TPR, O₂-TPR | 25 |
| Cu–Al–Oₓ mixed metal oxides | Co-precipitation method | He | 100 | 300–450 °C | XRD, ICP-MS, N₂ physisorption, O₂-TPD, H₂-TPR, *in situ* FT-IR and XAFS | 113 |
| Metal oxides supported Au-NPs (Au/MₓOᵧ) (MₓOᵧ: Al₂O₃, CeO₂, Fe₂O₃, TiO₂ and ZnO) | Deposition precipitation | He | 10 | 400–700 °C | BET, XRD, SEM, HR-TEM, XPS, H₂-TPR, EDS, GC-TCD | 114 |
| Co₃O₄/CeO₂ mixed oxide catalysts | Hydrothermal | He | 100 | 300–600 °C | BET, XRD, TEM, H₂-TPR, XPS, GC-TCD | 115 |
| K-modified Co–Mn–Al mixed oxides | Hydrothermal | He | 50 | 250–450 °C | ICP, XPRD, H₂-TPR, CO₂-TPD, NO-TPD, XPS, N₂-sorption | 116 |
| Co₃O₄/ZrO₂ | Hydrothermal | He | 30 | 200–400 °C | XRD, TEM, HRTEM, N₂-physisorption, FTIR, XPS, O₂-TPD, H₂-TPR, GC, Raman | 117 |
| K/Y₂O₃–Co₃O₄ | Co-precipitation | He/Ar | 20 | 100–400 °C | BET, DTA | 118 |
| Nd(Cu,Co)Al-Oₓ | Co-precipitation | O₂/He | 100 | 50–600 °C | XRD, BET, HRTEM, XPS, H₂-TPR | 119 |
| Co₃O₄–LaCoO₃ | Co-precipitation | He | 40 | 700–850 °C | XRD, BET, FTIR | 120 |
| MnₓCo₁₋ₓCo₂O₄ | Co-precipitation | He | 40 | 100–500 °C | XRF, XRD | 121 |
| LaFeO₃ | Hydrothermal | — | — | 250–500 °C | XRD, EDX, XPS | 122 |
| MnOₓ/TiO₂ | Ultrasonic impregnation | N₂ | 1000 | 0–400 °C | XRD, EDX, SEM | 123 |
| CuFeOₓ thin-film catalysts | Adsorption | Ar | 20 | 100–550 °C | XRD, EDX, XPS | 124 |
| MnO₂/MOₓ (M = Al, Si and Ti) | Wet impregnation | He | 60 | 120–280 °C | XRD, XPS, BET | 125 |
| MnOₓ/TiO₂ | Wet impregnation | — | — | 100–300 °C | XRD, BET, HRTEM, XPS, H₂-TPR and NH₃-TPD | 126 |
| Pd/CeO₂ | Hydrothermal | NH₃/He | 20 | 100–400 °C | XRD, XPS, TEM, FEI | 127 |
| Pt/Co₃O₄ | Incipient-wetness | H2/Ar | 35 | 100–500 °C | XRD, SEM, TEM, TPO, TPR | 128 |
| MnOₓ/TiO₂ | Ultrasonic impregnation | O₂/Ar/NO/NH₃ | 1000 | 0–350 °C | XRD, SEM, XPS, BET | 129 |
| Cs-supported Co₃O₄ (Cs/Co) | Co-precipitation | Ar | 100 | 100–300 °C | XRD, XPS, H₂-TPR | 130 |
| Bi₀.₁NiO₁.₁₅ | Co-precipitation | N₂/O₂ | 3100 | 300–400 °C | XRD, XPS, H₂-TPR | 131 |
| CuO/CeO₂ | Co-precipitation | — | — | 300–550 °C | STEM, EDX, XRD | 132 |
| Pd/γ-Al₂O₃ | Impregnation | N₂ | 6 | 550–350 °C | XRD, XPS | 18 |
| Rh/PTA | — | — | — | — | DFT | 38 |
| P@SiC | Adsorption | — | — | — | DFT, PDOS | 133 |
| (SACs) M1/PTA (M = Fe, Co, Mn, Ru, Rh, Os, Ir & Pt; PTA = [PW₁₂O₄₀]³⁻) | Ion exchange | — | — | — | DFT | 134 |
| Fe-substituted La-hexaaluminate supported Ir catalysts | Microemulsion | He | 50 | 384–450 °C | XRD, XPS, DRFTS | 135 |
| Rh/CeO₂ | Incipient wetness impregnation | Ar | 30 | 300–500 °C | XRD, STEM, EDS, HRTEM, XPS, FTIR, DRIFTS | 136 |
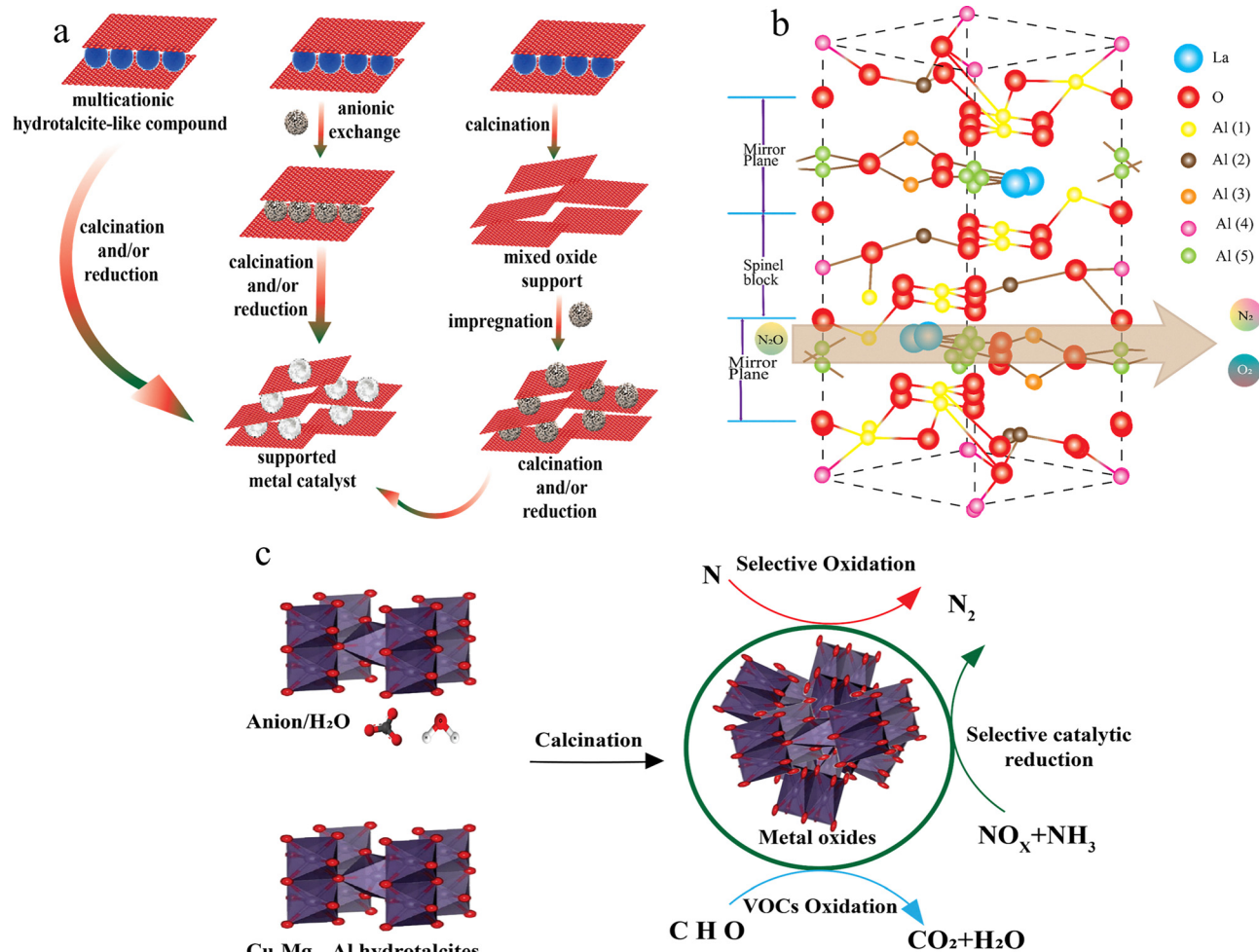
**Fig. 9** (a) Representation of main routes leading to the synthesis of metal-supported catalysts from LDH precursors.[139] Reproduced with permission from Springer (Copyright©2003). (b) $N_2O$ decomposition to $N_2$ and $O_2$ in the mirror plane phase of perovskite-type La-hexaaluminates (LaFe$_{x-}$Al$_{12-x}$O$_{19}$).[140] Reproduced with permission from the American Chemical Society (Copyright©2014). (c) Hydrotalcite-derived Cu$_x$Mg$_{3-x}$AlO oxides for pollutant-destruction mechanism.[141] Reproduced with permission from the American Chemical Society (Copyright©2019).

In another study, catalytic decomposition of $N_2O$ was estimated at Co/Al hydrotalcites, $[Co_{1-x}Al_x(OH)_2[(CO_3)]_{x/2} \cdot H_2O]$ (where $x \approx 0.25-0.33$), in a static glass reactor at a pressure of $\approx 50$ torr within the temperature range of 150–280 °C. Catalysts exhibited a first-order dependence for the $N_2O$ decomposition activity. An increase in Co concentration led to an increased decomposition activity. A higher activity was shown by the catalyst precursor synthesized under a low saturation (LS) method than that synthesized by a sequential precipitation (SP) method.[146] Table 5 presents various examples of hydrotalcites that have been applied for $N_2O$ decomposition.

*5.2.1.1. Shortcomings of hydrotalcite catalysts.* Hydrotalcite catalysts, while offering tunable composition and high dispersion of active sites, suffer from several drawbacks. Their thermal stability is limited, as structural collapse can occur upon high-temperature calcination. The resulting mixed metal oxides may exhibit low surface area and poor crystallinity. Additionally, their activity in $N_2O$ decomposition is generally

moderate, requiring further modifications. Sensitivity to water and contaminants can also affect the long-term performance and catalyst durability.

*5.2.1.2. Application scenario: automotive exhaust control.* These catalysts with layered double hydroxide structures offer high surface area, tunable composition, and excellent dispersion of active metal sites, making them promising for $N_2O$ decomposition in automotive exhaust systems. They are low cost and versatile but disadvantages include limited intrinsic activity, dependence on metal modification for efficiency and reduced stability under high-temperature, water and sulphur-rich exhaust conditions.

**5.2.2. Zeolites with transition metal ions.** Zeolite catalysts are among the few early known catalysts for $N_2O$ decomposition, while some show catalytic activities below 600 K.[156] The activity of transition metal ion-exchanged zeolite was determined by the type of transition metal ion (TMI) and zeolite. This is the reason that the activity order for different transition

**Table 5** Overview of synthesis methods, reaction conditions and various techniques employed during the course of analysis of different hydrotalcite catalysts for $N_2O$ decomposition

| Catalysts | Preparation method | Reaction atmosphere | Air speed (mL min$^{-1}$) | Decomposition temp-range (°C K$^{-1}$) | Techniques used for characterization and activity of catalysts | Ref. |
|---|---|---|---|---|---|---|
| Mn(Fe)CoAlO$_x$ hydrotalcite | Co-precipitation | N$_2$ | 100 | 100–500 °C | XRD, H$_2$-TPR, TGA, XPS, XAFS, BET | 147 |
| Ru/Me$_x$O$_y$ | Hydrothermal | — | — | 300–550 °C | CO$_2$-TPD, TEM | 148 |
| Rh/Mg/Al HT-derived film | Co-precipitation | H$_2$/Ar | 30 | 50–500 °C | SEM, EDX, TEM, SAED, BET, Raman, H$_2$-TPR, XPS | 149 |
| Hydrotalcite-derived Cu$_x$Co$_y$ (CuO–Co$_3$O$_4$ mixed oxides) | Co-precipitation | N$_2$ | 100 | 350–500 °C | XRD, XPS | 150 |
| Hydrotalcite-derived mixed oxides | Ion exchange | H$_2$ | 200 | 300–500 °C | XRD, XPS, BET | 151 |
| Hydrotalcite-derived Co$_3$O$_4$, Co$_3$O$_4$–P | Sol–gel method | — | — | 150–400 °C | TEM, TGA, XRD and BET | 152 |
| Hydrotalcite-derived [y = Cu/(Cu + Ni)] | Co-precipitation | H$_2$/Ar | 41 | 600–900 °C | XRD, XPS, TGA-DTA, BET, XPS | 153 |
| CoCuAl mixed oxides derived from hydrotalcites | Solid phase | H$_2$/Ar | 60 | 150–350 °C | XRD, N$_2$-physisorption, H$_2$-TPR | 154 |
| Al@Cu-based hydrotalcite CuAl-HT-c and Cu-P | Co-precipitation | NO/He CO/He | 8 8 | 450–600 K | XRD, TPR and in situ XANES | 155 |

metals in zeolite catalysts differs considerably from other metal oxide catalysts. One major advantage associated with zeolite catalysts is that the higher oxygen concentration shows a very small inhibitory effect on their catalytic efficiency, but one disadvantage associated with Rh-exchanged zeolites is their extreme sensitivity to water.[60]

Transition metal ions in zeolites, supported on oxides, or dispersed in solid solutions, are very active for $N_2O$ decomposition.[157,158] Numerous zeolites with transition metal ions are extensively studied in heterogeneous catalysis. A zeolite's ion-exchange capacity (IEC) depends on how it is chemically composed. A higher IEC is perceived in the zeolites having low $SiO_2/Al_2O_3$ ratios. Specific ion-exchange capacity of a zeolite varies by varying the structure of zeolites and cations exchanged. When a wet ion exchange (WIE) method was used for the preparation of Fe–ZSM-5, Lobree et al. were able to achieve only half of the complete IEC without getting small iron oxide particles.[159]

Natural zeolites show low activity for the catalytic reduction of $N_2O$ using $NH_3$ due to the complex structures of zeolites.[160] However, when natural zeolites were modified with Fe, their activity in the SCR of $N_2O$ became comparable to synthetic zeolites. It was found that the highest activity of $N_2O$ decomposition was achieved when natural zeolites contained 6.5 wt% Fe.

Natural zeolites prepared with $FeCl_2$ as the precursor exhibited higher activity for the reduction of $N_2O$ due to the formation of more reducible Fe species with $FeCl_2$.[160] Zeolites prepared with $FeSO_4$ as the precursor showed a considerably lower activity for the decomposition of $N_2O$ as surface sulphate ions were identified as inhibitors, and their presence shifted the reaction temperature to higher values. It is suggested that natural zeolites, especially when modified with Fe, can serve as a cost-effective alternative for catalysing the SCR of $N_2O$, as they demonstrated comparable activity to synthetic zeolites.[161,162]

Most active catalysts for $N_2O$ decomposition are usually inhibited by NO. This suggests that NO can interfere with the process of breaking down $N_2O$ into less harmful components. However, interestingly enough, NO can significantly enhance the rate of $N_2O$ decomposition over a specific catalyst, Fe–ZSM-5. Pérez-Ramírez et al. were first to report this positive effect of NO on $N_2O$ decomposition over Fe–ZSM-5. They proposed a mechanism where NO in the gas phase combines with both $N_2O$ and adsorbed $O_2$, leading to the regeneration of active sites and the production of nitrogen oxide. This mechanism explains the increase in the $N_2O$ decomposition rate due to NO.[61] However, Li and Armor reported that zeolites exchanged with Co or Cu ions were effective catalysts for $N_2O$ decomposition, and that metal ions (particularly Co, Cu, and Fe) in ZSM-5 were far more active than the same ions on $Al_2O_3$.[163] On Cu–ZSM-5, Fe–ZSM-5 and Co–ZSM-5, the $N_2O$ decomposition rate was proportional to the exchange extent. The existence of excess $O_2$ left the catalytic activity of Co–ZSM-5 unchanged and slightly decreased Cu–ZSM-5 activity, but enhanced the catalytic activity of Fe–ZSM-5.[164] Conversely, $H_2O$ present in the feed strongly affected the catalytic activity of zeolites and led to irreversible deactivation because of its heterolytic adsorption on active sites. In the presence of water vapours, Co–ZSM-5 was more

stable than Cu–ZSM-5 and Fe–ZSM-5.[165] For the decomposition of N$_2$O into its elements, TMI-exchanged pentasil-zeolites are recognized as most appropriate catalysts. Among the samples investigated, the highest N$_2$O decomposition activity was displayed by Cu–ZSM-5 catalysts.[166] Therefore, Deka et al. have carried out an extensive investigation on the use of Cu-exchanged zeolite-based catalysts (that include zeolite Y, ZSM-5, SSZ-13 and zeolite beta) for the abatement of NO$_x$ present in the exhaust emissions of light and heavy-duty vehicle engines.[11] However, Cu–ZSM-5 has a tendency to lose activity in the presence of H$_2$O vapours limiting its use in practical applications. However, Fe-containing zeolites are less sensitive towards H$_2$O vapours in comparison to Cu-containing zeolite.[167] Liu et al. studied N$_2$O formation using Cu–SSZ-13 zeolites via the NH$_3$-asssited SCR of NO$_x$. All reactions were performed in a flow reactor system, as shown in Fig. 10. It was found out that N$_2$O formation occurred through two entirely different mechanisms at low and high temperatures. At low temperatures, N$_2$O was released due to the decomposition of NH$_4$NO$_3$ on Cu–SSZ-13 zeolite, while high temperatures favoured the NH$_3$ oxidation route for N$_2$O formation.[168]

Yasumura et al. demonstrated an efficient strategy for the dispersion of metal species to design single-atom catalysts. Chabazite (CHA) zeolite precursors were utilized as templates to disperse bulk Pd atoms into their small pores.[169] At 600 °C, the flow of feed gas was regulated in such a way that Pd atoms present on the outside of CHA zeolites can get dispersed introducing Pd(II) ions into the pores of zeolite forming Pd–CHA zeolites along with the formation of N$_2$O. Fig. 11a illustrates the conversion of bulk Pd and CHA zeolites into Pd(II)-intercalated zeolites.

It has been observed that adsorbed NH$_3$ leaves the active sites by reaction with the surface O$_2$. As NH$_3$, as a reducing



**Fig. 10** Experimental setup of N$_2$O formation during the selective catalytic reduction of NO$_x$ with NH$_3$ over Cu–SSZ-13.[168] Reproduced with permission from the American Chemical Society (Copyright©2019).

agent, preferably reacts with O$_2$, the N$_2$O decomposition process becomes suppressed due to the presence of surface O$_2$. As a result, a vast majority of studies on the SCR of N$_2$O have been devoted to Fe-exchanged zeolite catalytic systems, more specifically, the Fe–BEA catalysts.[171,172] The N$_2$O abatement by NH$_3$ follows the Mars and Van Krevelen mechanism that involves an oxidation–reduction cycle of interchange between two oxidation states of Fe (Fe$^{3+}$ ↔ Fe$^{2+}$). In this scenario, N$_2$O reduction into oxygen surface species occurs over some definite Fe-sites, which lead to simultaneous N$_2$ release. Consequently, O$_2$ has no inhibitory influence on N$_2$O decomposition through NH$_3$.[173] In Fig. 11b, it can be noted that the presence of O$_2$ does not hinder the conversion of N$_2$O. In fact, there was small improvement in N$_2$O conversion when O$_2$ was present. This suggested that O$_2$ did not negatively impact the conversion of N$_2$O. Fig. 11d demonstrates that the enhanced reduction of N$_2$O was associated with the oxidation of NH$_3$, which could change the NH$_3$/N$_2$O stoichiometry. In the absence of O$_2$, the highest N$_2$O conversion occurred at around 3500 ppm of NH$_3$ concentration. In contrast, in the excess of O$_2$, the highest N$_2$O removal occurred at around 4000 ppm of NH$_3$ concentration. This also suggested that O$_2$ did not significantly interfere with N$_2$O decomposition and did not efficiently react with NH$_3$. Fig. 11c indicates that the oxidation of NH$_3$ by O$_2$ was much less significant when N$_2$O was present compared to when N$_2$O was absent. This suggested that in the reaction system involving N$_2$O, NH$_3$ and O$_2$, the selective catalytic reduction (SCR) of N$_2$O by NH$_3$ was more dominant than the oxidation of NH$_3$ by O$_2$. Fig. 11e shows that when NH$_3$ is oxidized by O$_2$, it produces a large amount of NO, NO$_2$ and N$_2$O. However, in the N$_2$O + NH$_3$ + O$_2$ reaction system, only N$_2$ is detected as the main product. This indicated that NH$_3$ can be oxidized by both O$_2$ and N$_2$O, but N$_2$O is much more reactive than O$_2$, and their reaction pathways are distinct.[170]

Ju et al. have found that UV irradiation of the Pb$^{2+}$–ZSM-5 catalyst led to the decomposition of N$_2$O at 298 K in a linear manner with the irradiation time.[174] It can be confirmed by observing the yield of N$_2$ that increases as a function of the UV-exposure time, while under dark conditions, the formation could not be noticed. The yield of N$_2$ also increases when the amount of Pb$^{2+}$ loading becomes higher. It was reported that the photocatalytic decomposition of N$_2$O proceeds much more efficiently in the presence of propane.[130] In addition to the N$_2$ evolution, this reaction also led to the formation of oxygen-containing compounds such as ethanol and acetone. It was indicated that the efficient decomposition of N$_2$O proceeds photocatalytically in the presence of propane on the Pb$^{2+}$–ZSM-5 catalysts. The efficiency of the photocatalytic reduction of N$_2$O is found to be strongly dependent on the type of hydrocarbons used, e.g. methane or ethane, and among the hydrocarbons, the highest enhancement in the reaction rate is shown by propane. These results can be attributed to the observation that during the reaction, oxygen atoms formed by the photodecomposition of N$_2$O detach more easily from the isolated Pb$^{2+}$ ions in the presence of propane.[174] Similarly, Co-based BEA zeolite catalysts were also used to study the oxidative
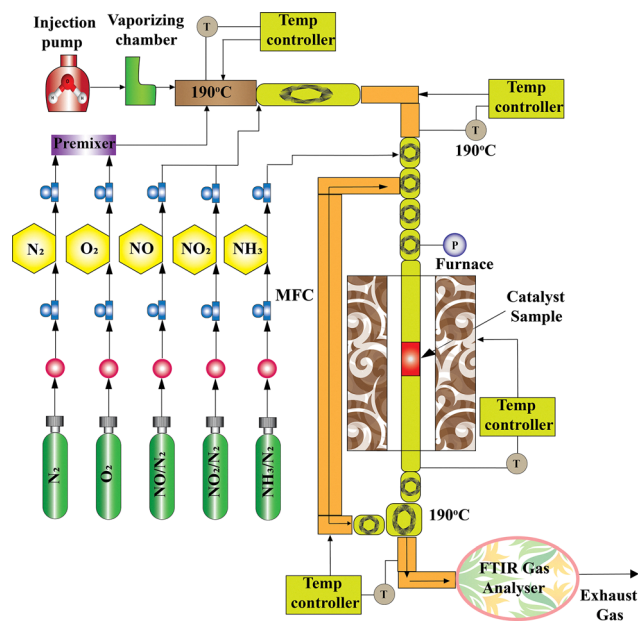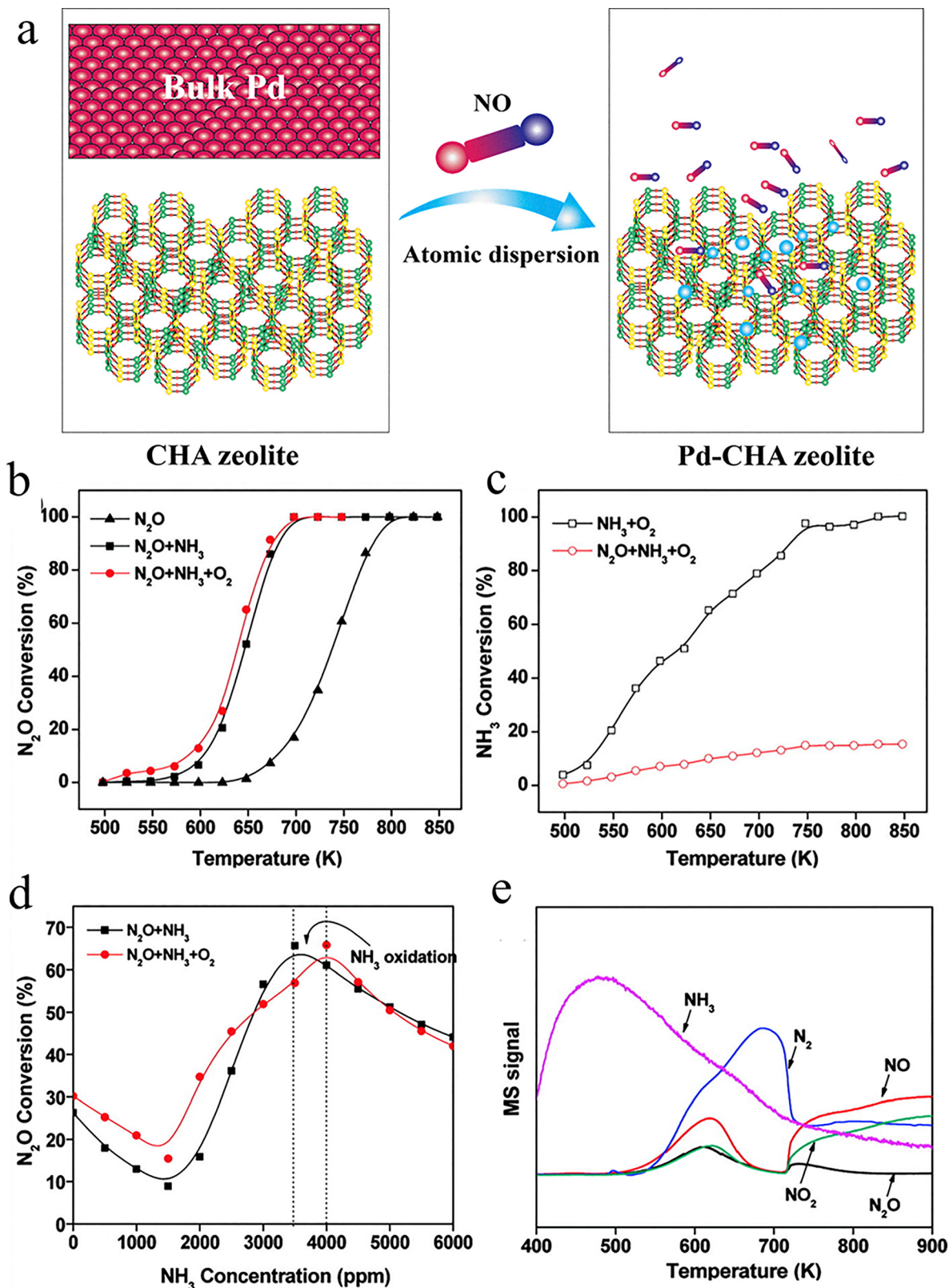
Fig. 11  (a) Transformation of bulk Pd to Pd cations in small-pore CHA zeolites facilitated by NO.[169] Reproduced with permission from the American Chemical Society (Copyright©2021). (b) Decomposition of $N_2O$ (%) via selective catalytic reduction (SCR) through $NH_3$ on Fe-MOR catalysts. (c) Decomposition of $NH_3$ (%) by oxidation of $NH_3$ with and without $N_2O$. (d) Decomposition of $N_2O$ (%) via $NH_3$ as a function of $P(NH_3)$ with and without $O_2$ and e. TPSR profiles of oxidation of $NH_3$ (conditions: 100 mg catalyst, 0 or 4000 ppm $NH_3$, 0 or 5% $O_2$, 5000 ppm $N_2O$, and balance He. GHSV = 30 000 h$^{-1}$).[170] Reproduced with permission from the American Chemical Society (Copyright©2012).

dehydrogenation of propane ($C_3H_8$) with $N_2O$ or a mixture of $N_2O$ and oxygen ($O_2$) as the oxidants. $N_2O$ is more selective but less active compared to $O_2$ as an oxidizing agent. Increasing the concentration of $N_2O$ in the reaction mixture with $C_3H_8$ and $O_2$ led to a substantial increase in propane conversion while maintaining a constant selectivity for propene. The combination of $O_2$ and $N_2O$ had a synergistic effect, resulting in a three-fold higher yield of propene compared using $O_2$ and $N_2O$ alone.[175] Table 6 summarizes various examples of catalysts used along with the techniques applied during the course of analysis for the purpose of $N_2O$ decomposition.

*5.2.2.1. Shortcomings of zeolite catalysts.* Zeolite catalysts, despite their well-defined microporous structures and strong metal–support interactions, have notable limitations in $N_2O$ decomposition. Their narrow pore sizes can restrict the diffusion of reactants and products, especially at higher conversions. Metal ion exchange may lead to non-uniform dispersion or clustering, reducing active site accessibility. Thermal stability under prolonged high-temperature reactions can be a concern, leading to framework degradation. Additionally, zeolites are sensitive to water vapours and contaminants such as sulphur, which can cause deactivation and limit their industrial applicability.

*5.2.2.2. Application scenario: diesel vehicle exhaust mechanism.* These catalysts are highly effective for $N_2O$ decomposition in diesel exhaust due to their high surface area, tunable acidity and excellent hydrothermal stability. They enable selective catalytic reduction with $NH_3$, offering high efficiency at medium temperatures. However, they are sensitive to sulphur poisoning, may deactivate under prolonged hydrothermal stress, and require careful formulation for durability.

**5.2.3. Mixed metal oxides in mesoporous silica.** After the discovery of well-organized mesoporous molecular sieves, scientific community has developed interest in their catalytic applications. Discovered by Mobil researchers, these mesoporous silica-supported catalysts possess a higher surface area than the conventional zeolite-based catalysts. Owing to their fascinating properties, these materials play an important role to support the other co-catalysts in many catalytic reactions.[204]

For example, SBA-15 is a mesoporous silica material with a fibre-like morphology that is several tens of micrometers long. It possesses a 2D porous structure and unique properties.[205,206] It has various applications including its use as a support material for Rh catalysts in $N_2O$ abatement with Rh being one of the most active metals in $N_2O$ decomposition. Different mesoporous silica-supported metal ions are crucial with regard to their $N_2O$ abatement activity and age resistance, but among them Rh/SBA-15–S is found to be most active and durable. It is well known because of its superior performance in the presence of $O_2$ which is typically an inhibiting agent. This is attributed to the large pore size of Rh/SBA-15–S that enhances catalyst's access, diffusion and dispersion. The smaller particle size of Rh in Rh/SBA-15–S results in the higher dispersion of metals on the catalyst surface. It favours the formation of more $Rh^+$ ions

than $Rh^0$ or $Rh^{3+}$, which, in turn, leads to higher $N_2O$ decomposition activity. Rh/SBA-15–S is found to be durable, maintaining its performance at a temperature of 430 °C. This suggests its suitability as a support material in long-term applications and further research.[207] Similarly, Wei *et al.* reported the synthesis of a highly dispersed and well-homogenized bimetallic Au–Pd alloy supported on amine-functionalized SBA-15. The catalytic activities, when tested from 150 °C to 600 °C, revealed a decreasing trend with the increase in the percentage of Au in bimetallic alloy catalysts (Fig. 12a). It led to the conclusion that the addition of Au negatively affects the activity of Pd catalysts. Though on the one hand, the Au–Pd alloy facilitates the desorption of $O_2$ molecules, on the other hand, it affects other elementary steps that change the rate-determining step. Fig. 12b depicts the energy profiles of $N_2O$ degradation over Pd, $Pd_3Au$/Pd and $PdAu_3$/Pd catalyst's surface, which has been split into three processes, *i.e.* (a) decomposition of $N_2O$ into $N_2$ and O atoms, (b) diffusion of O atoms on the surface of catalysts and (c) recombination of two O atoms to form $O_2$. The respective mechanisms of degradation are shown in Fig. 12c–k.[208] Various other examples of such catalysts are summarized in Table 7.

*5.2.3.1. Shortcomings of mesoporous silica-supported metal oxide catalysts.* Mesoporous silica-supported metal oxide catalysts often suffer from weak metal-support interactions, leading to metal sintering or leaching under harsh conditions. Their thermal and hydrothermal stability is generally lower than that of crystalline supports like zeolites. Additionally, achieving uniform metal dispersion can be a challenge, and their catalytic activity may decline over time due to the structural degradation or active site deactivation.

*5.2.3.2. Application scenario: chemical plant emissions.* Mixed metal oxides dispersed in mesoporous silica supports provide high surface area, uniform metal dispersion and enhanced redox properties, making them effective for $N_2O$ decomposition in chemical plant emissions. They offer thermal stability and tenability, but disadvantages include susceptibility to pore blockage, reduced activity under humid or sulphur-rich conditions, and higher synthesis complexity.

## 5.3. Nanostructured metal-doped materials

Nanostructured metal-doped materials exhibit high surface area, quantum size effects, and unique electronic properties. Doping enhances the catalytic activity by modifying charge distribution and creating active sites. Their tunable morphology – nanosheets, nanotubes or cages – improves reactant accessibility. These materials often show superior thermal stability, reactivity, and selectivity, making them promising candidates for advanced catalytic applications like $N_2O$ decomposition.

**5.3.1. Metal-doped nanotubes, nanosheets and nanocages.** Nanotubes, nanosheets and nanocages are elongated, 2D and cage-like structures, respectively, possessing large surface area, crystallinity, high porosity, hollow structure and astonishing electrical and mechanical properties, rendering them novel and excellent choice of catalyst for $N_2O$ decomposition due to a

**Table 6** Overview of synthesis methods, reaction conditions and various techniques employed during the course of analysis of different zeolite catalysts for N₂O decomposition

| Catalysts | Preparation method | Reaction atmosphere | Air speed (mL min⁻¹) | Decomposition temp-range (°C K⁻¹) | Techniques used for characterization and activity of catalysts | Ref. |
|---|---|---|---|---|---|---|
| Co–, Cu– and Fe–SSZ-13 zeolites | Hydrothermal | N₂ / H₂/Ar | 10 / 30 | 300–530 K | XRD, FT-IR, H₂-TPR, N₂O-TPR | 27 |
| Rh–ZSM catalysts | Incipient wetness | He/Ar | 70 | 250–450 °C | STEM, XPS, TPR, N₂O-DRIFTS | 104 |
| CoMnAl HTC catalysts | Co-precipitation | He | 25 | 330–460 °C | SEM, EDX, XRD, NH₃-TPD, CO₂-TPD, H₂-TPR, BET | 157 |
| Cu–ZSM-5 catalysts | Ion exchange | NH₃/He | 30 | 200–600 °C | BET, XRD, TEM, CO₂-TPR, NH₃-TPR, GC–TCD | 176 |
| Fe–ZSM-5 | Hydrothermal | He/Ar | 15 | 550–750 K | N₂O-TPD, O₂-TPD, NO-TPD, AAS | 177 |
| Co–ZSM-5 | Hydrothermal | He/O₂ | 25 | 380–500 °C | SEM, XRD, NH₃-TPD, H₂-TPR, ICP-AES, UV-Vis-DRS, DFT | 178 |
| Co/zeolites (Co/Beta, Co/mordenite, Co/ZSM-5, Co/MCM-49, Co/ZSM-23, Co/SSZ-13) | Wet impregnation | N₂ | 30 | 200–450 °C | XRD, BET, NH₃-TPD, H₂-TPR, XPS UV-Vis-DRS, | 179 |
| Fe–, Co–, Ni– and Cu–ZSM-5 catalysts | Ion exchange | Ar | 4 | 400–800 °C | DFT, TPR | 158 |
| Fe, Co and Ni-exchanged Na-MOR catalysts (Fe–MOR, Co–MOR and Ni–MOR catalysts) | Ion exchange | O₂/He | 100 | 293–773 K | GC, TCD, FID, *operando* FTIR equipped with MCT detector | 180 |
| Cu/ZSM-5 catalysts | Adsorption | N₂ | 40 | 250–500 °C | ICP-AES, UV-Vis-DRS, H₂-TPR, N₂O-TPD | 181 |
| Cu–ZSM-5 catalysts | Adsorption | — | — | — | DFT | 182 |
| Fe-zeolites (Fe–PST-7, Fe–LTA, Fe–RTH, Fe–SSZ-13, Fe–FER, Fe–ZSM-5) | Hydrothermal | He | 55 | 600–850 °C | XRD, SEM, TEM, BET, UV-vis, ESR, FTIR, NMR | 183 |
| Cu–ZSM-5 catalysts | Hydrothermal | — | — | 600–800 K | H₂-TPR, IR | 184 |
| Cu–ZSM-5 catalysts | Ion exchange | N₂O/N₂ | 300 | 350–450 °C | H₂-TPR, IR, BET, H₂-TPR, TPD, FESEM, EDX | 151 |
| Cu–, Ni–, Zn–, Co–, Fe– and Mn–ZSM-5 catalysts | Ion exchange | N₂ | 300 | 50–300 °C | DFT, N₂O-TPD, GC–TCD, FT-IR, BET, ICP-OES | 185 |
| Fe–ZSM-5 catalysts | Wet impregnation | N₂ | 30 | 250–550 °C | XRD, XPS, BET, HRTEM, UV-Vis-DRS, XPS, H₂-TPR, TPO, DRIFTS | 186 |
| Cu/HZSM-5 catalysts | Wet impregnation | N₂ | 60 | 620 K | FTIR, XPS, XPRD | 187 |
| Co/HZSM-5 catalysts | Citric acid impregnation | O₂/Ar | 80 | 300–450 °C | XRD, TG–DSC, Raman, SEM, H₂-TPR, XPS, EPR, FTIR, DRIFTS | 188 |
| Fe–ZSM-5 catalysts | Hydrothermal | N₂ | 20 | 300–600 °C | XRD, SEM, BET, UV-vis, FTIR | 189 |
| Fe–ZSM-5, Fe-Beta, Fe–FER catalysts | Wet impregnation | He | 70 | 200–400 °C | FTIR, BET, H₂-TPR, TGA-MS | 190 |
| Fe-beta, Fe–ZSM-5 and Fe–SAPO-34 catalysts | Ion exchange | H₂/Ar | 30 | 200–400 °C | UV-vis-DRS, H₂-TPR | 191 |
| Fe–SSZ-13 catalysts | Ion exchange | He | 103 | 400–600 °C | ICP-AES, BET, UV-vis-DRS, XRD, TEM, On-line GC–TCD | 192 |
| Fe/CHA catalysts | Ion exchange | N₂ | 80 | 160–550 °C | XRD, ICP-OES, DFT, TEM, EDX, XPS, EPR, FTIR, H₂-TPR | 193 |
| Fe-modified MCM-22 zeolite and its derivative ITQ-2 catalysts | Ion exchange | Ar | 10 | 200–600 °C | XRD, ICP-OES, UV-vis-DRS, H₂-TPR, HRTEM | 161 |
| (Co, Fe)–ZSM-5 and (Co, Fe)-beta catalysts | Ion exchange | Ar | 30 | 25–600 °C | XRD, H₂-TPR, UV-vis, TCD | 165 |
| Cu/SSZ-13, Cu/SSZ-5, Cu/BEA | Ion exchange | O₂ | 2 | 100–500 °C | XRD, BET, DRIFTS, FTIR, H₂-TPR, NH₃-TPD | 194 |
| Co(x)/PRSA catalysts | Impregnation | O₂ | 20 | 348–438 °C | XRD, BET, H₂-TPR, NH₃-TPD, XPS, XRF, DRIFTS | 195 |
| Fe–FER catalysts | impregnation | NO/O₂/H₂O | 350 | 200–900 °C | XRD, BET, SEM, UV-vis-NIR, FTIR, Mössbauer spectroscopy | 196 |
| Fe zeolite catalysts | Diffusion impregnation | He | 20 | — | UV-Vis-NIR, FTIR, Mössbauer spectroscopy | 197 |
| Zeolite 5A, 13X and ZSM-5 catalysts | Wet impregnation | N₂ | 300 | 298–358 K | N₂O-TPD, BET, isosteric heat of adsorption | 198 |
| Cu/SSZ-13 catalysts | Hydrothermal | NO/NH₃/CO₂/H₂O/NO₂/N₂O | 800–1500 | 200–600 °C | XRD, BET, ICP-OES, UV-vis-DRS, H₂-TPR, HRTEM | 199 |
| Fe/BEA | Ion exchange | N₂ | 300 | 350–380 °C | XRF | 200 |
| Fe–MOR and Fe–FER | Hydrothermal | O₂/He | 100 | 0–350 °C | FTIR, UV-vis | 201 |
| Fe–FER | Hydrothermal | — | — | 500–900 °C | XRD, SEM, FTIR | 202 |
| Zeolite-based Fe catalysts | Ion exchange | NO/O₂/H₂O/He | 350 | 400–800 °C | XRD, FTIR, TPD | 203 |
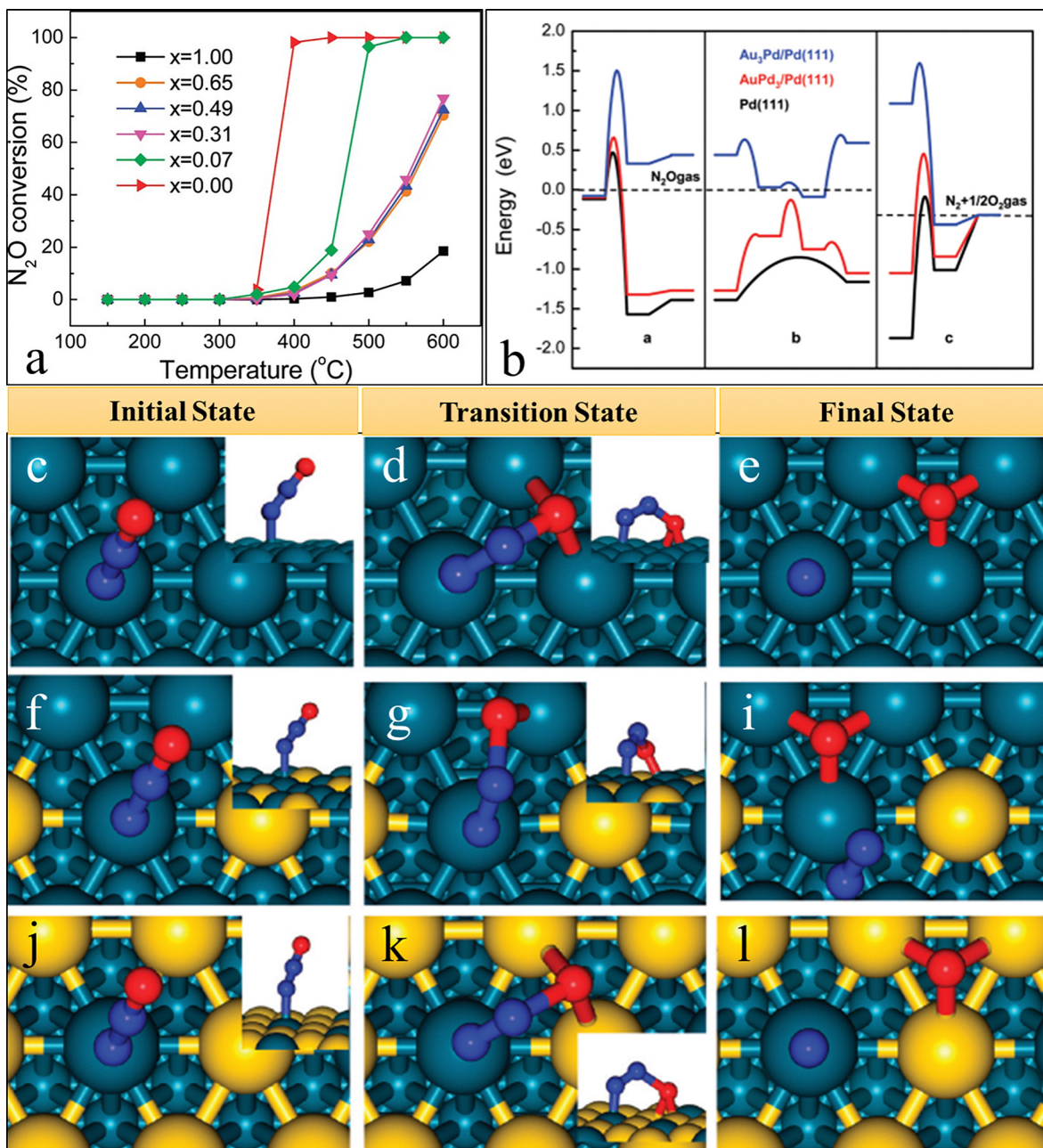
Fig. 12   (a) $N_2O$ conversion (%) as a function of reaction temperature onto $Au_xPd_{1-x}$/SBA-15 catalysts (where $x$ = atomic ratio of Au to total metal atoms; metal loading = 2 wt%). (b) Energy profiles for $N_2O$ decomposition on Pd, $AuPd_3$ and $Au_3Pd$ catalysts. (c)–(k) Mechanism of $N_2O$ degradation into $N_2$ and $O_2$ over (c)–(e) Pd, (f)–(h) $Pd_3Au$/Pd and (i)–(k) $PdAu_3$/Pd catalysts.[209] Reproduced with permission from the American Chemical Society (Copyright©2012).

shorter diffusion length and easier mass/heat transport.[209,216] Recently, the decomposition of $N_2O$ supported by metal-doped nanotubes (NTs), nanosheets (NSs) and nanocages (NCs)-has emerged. Researchers have predicted the roles of metal-confined titania nanotubes,[217,218]

carbon nanotubes (CNTs),[219,220] boron nitride nanotubes, nanosheets,[221,222] and nanocages[223] for $N_2O$ decomposition by employing DFT studies.

Metal-doped nanocages are currently among very popular materials that can capture greenhouse gases and protect the

environment from their harmful effects. Gao *et al.* have successfully doped four Ca atoms in a $C_{60}$ molecule and examined its energy profile for $CO_2$ capture and $N_2O$ adsorption. In comparison, the adsorption of $N_2O$ on pristine $C_{60}$ molecules was very weak as compared with Ca-decorated fullerene $C_{60}$.[224] Fig. 13a represents the doping of Ca atoms in a $C_{60}$ molecule, while Fig. 13b and c show the adsorption of one and two $N_2O$ molecules on the surface of $CaC_{60}$, respectively. Table 8 demonstrates the examples of metal-doped nanotubes, nanosheets and nanocages utilized for $N_2O$ mitigation studies.

**Table 7** Overview of synthesis methods, reaction conditions and various techniques employed during the course of analysis of mesoporous silica-supported metal/metal oxide catalysts for N₂O decomposition

| Catalysts | Method | Reaction atmosphere | Air speed (mL min⁻¹) | N₂O decomposition temp-range (°C K⁻¹) | Techniques used for characterization and activity of catalysts | Ref. |
|---|---|---|---|---|---|---|
| $Al_2O_3$ + $SiO_2$ | Wet impregnation | $N_2$ | 100 | 300–450 °C | AAS, XRD, TPR-$H_2$, FTIR, Raman, XPS, SEM, $N_2$ adsorption | 210 |
| Pt, Pd, Rh/$Al_2O_3$–$SiO_2$ | Hydrothermal | He | 100 | 600–900 °C | XRD, $N_2$ physiosorption and FESEM | 211 |
| Pt/$SiO_2$ | Impregnation | Ar | 10 | 350–600 °C | BET, XRD, ICP | 212 |
| Cu-supported on hollow silica–alumina composite | Impregnation | $N_2$ | 50 | 450–800 K | EDX, UV-Vis-DRS, SEM, TEM | 213 |
| Rh@S-1 | Hydrothermal | — | — | 200–400 °C | STEM, XPS, DRIFTS, TEM | 214 |
| NiCoAl-based monolithic catalysts | Wet impregnation | $N_2$ | 10 | 300–600 °C | SEM, EDX, BET | 215 |
| $TiO_2$@$Fe_2O_3$@$Al_2O_3$ monolith catalysts | Co-precipitation | — | — | 220–420 °C | XRD, XPS | 100 |

*5.3.1.1. Shortcomings of metal-doped nanotubes, nanosheets and nanocages.* Controlled synthesis of metal-confined nanotubes remains a big issue. They face challenges like structural instability at high temperatures, metal agglomeration and limited long-term durability under reaction conditions. Their synthesis can be complex and costly and scalability remains a barrier. In low-temperature zones, these catalysts suffer from serious disadvantages at the industrial level.[251]

*5.3.1.2. Application scenario: power plant emissions.* Metal-doped nanostructures offer exceptional surface area, abundant active sites, and tunable electronic properties, making them highly promising for N₂O decomposition in power plant emissions. They provide excellent dispersion of doped metals and improved redox performance. However, challenges include complex synthesis, potential agglomeration, limited large-scale stability, and higher costs compared to conventional catalyst systems.

**5.3.2. Metal-embedded graphene and graphitic nitrides.** Graphene is considered one of the most promising candidates for next-generation electronic materials of this decade.[225,252] Extensive research is carried out on graphene because of its enormous surface-to-volume ratio (*i.e.* large area) for catalytic reactions. However, modified graphene sheets display high catalytic performance for N₂O decomposition, and several DFT studies have been conducted on this catalytic behaviour, *e.g.* transition metal-embedded graphene,[253–255] N-doped graphene,[256,257] Si-doped graphene,[245,258] metal oxide-doped graphene,[255] and metal-decorated graphene oxides.[253,259] Among them, transition metal-embedded graphene structures possess good thermal stabilities and stronger bonds between metals and neighbouring C-atoms.

Like graphene, graphitic carbon nitride (g-$C_3N_4$) is composed of carbon and nitrogen atoms arranged in a 2D, hexagonal lattice. However, in g-$C_3N_4$, carbon and nitrogen atoms are bonded together in a polymeric, layered structural form. This polymeric arrangement gives it a unique set of properties compared to graphene. However, graphene is a zero-bandgap material while g-$C_3N_4$ is a semiconductor with moderate bandgap that makes it suitable for electronics and photocatalytic applications especially under visible light. Furthermore, its properties can be tuned by modifying its structure, composition and doping that optimize its performance for specific applications.[260–262] For example, Troppovà *et al.* modified its structure by making its nanocomposites with TiO₂ at different weight ratios. The primary focus of the study was to assess the photocatalytic activity of these TiO₂/g-$C_3N_4$ nanocomposites. They investigated the decomposition of N₂O under UV treatment with a wavelength ($\lambda$) of 365 nm. The results indicated that all the synthesized nanocomposites exhibited higher photocatalytic activity than the individual parent materials (g-$C_3N_4$ and TiO₂).[263] The enhanced photocatalytic activity of TiO₂/g-$C_3N_4$ nanocomposites was attributed to the coupling of TiO₂ with g-$C_3N_4$. This coupling was found to improve the separation of electron–hole pairs and expand the range of spectral light absorption. Similarly, N-doped graphene embedded with single transition metal atoms produces single-atom catalysts (SACs), and enable the conversion of CH₄ into
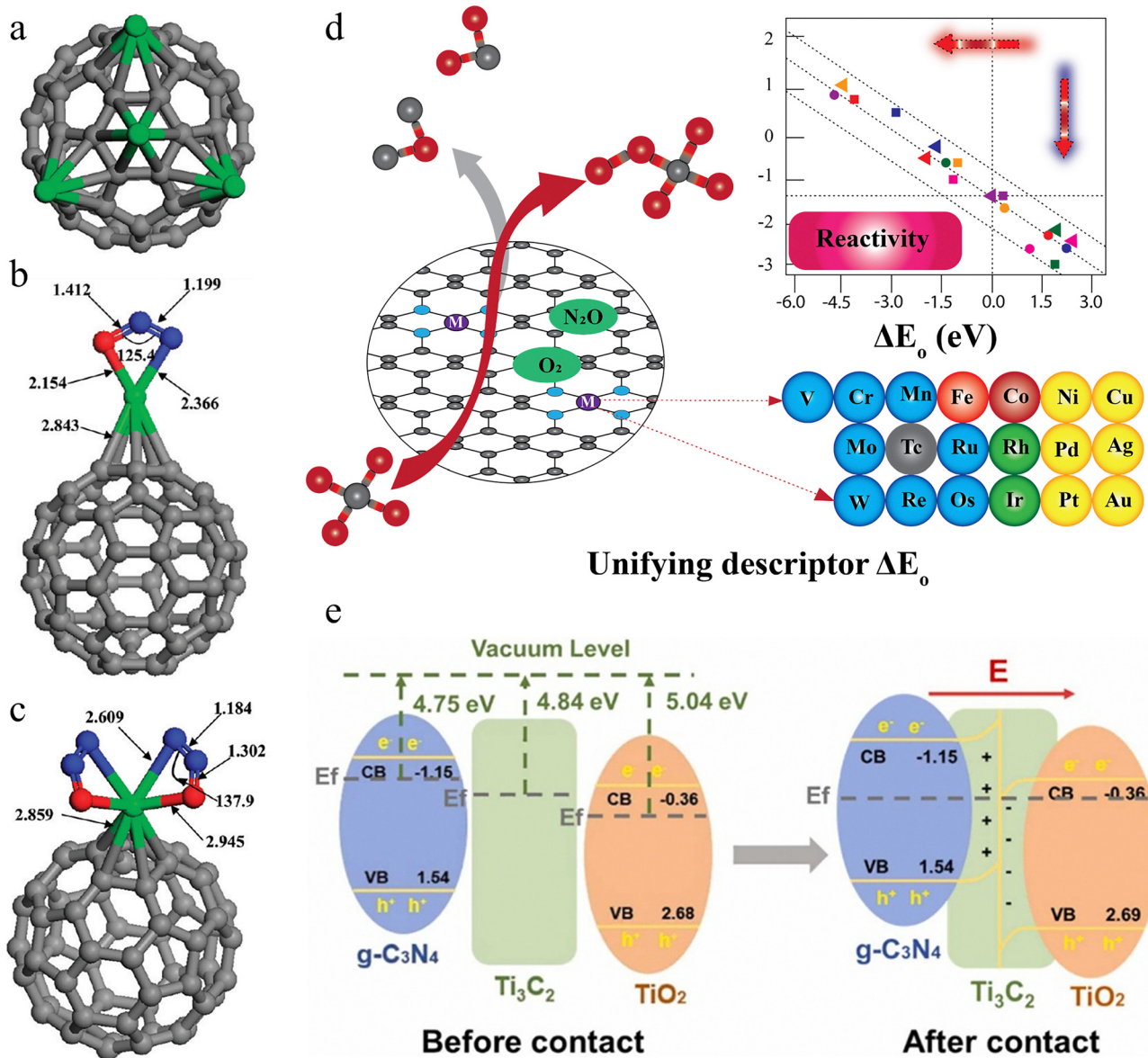
**Fig. 13** (a) Four Ca atoms doped $C_{60}$ nanocage; adsorption profiles and corresponding energies of (b) one and (c) two $N_2O$ molecules on fullerene $(CaC_{60})$.[225] Reproduced with permission from the American Chemical Society (Copyright©2011); (d) mechanism of methane-to-methanol conversion by transition-metal-atom-embedded N-doped graphene (TM–$N_4$/C) catalysts with $N_2O$ and $O_2$ oxidants and a comparison of their reactivity.[226] Reproduced with permission from the American Chemical Society (Copyright©2023). (e) Energy bands of $TiO_2$/MXene/g-$C_3N_4$ displaying energy bending.[227] Reproduced with permission form Elsevier (Copyright©2023).

$CH_3OH$ with the help of $N_2O$ and $O_2$ oxidants (Fig. 13d). The relationship between the adsorption energy of oxygen molecules $(\Delta E_{Ads})$ and the catalytic reactivity in the conversion of methane to methanol can be seen in the inset.[264] Many other examples of use of such catalysts in $N_2O$ abatement are provided in Table 9.

*5.3.2.1. Shortcomings of metal-embedded graphene and graphitic oxides/nitrides.* Major disadvantages associated with these types of catalysts are their low surface area and a rapid recombination between photoexcited electrons and holes. However, this problem is overcome by impregnation or doping of a noble metal or co-catalyst into these semiconductor materials.[226,280]

*5.3.2.2. Application scenario: industrial flue gas treatment.* Metal-embedded graphene and graphitic oxides/nitrides provide high conductivity, large surface area, and strong metal-support interactions, enhancing $N_2O$ decomposition in industrial flue gas treatment. They enable efficient electron transfer and dispersion of active sites. However, their disadvantages include high synthesis costs, sensitivity to oxidation at elevated temperatures, and scalability issues for long-term industrial deployment.

**5.3.3. MXene-based materials.** MXene-based catalysts have emerged as promising materials for $N_2O$ decomposition due to their unique 2D structure, high electrical conductivity and

**Table 8** Overview of synthesis methods, reaction conditions and various techniques employed during the course of analysis of metal-doped nanotubes, nanosheets and nanocages for $N_2O$ decomposition

| Catalysts | Method | Reaction atmosphere | Air speed (mL min$^{-1}$) | $N_2O$ decomposition temp-range (°C K$^{-1}$) | Techniques used for characterization and activity of catalysts | Ref. |
|---|---|---|---|---|---|---|
| Metal oxide-confined interweaved $TiO_2$ nanotubes M/TNT (M = Mn, Cu, Ce, Fe, V, Cr and Co) | Wet impregnation | — | — | 100–300 °C | BET, HRTEM, XRD, XPS, $H_2$-TPR, $NH_3$–TPD | 228 |
| C-doped BN nanotubes (C-BNNTs) | Adsorption | — | — | — | DFT calculations for $N_2O$ adsorption and reduction reaction | 229 |
| C-doped BN nanosheets | Adsorption | — | — | — | DFT calculations, computational calculations | 222 |
| Si-doped $C_3N$ (Si–$C_3N$) nanosheets | Adsorption | — | — | — | First-principle (DFT) calculations | 230 |
| Fullerene-like boron nitride nanocages (C-doped $B_{12}N_{12}$) | Adsorption | — | — | — | DFT calculation of adsorption behaviors of $N_2O$ and CO | 231 |
| Boron-doped $C_3N$ monolayers | Adsorption | — | — | — | DFT | 232 |
| $A_{0.5}Co_{2.5}O_4$ (A = Mg, Ca, Sr, Ba) | Hydrothermal | $O_2/N_2$ | 80 | — | DFT | 233 |
| Fe-embedded $C_2N$ monolayer | — | — | — | — | DFT | 234 |
| SACs supported on defective boron nitride nanotubes (BNNT) | — | — | — | — | DFT | 235 |
| Potassium promoted $Gd_{0.06}Co$ catalysts | Co-precipitation | Ar | 50 | 150–500 °C | XPS, $H_2$-TPR, $O_2$–TPD, XRD, SEM, TEM | 236 |
| Gd to $Co_3O_4$ | Co-precipitation | $N_2$ | 350 | — | DFT | 237 |
| Ni–Co mixed oxides ($Ni_xCo_{1-x}Co_2O_4$) | — | — | — | 250–600 °C | SEM, EDX, XRD, | 238 |
| $CuO$–$Co_3O_4$ | Co-precipitation | $NH_3/O_2/He$ | 100 | 400–700 °C | XAFS, DRIFTS, DFT, XANES | 239 |
| Si (Si-doped haeck-BNNT) | Adsorption | $O_2$ | 550 | — | DFT | 240 |
| MgO(100) in $SO_2$ and CO | Adsorption | — | — | — | DFT | 241 |
| Rh(0.2)/NC–MnFe | Adsorption | $H_2$ | 60 | 100–150 °C | XRD | 242 |
| $MC_{23}$ clusters (M = Ru, Mn, V, Rh, and Pd) clusters | — | — | — | — | DFT | 243 |
| Al- or P-doped hexagonal boron nitride nanosheets (h-BNNS) | Adsorption | — | — | — | DFT | 244 |
| Si@BN-yne | — | — | — | — | DFT, PDOS | 245 |
| Co-doped Fe–Mn@CNTs | Co-precipitation | — | — | 170–250 °C | XRD, XPS | 246 |
| $Sm_{0.06}Ni$ | Adsorption | Ar | 50 | 100–600 °C | SEM, TEM, XRD, XPS, HRTEM | 247 |
| $Co_3O_4$@$CoMn_2O_4$ | Hydrothermal | $NH_3/O_2/SO_2/H_2O/Ar$ | 300 | 90–270 °C | SEM, TEM, HRTEM, XPS, DRIFTS | 248 |
| $M_{13}$@$Cu_{42}$ (M = Cu, Co, Ni, Zn, Ru, Rh, Pd, Pt) core-shell clusters | Adsorption | — | — | — | DFT | 249 |
| Si@$C_{24}N_{24}$ | — | — | — | — | DFT | 250 |

**Table 9** Overview of synthesis methods, reaction conditions and various techniques employed during the course of analysis of metal-embedded graphene, graphitic oxides and nitrides for $N_2O$ decomposition

| Catalysts | Method | Reaction atmosphere | Air speed (mL min$^{-1}$) | $N_2O$ decomposition temp-range (°C K$^{-1}$) | Techniques used for characterization and activity of catalysts | Ref. |
|---|---|---|---|---|---|---|
| BC$_m$N$_n$-doped graphene sheets | Adsorption | — | — | — | DFT calculations, Computational studies on adsorption configurations, electronic structures, and catalytic activity by quantum chemical calculations | 257 |
| Single Si or P atom incorporated N-doped graphene(SiN$_4$-Gr/PN$_4$-Gr) | — | — | — | — | Comparative DFT study, computational calculations for adsorption energies and reduction mechanism by first-principle | 265 |
| Single Ge or Ga atom-doped graphene | Adsorption | — | — | — | DFT study, computational estimation of adsorption energies and reaction mechanisms | 266 |
| ZnO-doped graphene [ZnO(001)@G] | — | — | — | — | DFT calculation for adsorption and activation energies, *ab initio* model, OAT, ER and LH pathway | 267 |
| Al- and Ti-doped graphene (Al-/Ti-graphene) | — | — | — | — | DFT calculations for reaction barriers and thermodynamic parameters | 268 |
| M-decorated graphene oxide (M = Mg, Cu or Ag) | Adsorption | — | — | — | DFT computational method | 259 |
| Graphitic carbon nitride (g-C$_3$N$_4$) | Melamine condensation | N$_2$ | 15 | 400–700 °C | UV-Vis-DRS, PL, FTIR, Raman, SSA, XRD, SEM, TEM | 269 |
| TiO$_2$/g-C$_3$N$_4$ photocatalysts | Adsorption | N$_2$ | 30 | — | XRPD, UV-Vis-DRS, Raman, FTIR, SEM, TEM, BET, PL, XPS, GC-BID | 270 |
| TiO$_2$/g-C$_3$N$_4$ photocatalysts | Hydrothermal | O$_2$ | 3.5–4.5 | — | N$_2$-physisorption, XRD, UV-Vis-DRS, FTIR, Raman, PL, TEM, XPS | 263 |
| g-C$_3$N$_4$/WO$_3$ photocatalysts | Calcination | — | — | — | XRD, XPS, HR–TEM, STEM, N$_2$-adsorption, UV-Vis-DRS, PL, EDS | 271 |
| g-C$_3$N$_4$/ZnO nanocomposite photocatalysts | Co-precipitation | — | — | — | XRD, UV-Vis, FTIR, Raman Spectroscopy, TEM and AAS | 272 |
| g-C$_3$N$_4$/BiVO$_4$ composite photocatalysts | Sol–gel | N$_2$ | 500 | — | XRD, N$_2$-physisorption, UV-Vis-DRS, PL, FTIR, XPS, TEM | 273 |
| BiVO$_4$/g-C$_3$N$_4$ (1 : 1) composite photocatalysts | Adsorption | — | — | — | XPS, UV-Vis-DRS, PL, FTIR, Raman, BET, TEM | 274 |
| g-C$_3$N$_4$ and BiOIO$_3$ | Hydrothermal | — | — | 300–800 °C | FTIR, XRPD, XPS, HRTEM, DRS, TEM | 275 |
| SiN$_4$G | — | — | — | — | DFT | 276 |
| Cu-Embedded Graphene | Adsorption | — | — | — | DFT | 253 |
| Si@Graphene | Adsorption | — | — | 100–350 °C | DFT | 258 |
| Au/C$_2$N and Cu/C$_2$N | Adsorption | — | — | — | DFT | 277 |
| Si-doped C$_3$N (Si–C$_3$N) nanosheets | Co-adsorption | — | — | — | DFT | 278 |
| Co$_3$O$_4$/g-CN | Wet impregnation | N$_2$ | 5 | 100–700 °C | XRD, HR-TEM, N$_2$-physisorption, Raman, FT-IR, XPS, H$_2$-TPR, CO$_2$-TPD, EC | 279 |

**Table 10** Overview of synthesis methods, reaction conditions and various techniques employed during the course of analysis of MXene-based catalysts for $N_2O$ decomposition

| Catalysts | Method | Reaction atmosphere | Air speed (mL min$^{-1}$) | $N_2O$ decomposition temp-range (°C K$^{-1}$) | Techniques used for characterization and activity of catalysts | Ref. |
|---|---|---|---|---|---|---|
| $UO_2$@MXnene (e.g. $Ti_2CO_2$, $V_2CO_2$, $Cr_2CO_2$, $Zr_2CO_2$, $Nb_2CO_2$, $Mo_2CO_2$) | — | — | — | — | ab initio calculations | 283 |
| Y-doped $Ti_2CO_2$ (MXene) monolayer | — | — | — | — | DFT and ab initio calculations | 284 |
| P@$Cr_2CO_2$ and P@$MoCO_2$ | — | — | — | — | DFT | 285 |
| g-$C_3N_4$/$TiO_2$/$Ti_3C_2$ MXene | Air oxidation and ultrasonic processing | $O_2$ | 3000 | — | XRD, SEM, TEM, HRTEM, EDS, XPS, PL, BET, EPR | 286 |
| $TiO_2$–N–$Ti_3C_2T_x$ | Co-precipitation | — | — | — | TEM, SEM, FTIR, Raman, XPS, PL, EPR | 287 |
| (Ti,C)-BiOBr/$Ti_3C_2T_x$ | Solvothermal | $N_2$ | 200 | — | XRD, FESEM, STEM, DRS, XPS, BET, Raman | 288 |
| $Ti_3C_2$–OH with $TiO_2$ | Co-precipitation | $N_2$ | — | — | SEM, TEM, XRD, XPS | 289 |
| Cu/$Ti_3C_2O_2$-$V_0$ and Ni/$Ti_3C_2O_2$–$Ti_1$ | — | — | — | — | DFT | 290 |

tunable surface chemistry. Doping transition metals (e.g. Fe, Co, and Cu) into MXenes enhances redox activity and introduces abundant active sites for $N_2O$ adsorption and activation. Their layered morphology facilitates gas diffusion and charge transfer, which are critical for catalytic efficiency. However, stability under high-temperature and oxidative conditions remains a concern. Additionally, scalable synthesis and control over metal dispersion require further development. Despite these challenges, MXene-based catalysts offer a novel platform for designing efficient and selective $N_2O$ abatement systems.[281]

As of now, there are very limited experimental studies reporting the use of MXene-based catalysts for $N_2O$ abatement. However, a few studies have been conducted for their $N_2O$ decomposition efficiency by mixing MXenes with other semiconductor photocatalysts. For example, Zhao et al. prepared triphase heterostructures via the self-assembly of titania, MXene and graphitic carbon nitride ($TiO_2$/MXene/g-$C_3N_4$) that showed an improved photocatalytic efficiency for NO removal. Z-scheme heterojunctions enhance photocatalysis by preserving strong redox carriers and minimizing recombination of low-activity electrons and holes, as shown in Fig. 13e.[282] Other studies on photocatalytic decomposition of $NO_x$ using MXenes coupled with other materials are listed in Table 10.

### 5.4. Porous MOFs and MOF-derived catalysts

MOFs act as porous solid material catalysts possessing coordinatively unsaturated sites (CUS) for gas adsorption, separation and catalysis.[291] Their well-defined composition, hollow structures, small particle size, and exposed surface impart considerable efficiency and stability to these catalysts. MOFs are also utilized as precursors for the synthesis of metal oxides that can prevent the nanoparticle's clustering during the calcination.[227]

Metal–organic frameworks are composed of metal atoms or metal oxide clusters coordinated to organic linkers. This arrangement creates a highly ordered, porous network with a large surface area. The choice of metal and linkers can be tailored to achieve specific applications. MOFs are well known for their structural flexibility, meaning that their frameworks can be tuned or modified to suit particular needs. This flexibility allows for the design of customized surface and porous

structures. Coordinative unsaturated metal sites are of particular interest, as these sites have metal atoms with unoccupied coordination, making them highly reactive. CUS can be crucial in gas adsorption and separation processes as well as catalytic reactions, which is why MOFs are excellent candidates for gas adsorption and separation due to their high surface area and tunable porosity. The tunable nature of MOFs generate catalytic sites with precise geometries, enhancing the catalytic efficiency and selectivity.[292,293] For example, nanoscale MOFs may exhibit different properties compared to their bulk counterparts, making them suitable for their specific dynamic applications.[294,295]

Despite the huge number of reports on gas sorption, the $N_2O$ abatement studies by MOFs are still scarce. The common route of $N_2O$ abatement is through catalytic decomposition, but adsorptive removal of $N_2O$ by MOFs has also been reported in cases when catalytic decomposition is not economically feasible due to very low $N_2O$ concentrations.[156] In some studies, MOFs also offer an important means for dissociative adsorption of $N_2O$,[296–300] as displayed in Fig. 14.
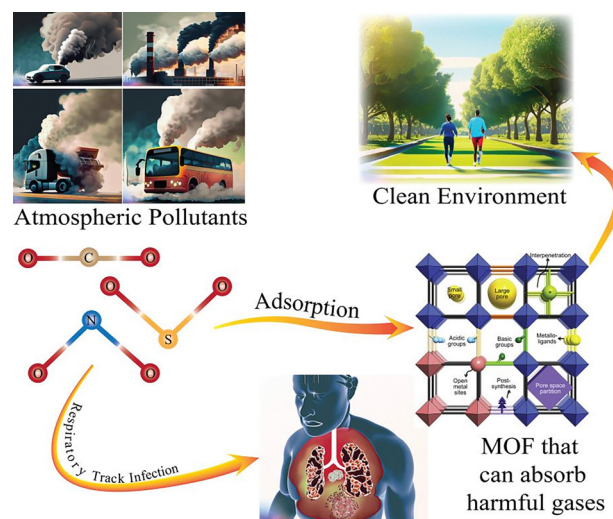


**Fig. 14** Layout of the removal of atmospheric pollutants (that affect respiratory tract) via adsorption through MOFs.

**Table 11** Overview of synthesis methods, reaction conditions and various techniques employed during the course of analysis of MOFs and MOF–derived catalysts for $N_2O$ decomposition

| Catalysts | Method | Reaction atmosphere | Air speed (mL min$^{-1}$) | $N_2O$ decomposition temp-range (°C K$^{-1}$) | Techniques used for characterization and activity of catalysts | Ref. |
|---|---|---|---|---|---|---|
| $M_3(BTC)_2$ MOF [M = Cr, Fe, Co, Ni, Cu and Zn] | Wet impregnation | — | — | — | DFT calculations with M06-L functional, EXAFS, computational screening | 302 |
| MOF-derived Ni/CeO$_2$ HPOC | Wet impregnation | Ar | 10 | 250–500 °C | SEM, TEM, N$_2$-adsorption, EDS, XRD, H$_2$-TPR, Raman, XPS, ICP–MS, GC–TCD | 297 |
| Fe-supported MOF Zr-NU-1000 | Wet impregnation | — | — | — | DFT and CASPT2 calculations with M06-L functional | 303 |
| MnO$_2$ decorated Ru-MOF (Ru-NH$_2$-UiO-66/MnO$_2$) | Hydrothermal | — | — | Not clear | XRD, XPS, BET, SEM, TEM, N$_2$O–TPD, MS, EXAFS, IC, DFT | 304 |
| MFU-4l MOFs (MFU-4l, Cu$^I$-MFU-4l and Li-MFU-4l) (BTDD$^{2-}$ ligands and [Zn$_5$Cl$_4$]$^{6+}$ building units) | Wet impregnation | N$_2$ | 3 | Not clear | DFT calculations, PXRD, FTIR, TGA, ICP–OES, BET | 305 |
| Fe(II)(Me$_3$TACN)(S$_2$SiMe$_2$) | Hydrothermal | — | — | 100–135 °C | UV-vis, resonance Raman, EPR, Mössbauer, XAS, DFT | 306 |
| ZIF-67 derived Co/CoO$_x$@C | Hydrothermal | N$_2$ | 30 | 305–650 °C | TPD, DRIFTS | 307 |
| Mn@Cu$_3$(BTC)$_2$ | Ion exchange | — | — | 230–260 °C | SEM, TEM, XRD, XPS, FESEM, ZEISS-ΣIGMA HD, BET | 308 |

Vogiatzis *et al.* conducted a computational study on high-spin Fe(IV)–OXO complexes that have well-known activating effects on the strong C–H bonds.[301] Although it is difficult to stabilize a high-spin electronic configuration for homogeneous catalysis in molecular species, the results suggested that it is attainable in MOF-based catalysts, *e.g.* Fe$_2$(dobdc) and its Mg-substituted analogues. Using a screening approach, different frameworks were identified that could form Fe(IV)–OXO complexes on N$_2$O adsorption. It was concluded from the study that among different materials, Fe–BTT selectively oxidizes C$_2$H$_6$ to C$_2$H$_5$OH by N$_2$O adsorption. The follow-up spectroscopic techniques suggested that the observed reactivity was attributed to the existing defect sites.[301] Further examples from the recent studies are given in Table 11.

**5.4.1. Shortcomings of MOFs and MOF-derived catalysts.** MOFs and MOF-derived catalysts face challenges such as limited thermal stability, structural degradation under reaction conditions, and low conductivity, which can hinder electron transfer during N$_2$O decomposition. Additionally, their synthesis can be complex and costly and active site accessibility may be restricted, affecting the overall catalytic efficiency.

**5.4.2. Application scenario: waste gas purification.** MOFs and MOF-derived catalysts offer ultra-high surface area, tunable porosity, and flexible metal-ligand coordination, making them

highly effective for N$_2$O decomposition in waste gas purification. Their derived metal oxides or carbons show strong redox activity and stability. However, drawbacks include complex synthesis, limited hydrothermal and thermal stability and challenges in scaling up for industrial applications.

## 5.5. Emerging or novel materials

Antenna-reactor catalysts and quantum dot-based catalysts exhibit unique light-harvesting and charge separation abilities, crucial for N$_2$O decomposition. Further details are provided in the coming sections.

**5.5.1. Antenna-reactor catalysts.** Very recently, the concept of "Antenna–Reactor" plasmonic photocatalysts is introduced, and it is rapidly gaining interest in the field of catalysis. In a few studies conducted to date, N$_2$O decomposition was selected as a model reaction.[138,309] The use of antenna-reactor photocatalysts holds special significance in controlling the rate and products of various chemical reactions. Being poor absorbers of light, many traditional catalysts lack the ability to catalyze efficiently because of the restricted surface chemistry. By combining a catalytic nanoparticle with a plasmonic nanoantenna in a single complex, the light-harvesting properties of plasmonic nanoparticles can be fine-tuned to increase light absorption.[310] Table 12 summarizes few examples of these catalysts.

**Table 12** Overview of synthesis methods, reaction conditions and various techniques employed during the course of analysis of antenna-reactor catalysts for $N_2O$ decomposition

| Catalysts | Method | Reaction atmosphere | Air speed (mL min$^{-1}$) | $N_2O$ decomposition temp-range (°C K$^{-1}$) | Techniques used for characterization and activity of catalysts | Ref. |
|---|---|---|---|---|---|---|
| Al–Ir antenna–reactor photocatalysts | Ion exchange | — | — | 250–350 °C | HAADF–STEM, MS, XPS and UV-Vis-NIR | 138 |
| Antenna-reactor plasmonic photocatalysts (Pd decorated Al NCs, Al@Cu$_2$O and Cu–Ru surface alloy@Cu) | Co-precipitation | — | — | — | XPS, ICP–MS, UV-Vis-DRS, TEM, HAADF GC-MS, HR–TEM | 309 |

**5.5.2. Quantum dots.** Quantum dots (QDs) can play a significant role in $N_2O$ decomposition due to their tunable bandgaps, high surface-to-volume ratios, and excellent light absorption properties. These features enable efficient electron–hole pair generation and separation under visible light, promoting redox reactions. QDs can be engineered to provide active sites for $N_2O$ adsorption and activation, potentially lowering the activation energy and enhancing catalytic efficiency under mild, sustainable reaction conditions.[311] Currently, there are no experimental studies specifically reporting the use of QDs for $N_2O$ decomposition. However, theoretical investigations have predicted their potential.

# 6. Performance-based summary of $N_2O$ decomposition catalysts

Performance-based comparisons are critical for identifying optimal catalysts and guiding their future research directions. Table 13 provides a comparative summary of the benchmark performance metrics for different classes of catalysts used in $N_2O$ decomposition, based on their catalytic activity, temperature range, hydrothermal stability, and resistance to inhibitors. This provides a clear performance-based comparison of $N_2O$ decomposition catalysts.

# 7. Mechanisms of $N_2O$ decomposition

There are five primary mechanisms of $N_2O$ decomposition in the context of fundamental steps and catalyst surface interactions. These mechanisms are key to understanding how various
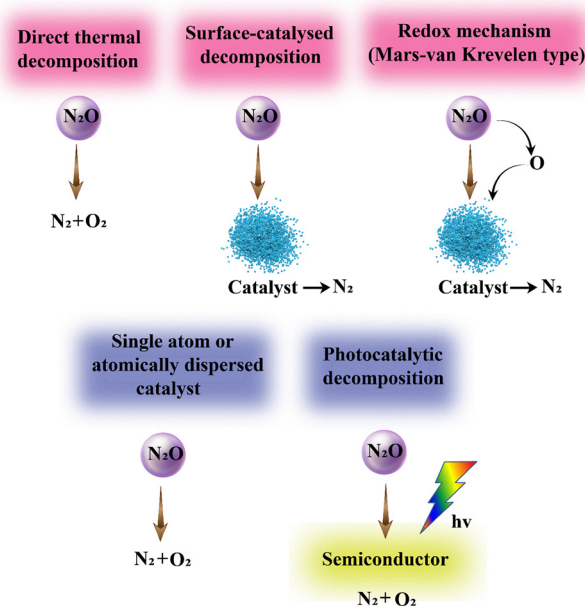


**Fig. 15** Different mechanisms of $N_2O$ decomposition.

catalysts function in breaking down $N_2O$ into harmless components (Fig. 15).

## 7.1. Direct thermal decomposition $N_2O \rightarrow N_2 + \frac{1}{2}O_2$

Direct thermal decomposition of nitrous oxide occurs at temperatures above 800 °C in the absence of catalysts. Although the reaction is thermodynamically favourable, the extreme energy demand makes this route impractical for most industrial applications. However, in certain specialized high-concentration

**Table 13** Comparison of the benchmark performances of $N_2O$ decomposition catalysts

| Catalyst class | Typical active sites | $T_{50}{}^a$ (°C) | Hydrothermal stability | Resistance to $H_2O/O_2{}^b$ | Remarks |
|---|---|---|---|---|---|
| Metal oxides | $CuO$, $Co_3O_4$, $MnO_2$ | 300–500 | Moderate | Low moderate | Inexpensive; deactivated by moisture |
| Spinel oxides | $CoFe_2O_4$, $MnFe_2O_4$ | 300–450 | High | Moderate | Good stability; better than simple oxides |
| Hydroxyapatites | $Ca_{10}(PO_4)_6(OH)_2$ doped with Fe, Cu | >450 | Moderate | Poor | High thermal stability; lower activity |
| Mixed metal oxides | Cu–Mn, Fe–Al oxides | 250–400 | Moderate | Low – moderate | Synergistic effects; still limited by deactivation |
| Hydrotalcites | Mg–Al–Fe–Cu layered structures | 300–500 | Moderate | Moderate | Tunable; activity depends on calcination |
| Zeolites | Fe, Co, Cu in ZSM-5, SSZ-13 | 200–400 | High | High | Fe–SSZ-13 shows best performance under wet/oxidizing conditions |
| Mixed metal oxides in mesoporous silica | Fe/Cu in SBA-15, MCM-41 | 250–450 | Moderate – high | Moderate | Good dispersion and surface area |
| Metal-doped nanotubes/ nanosheets | Fe, Co, Cu on CNTs, g-$C_3N_4$, BN | 300–500 | Moderate | Low – moderate | High surface are; expensive synthesis |
| Graphene and graphitic nitrides | Single atoms or clusters (Fe, Co) | 250–450 | Low – moderate | Low – moderate | Tunable electronic structure; prone to sintering |
| MXene-based materials | $Ti_3C_2$, $Mo_2TiC_2$ doped with metals | 250–400 | Moderate | Moderate | Emerging materials with potential for hybrid photocatalysis |
| MOFs and MOF-derived catalysts | Fe-MIL-100, ZIF-8-derived oxides | 300–500 | Low – moderate | Poor | High porosity; often thermally unstable |
| Antenna-reactor catalysts | Dual-site systems (*e.g.* Ce, Fe) | 200–350 | Moderate | Moderate – high | Emerging concept; synergistic enhancement |
| Quantum dots-based catalysts | CdS, $Fe_3O_4$ QDs supported on hosts | <300 (predicted) | Unknown | Unknown | Theoretical potential; lacks direct experimental validation |

$^a$ $T_{50}$ (°C): temperature at which 50% $N_2O$ conversion is achieved. $^b$ Resistance to $H_2O/O_2$: resistance to inhibition by water vapour or oxygen.

processes such as semiconductor manufacturing, direct pyrolysis of $N_2O$ has been investigated under nitrogen-rich atmospheres at temperatures approaching 1000 °C. These studies demonstrate that while $N_2O$ can indeed be decomposed under such conditions, the process requires significant thermal input and careful gas-phase control, which limits its scalability for broader emission abatement. Nonetheless, this pathway remains relevant in niche applications where high-purity nitrogen or oxygen streams are simultaneously desired.[312]

### 7.2. Surface-catalysed decomposition

Most practical catalysts (*e.g.* Fe-, Co- and Cu-based) accelerate this reaction by activating $N_2O$ on their surfaces. It requires active oxygen-vacancy sites. Catalysts can be used to lower the activation energy for N–O bond cleavage. Overall, it is summarized in three steps:[313,314]

  1. Adsorption

$$N_2O_{(g)} \rightarrow N_2O_{(ads)}$$

  2. N–O bond cleavage

$$N_2O \rightarrow N_{2(g)} + O_{(ads)}$$
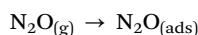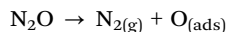
  3. Recombination of surface oxygen

$$O_{(ads)} + O_{(ads)} \rightarrow O_{2(g)}$$

### 7.3. Redox mechanism (Mars–van Krevelen type)

It is commonly observed in transition metal oxide catalysts. Here, the catalyst surface is first reduced and then deoxidized, enabling a catalytic cycle:[315,316]

  1. In the first step, $N_2O$ reacts with a lattice oxygen.

$$N_2O + [M]-O \rightarrow N_2 + [M]-O-O$$
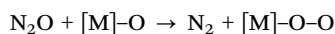
  2. Oxygen vacancy is replenished by $O_2$ from the gas phase.

$$[M] + \tfrac{1}{2}O_2 \rightarrow [M]-O$$
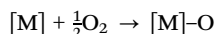
### 7.4. Single atom or atomically dispersed catalysis

This type of catalysis is common in Fe–ZSM-5, Fe–SSZ-13 and Cu-CHA materials. During this catalysis, first $N_2O$ coordinates to a single metal centre. Then, the N–O bond is cleaved through electron transfer from the metal. Oxygen binds to the metal site or adjacent framework oxygen. It shows high site selectivity and stability, especially in the presence of steam or $O_2$.

### 7.5. Photocatalytic decomposition

It involves photon-excitation of catalysts such as $TiO_2$, g-$C_3N_4$ or MXene hybrids. In this case, light generates electron–hole pairs in the photocatalysts. Electrons are responsible for the reduction of $N_2O$ to $N_2$. The holes may oxidize adsorbed species or water to maintain charge neutrality. This mechanism is still under development particularly for low-temperature $N_2O$ removal.

# 8. N₂O activation mechanisms

$N_2O$ activation mechanisms follow different pathways, three of which are most common, namely dual-pathway mechanism, radical-initiated oxidative decomposition and electron-assisted surface decomposition. Representative reactions belonging to each category are indicated in this section.
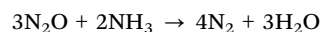
### 8.1. Dual-pathway mechanism

It corresponds to the classical surface-mediated activation of $H_2O$ on catalytic active sites (*), described as follows:

$$N_2O + * \rightarrow N_2 + *O^-$$

$$2*O^- \rightarrow O_2 + 2*$$

$$N_2O + *O^- \rightarrow N_2 + O_2 + *$$
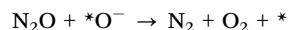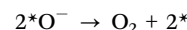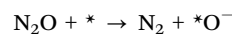
When $NH_3$ is present ($NH_3$-assisted SCR), surface $O_2$ can be removed as follows:

$$2NH_3 + 3*O^- \rightarrow N_2 + 3H_2O + 3*$$
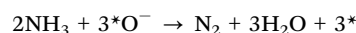
Interaction of $NH_3$ with $N_2O$ is given as

$$3N_2O + 2NH_3 \rightarrow 4N_2 + 3H_2O$$

The Fe–MOR catalyst was employed for the systematic investigation of $N_2O$ reduction reaction mechanism by $NH_3$, through which the roles of different oxygen species were examined[317] (Fig. 16a).
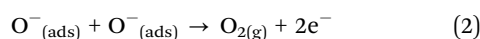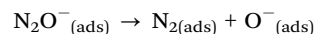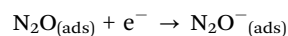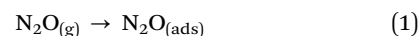
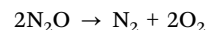### 8.2. Radical-mediated oxidation of N₂O

In this case, $N_2O$ activation occurs *via* the following main reaction routes (Fig. 16b):

$$N_2O \rightarrow NO + N$$

$$NO + O \rightarrow NO_2$$

$$NO + OH \rightarrow HNO_2$$

$$NO_2 + OH \rightarrow HNO_3$$
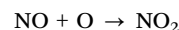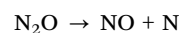
### 8.3. Electron-mediated reduction of N₂O

The solid solution system is fairly active toward the decomposition reaction of $N_2O$ in the temperature range of 300–450 °C. Winter proposed the mechanism of $N_2O$ decomposition reaction involving the following steps[318] (Fig. 16c):

$$2N_2O \rightarrow N_2 + 2O_2$$

$$N_2O_{(g)} \rightarrow N_2O_{(ads)} \tag{1}$$

$$N_2O_{(ads)} + e^- \rightarrow N_2O^-{}_{(ads)}$$

$$N_2O^-{}_{(ads)} \rightarrow N_{2(ads)} + O^-{}_{(ads)}$$

$$O^-{}_{(ads)} + O^-{}_{(ads)} \rightarrow O_{2(g)} + 2e^- \tag{2}$$
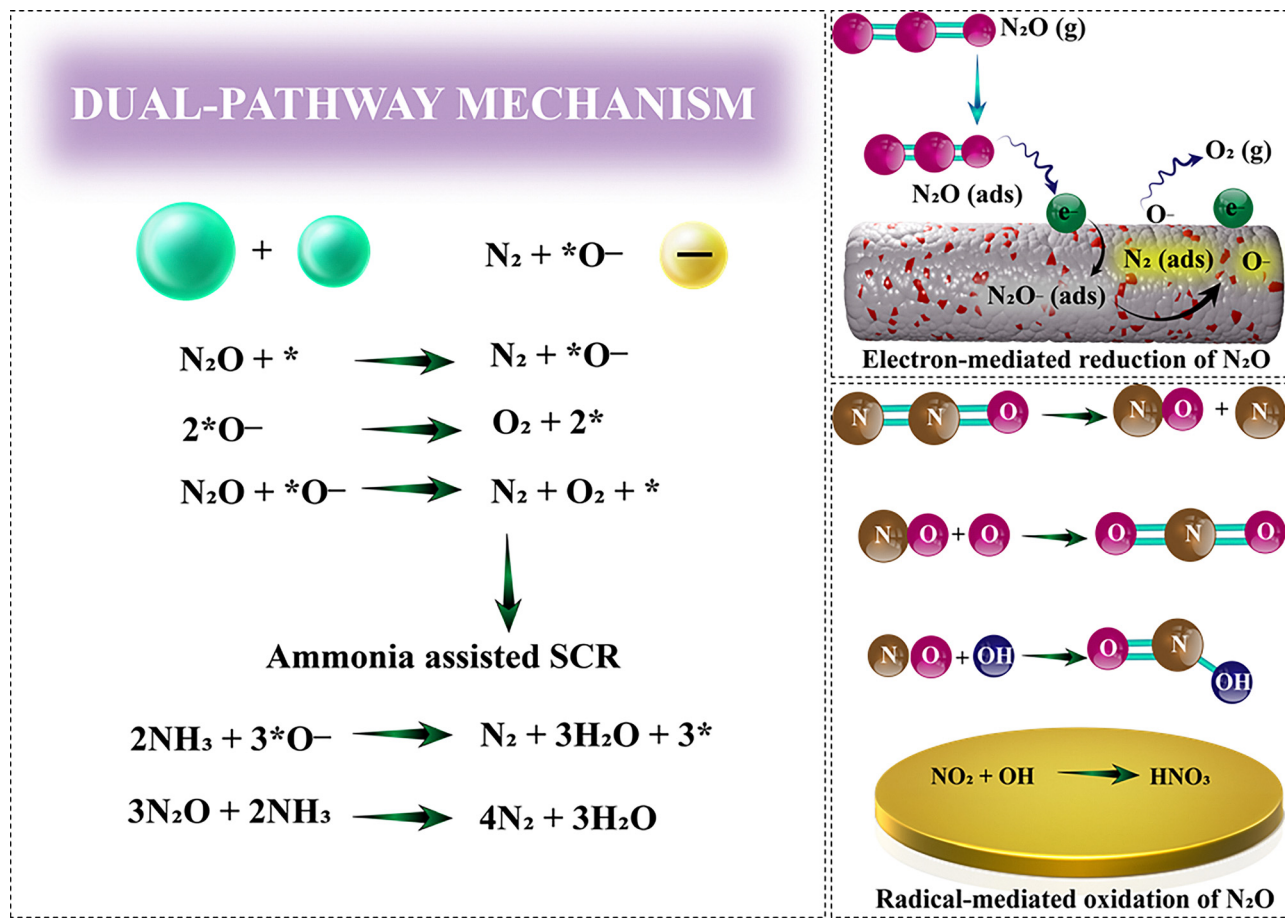
**Fig. 16** Different mechanisms of $N_2O$ activation.

$$O^- + N_2O \rightarrow O_{2(g)} + N_{2(g)} + 2e^-$$
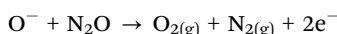
In governing the reaction rate, $N_2O$ adsorption [step 1] and oxygen ($O_{ads}^-$) desorption as $O_2$ [step 2] are the key steps. Using the following rate equations, the kinetic parameters of $N_2O$ decomposition have been derived:[319]

$$\ln\left(\frac{a}{a-x}\right) = k_1 t$$

$$\left(\frac{1}{2}a\right)\ln\left(\frac{a^{1/2} + x^{1/2}}{a^{1/2} + x^{1/2}}\right) - (2x)^{1/2} = k_2 t$$

$$\ln\left(\frac{a}{a-x}\right) - b\left[\left(\frac{1}{2}a\right)\ln\left(\frac{a^{1/2} + x^{1/2}}{a^{1/2} + x^{1/2}}\right) - (2x)^{1/2}\right] = k_t 3$$

(3)

Here, $\alpha = P^{\circ} N_2O$ (*i.e.* initial pressure of $N_2O$), $x = P^t N_2O$ (which represents the pressure of $N_2O$ at time '$t$'), and $x/2 = P^t O_2$ (*i.e.* pressure of oxygen released at any time '$t$').

This rate equation corresponds to the non-inhibitory effect caused by $O_2$. The rate eqn (3) corresponds to strong inhibition by $O_2$ and represents weak inhibition of the decomposition kinetics by $O_2$.[320]

# 9. Conclusions and future perspectives

In this review, we summarized various categories of $N_2O$ decomposition catalysts. Starting with the well-known category of TMI-exchanged zeolites, we then presented other different classes including hydrotalcites, spinel oxides, mixed metal oxides, mesoporous silica-supported metal oxides and pure metal oxides, and finally, the more recent categories of catalysts such as metal-doped nanotubes, nanosheets and nanocages, graphene and graphitic oxides/nitrides, MOFs and MOF-derived catalysts for adsorptive reduction of $N_2O$. Nitrous oxide ($N_2O$) is a potent greenhouse gas and a major contributor to stratospheric ozone depletion. Its anthropogenic and natural emissions through biological processes such as nitrification, denitrification and nitrifier denitrification along with abiotic pathways and industrial activities demand urgent and effective mitigation strategies. Catalytic decomposition of $N_2O$ into benign products ($N_2$ and $O_2$) stands out as a promising solution owing to its direct applicability in emission abatement technologies and potential integration into existing industrial setups.

This review comprehensively categorizes $N_2O$ decomposition catalysts based on their mechanisms, compositions and material structures, providing a unified understanding of their

functionality and efficiency. Mechanistically, the catalysts are classified into those following direct catalytic decomposition (DCD), selective catalytic reduction (SCR) and other redox or surface-catalysed processes. Composition-wise, both precious metal-based catalysts (*e.g.* Rh, Pt, and Pd) and non-precious alternatives (*e.g.* Fe, Co, and Cu-based materials) have been investigated with emphasis on cost, stability and activity trade-offs. The type of support materials – ranging from metal oxides, spinels to mesoporous and layered structures – plays a vital role in modulating dispersion, redox behaviour and oxygen vacancy dynamics.

Importantly, this review offers a progress-based classification, moving from classical oxide-based catalysts to novel nanostructured materials and framework materials such as MOFs and MOF-derived catalysts, which have shown significant promise due to their high surface areas, tunable porosity and ability to accommodate multiple active sites. Emerging materials such as antenna-reactor systems and quantum dots illustrate the frontier of $N_2O$ decomposition research, hinting at the exciting potential of photonic and nanoscale control over activation energies.

Mechanistic pathways such as surface-catalysed decomposition, Mars–van Krevelen mechanisms, and single-atom catalysis reveal the intricate nature of $N_2O$ activation, where lattice oxygen, metal oxidation states and coordination environments dictate the reaction rate and selectivity. Novel mechanisms including photo-catalytic and electron/radical-mediated pathways further expand the toolkit available for $N_2O$ conversion, particularly under mild conditions or light-driven environments.

Looking ahead, several key future perspectives emerge. First, the rational design of catalysts with high activity at low temperatures coupled with selectivity and durability under industrial gas compositions remains an urgent priority. The integration of computational modelling and machine learning can accelerate the discovery of optimal catalyst compositions and structures. Second, a shift towards earth-abundant, non-toxic elements is essential to scale these technologies sustainably. Single-atom catalysts and dual-function catalysts that combine decomposition with selective oxidation or reduction reactions open new frontiers in multifunctional reactor design.

Moreover, *in situ* and *operando* characterization techniques should be leveraged to elucidate real-time reaction mechanisms, bridging the gap between theoretical models and actual catalyst performance. Finally, interdisciplinary collaboration between catalysis, materials science, environmental engineering and process design is essential to translate laboratory successes into commercially viable solutions.

In summary, catalytic $N_2O$ decomposition is a vibrant and evolving field. Continued research on catalyst development, mechanistic understanding and scalable application will be pivotal in mitigating $N_2O$ emissions and achieving global climate and sustainability goals.

# Conflicts of interest

Authors declare no competing financials interest.

# Abbreviations

| | |
|---|---|
| WHO | World Health Organization |
| EPA | Environmental Protection Agency |
| IPPC | Intergovernmental Panel on Climate Change |
| AFED | Arab Forum for Environment and Development |
| APAN | Asian Pacific Adaptation Network |
| CCCCC | Caribbean Community Climate Change Centre |
| CAN | Climate Action Network |
| CCL | Citizen Climate Lobby |
| CJA | Climate Justice Alliance |
| EDF | Environmental Defense Fund |
| HEA | Health and Environmental Alliance |
| NRDC | Natural Resources Defense Council |
| GWP | Global warming potential |
| AOB | Ammonia-oxidizing bacteria |
| AOA | Ammonia-oxidizing archaea |
| DCD | Direct catalytic decomposition |
| SCR | Selective catalytic reduction |
| ZSM | Zeolite Socony Mobil |
| SSZ | Aluminosilicate zeolite |
| MOF | Metal–organic framework |
| $E_a$ | Activation energy |
| CFBC | Circulating fluidized bed combustion |
| SNCR | Selective non-catalytic reduction |
| EG | Ethylene glycol |
| DP | Deposition precipitation |
| IMP | Impregnation method |
| DP–Cl | Deposition precipitation by chloride precursor |
| PTA | Phosphotungstic acid |
| SACs | Single-atom catalysts |
| DFT | Density functional theory |
| GC | Gas chromatography |
| XRD | X-ray diffraction |
| XPS | X-ray photoelectron spectroscopy |
| FTIR | Fourier transform infrared spectroscopy |
| TEM | Transmission electron microscopy |
| HRTEM | High-resolution transmission electron microscopy |
| TPR | Temperature-programmed reduction |
| $H_2$–TPR | Temperature-programmed reduction with $H_2$ |
| XPS | X-ray photoelectron spectroscopy |
| EXAFS | Extended X-ray absorption fine structure |
| EDS | Energy-dispersive spectroscopy |
| STEM | Scanning transmission electron spectroscopy |
| EELS | Electron energy loss spectroscopy |
| $O_2$–TPR | Temperature-programmed reduction with $O_2$ |
| nHAP | Natural hydroxyapatites |
| SSA | Specific surface area |
| HADDF | High-angle annular dark field |
| $O_2$-TPD | Temperature-programmed desorption of chemisorbed $O_2$ |
| XRF | X-ray fluorescence |
| TPSR | Temperature-programmed surface reaction |

| SEM | Scanning electron microscopy |
| FESEM | Field emission scanning electron microscopy |
| SAED | Selected area electron diffraction |
| TPCR | Transfer-PCR |
| QMS | Quadrupole mass spectrometer |
| EPR | Electron paramagnetic resonance |
| TGA | Thermogravimetric analysis |
| ICP–OES | Inductively coupled plasma-optical emission spectrometry |
| BET | Brunauer, Emmett and Teller theory |
| MS | Mass spectrometry |
| GC–TCD | Gas chromatograph equipped with a thermal conductivity detector |
| DTA | Differential thermal analysis |
| XRPD | X-ray powder diffraction |
| QDs | Quantum dots |
| DRS | Diffuse reflectance spectroscopy |
| DRIFTS | Diffuse reflectance infrared Fourier transform spectroscopy |
| CO-DRIFTS | Diffuse reflectance infrared Fourier transform spectroscopy of CO adsorption |
| MCT | Mercury cadmium telluride |
| LDHs | Layered double hydroxides |
| MP | Mirror plane |
| PILC | Pillared clay |
| VOCs | Volatile organic compounds |
| LS | Low saturation |
| SP | Sequential precipitation |
| TMIs | Transition metal ions |
| IEC | Ion exchange capacity |
| WEI | Wet ion exchange |
| XANES | X-ray absorption near-edge structure |
| CHA | Chabazite |
| AAS | Atomic absorption spectroscopy |
| ICP–AES | Inductive coupled plasma atomic emission spectroscopy |
| FID | Flame ionization detector |
| ESR | Electron spin resonance |
| NMR | Nuclear magnetic resonance |
| SBA | Santa Barbara Amorphous |
| NTs | Nanotubes |
| NSs | Nanosheets |
| NCs | Nanocages |
| CNTs | Carbon nanotubes |
| TNTs | Titania nanotubes |
| PL | Photoluminescence |
| CUS | Coordinatively unsaturated sites |
| BDC | 1,4-Benzenedicarboxylate |
| BTC | 1,3,5-Benzenetricarboxylate |
| MCM | Mobil Composition of Matter |
| KIT | Korea Advanced Institute of Science and Technology |
| MCF | Mesoporous Cellular Foam |
| Fe-FER | Iron Ferrierite |
| TG–DTA–MS | Thermogravimetric differential thermal analysis mass spectrometry |

## Data availability

The data and necessary protocols of this study have been included as part of the SI.

## Acknowledgements

## References

1  F. Charlson, S. Ali, T. Benmarhnia, M. Pearl, A. Massazza, J. Augustinavicius and J. G. Scott, *Int. J. Environ. Res. Public Health*, 2021, **18**, 4486.

2  S. Sinhababu, Y. Lakliang and N. P. Mankad, *Dalton Trans.*, 2022, **51**, 6129–6147.

3  K. Hayashi and N. Itsubo, *Int. J. Life Cycle Assess.*, 2023, 1–13.

4  N. J. Bassous, A. C. Rodriguez, C. I. L. Leal, H. Y. Jung, C. K. Lee, S. Joo, S. Kim, C. Yun, M. G. Hahm and M. H. Ahn, *Adv. Sens. Res.*, 2023, 2300094.

5  R. Feng and X. Fang, *Environ. Sci. Technol.*, 2022, **56**, 5299–5301.

6  S. He, Y. Han and X. Qin, *J. Environ. Sci.*, 2025, **157**, 615–632.

7  B. K. Sovacool, S. Griffiths, J. Kim and M. Bazilian, *Renewable Sustainable Energy Rev.*, 2021, **141**, 110759.

8  X. Zhu, M. Burger, T. A. Doane and W. R. Horwath, *Proc. Natl. Acad. Sci. U. S. A.*, 2013, **110**, 6328–6333.

9  N. Wrage, G. L. Velthof, M. L. Van Beusichem and O. Oenema, *Soil Biol. Biochem.*, 2001, **33**, 1723–1732.

10 T. C. Robinson, D. E. Latta, L. Notini, K. E. Schilling and M. M. Scherer, *Environ. Sci.: Processes Impacts*, 2021, **23**, 1531–1541.

11 U. Deka, I. Lezcano-Gonzalez, B. M. Weckhuysen and A. M. Beale, *ACS Catal.*, 2013, **3**, 413–427.

12 Y. Zhang, G. Cao and X. Yang, *Energy Fuels*, 2021, **35**, 6443–6464.

13 Y. Liu, F. Gao, H. Yi, C. Yang, R. Zhang, Y. Zhou and X. Tang, *Environ. Sci. Pollut. Res.*, 2021, **28**, 2549–2571.

14 H. Chen, L. Zeng, D. Wang, Y. Zhou and X. Yang, *Water Res.*, 2020, **184**, 116168.

15 M. Galle, D. Agar and O. Watzenberger, *Chem. Eng. Sci.*, 2001, **56**, 1587–1595.

16 A. E. Hughes, N. Haque, S. A. Northey and S. Giddey, *Resources*, 2021, **10**, 93.

17 Q. Zhang, S. Gao and J. Yu, *Chem. Rev.*, 2022, **123**, 6039–6106.

18 N. Richards, J. H. Carter, E. Nowicka, L. A. Parker, S. Pattisson, Q. He, N. F. Dummer, S. Golunski and G. J. Hutchings, *Appl. Catal., B*, 2020, **264**, 118501.

19 S. Hinokuma, T. Iwasa, Y. Kon, T. Taketsugu and K. Sato, *Catal. Commun.*, 2021, **149**, 106208.

20 S. Hinokuma, T. Iwasa, Y. Kon, T. Taketsugu and K. Sato, *Sci. Rep.*, 2020, **10**, 21605.

21 M. Miao, M. Zhang, H. Kong, T. Zhou, X. Yang and H. Yang, *Energies*, 2021, **14**, 6148.

22 Y. Yin, R. Xiao, L. Qiu, C. Wang and H. Chang, *Fuel*, 2024, **366**, 131303.

23 Y. Li, S. Yang, H. Peng, W. Liu, Y. Mi, Z. Wang, C. Tang, D. Wu and T. An, *J. Catal.*, 2021, **395**, 195–209.

24 R. Li, Y. Li and Z. Liu, *Fuel*, 2024, **355**, 129405.

25 N. Richards, J. H. Carter, L. A. Parker, S. Pattisson, D. G. Hewes, D. J. Morgan, T. E. Davies, N. F. Dummer, S. Golunski and G. J. Hutchings, *ACS Catal.*, 2020, **10**, 5430–5442.

26 A. Szymaszek-Wawryca, P. Summa, D. Duraczyńska, U. Díaz and M. Motak, *Materials*, 2022, **15**, 7884.

27 F. Lin, T. Andana, Y. Wu, J. Szanyi, Y. Wang and F. Gao, *J. Catal.*, 2021, **401**, 70–80.

28 F. Saleem, M. Z. Abid, K. Rafiq, A. Rauf, K. Ahmad, S. Iqbal, R. Jin and E. Hussain, *Int. J. Hydrogen Energy*, 2024, **52**, 305–319.

29 N. Wajid, K. Rafiq, M. Z. Abid, A. Ilyas, T. Najam, A. Rauf and E. Hussain, *Mater. Chem. Phys.*, 2023, **306**, 128062.

30 M. Sabir, K. Rafiq, M. Z. Abid, U. Quyyum, S. S. A. Shah, M. Faizan, A. Rauf, S. Iqbal and E. Hussain, *Fuel*, 2023, **353**, 129196.

31 T. Gaidei, A. Kokorin, N. Pillet, M. Srukova, E. Khaustova, G. Shmurak and N. Yaroshenko, *Russ. J. Phys. Chem. A*, 2007, **81**, 895–900.

32 L. Han, S. Cai, M. Gao, J.-Y. Hasegawa, P. Wang, J. Zhang, L. Shi and D. Zhang, *Chem. Rev.*, 2019, **119**, 10916–10976.

33 D. Shun, D. H. Bae, J. Y. Paek and Y. S. Park, *Korean J. Chem. Eng.*, 2004, **21**, 890–894.

34 A. Ilyas, K. Rafiq, M. Z. Abid, A. Rauf and E. Hussain, *RSC Adv.*, 2023, **13**, 2379–2391.

35 M. Z. Abid, A. Ilyas, K. Rafiq, A. Rauf, M. A. Nadeem, A. Waseem and E. Hussain, *Environ. Sci.: Water Res. Technol.*, 2023, **9**, 2238–2252.

36 M. Z. Abid, K. Rafiq, A. Rauf, S. S. A. Shah, R. Jin and E. Hussain, *Nanoscale Adv.*, 2023, **5**, 3247–3259.

37 J. Liu, L. Wang, W. Song, M. Zhao, J. Liu, H. Wang, Z. Zhao, C. Xu and Z. Duan, *ACS Sustainable Chem. Eng.*, 2018, **7**, 2811–2820.

38 L.-L. Zhang, X.-M. Chen and C.-G. Liu, *Inorg. Chem.*, 2019, **58**, 5221–5229.

39 V. G. Komvokis, M. Marti, A. Delimitis, I. A. Vasalos and K. S. Triantafyllidis, *Appl. Catal., B*, 2011, **103**, 62–71.

40 P. S. S. Reddya, N. S. Babua, N. Lingaiaha, P. S. Prasada and I. Raob, *Proc. Eur. Cong. Chem. Eng.*, 2007, 1–12.

41 S. N. Basahel, M. Mokhtar, T. T. Ali and K. Narasimharao, *Catal. Today*, 2020, **348**, 166–176.

42 N. Zhang, C. He, Y. Jing, Y. Qian, T. Toyao and K.-I. Shimizu, *Surf. Interfaces*, 2024, **46**, 104120.

43 M. K. Singh and G. Rajaraman, *Inorg. Chem.*, 2019, **58**, 3175–3188.

44 M. G. Galloni, S. Campisi, A. Gervasini, S. Morandi and M. Manzoli, *Appl. Catal., A*, 2023, **655**, 119101.

45 X. Hu, L. Wu, S. Ju, C. Dong, Y. Yang and W. Qin, *Environ. Eng. Sci.*, 2014, **31**, 308–316.

46 X. Li, J. Chen, C. Lu, G. Luo and H. Yao, *Fuel*, 2021, **299**, 120910.

47 M. D. Esrafili, H. Janebi and P. Mousavian, *Appl. Surf. Sci.*, 2021, **569**, 151001.

48 H. Yu, X. Qi, X. Du, Y. Pan, X. Feng, W. Shan and Y. Xiong, *Mol. Catal.*, 2023, **537**, 112960.

49 E. M. Goliaei and N. Seriani, *Appl. Surf. Sci.*, 2022, **579**, 152215.

50 K. Feng, R. Lin, T. Chen, Y. Hu, Y. Feng, D. Chen, M. H. Tahir and T. Cao, *J. Environ. Chem. Eng.*, 2024, 111891.

51 H. Liu, S. Yang, G. Wang, H. Liu, Y. Peng, C. Sun, J. Li and J. Chen, *Environ. Sci. Technol.*, 2022, **56**, 16325–16335.

52 H. Liu, J. Chen, Y. Wang, S. Xiong, Z. Su, Y. Wang, W. Yang, X. Chu, W. Yang and Y. Peng, *Chem. Eng. J.*, 2021, **414**, 128643.

53 X. Hu, Y. Wang, R. Wu and Y. Zhao, *Mol. Catal.*, 2021, **509**, 111656.

54 W. Gao, D. Wen, J. Ho and Y. Qu, *Mater. Today Chem.*, 2019, **12**, 266–281.

55 F. Zasada, J. Gryboś, E. Budiyanto, J. Janas and Z. Sojka, *J. Catal.*, 2019, **371**, 224–235.

56 Q. Zhao, Z. Yan, C. Chen and J. Chen, *Chem. Rev.*, 2017, **117**, 10121–10211.

57 G. Chen, C. Guyon, Z. Zhang, B. Da Silva, P. Da Costa, S. Ognier, D. Bonn and M. Tatoulian, *Microfluid. Nanofluid.*, 2014, **16**, 141–148.

58 Q. Shen, L. Li, J. Li, H. Tian and Z. Hao, *J. Hazard. Mater.*, 2009, **163**, 1332–1337.

59 M.-J. Kim, S.-J. Lee, I.-S. Ryu, M.-W. Jeon, S.-H. Moon, H.-S. Roh and S. G. Jeon, *Mol. Catal.*, 2017, **442**, 202–207.

60 Y. Li, A. Sundermann, O. Gerlach, K.-B. Low, C. C. Zhang, X. Zheng, H. Zhu and S. Axnanda, *Catal. Today*, 2019, **355**, 608–619.

61 J. Pérez-Ramírez, F. Kapteijn, G. Mul and J. A. Moulijn, *J. Catal.*, 2002, **208**, 211–223.

62 X. Wei, Y. Wang, X. Li, R. Wu and Y. Zhao, *Mol. Catal.*, 2020, **491**, 111005.

63 L. Rocha-Meneses, A. Inayat, M. Ayoub, S. Ullah, S. R. Naqvi, S. Farrukh, A. Mustafa, A. Z. Abdullah and A. H. Bhat, *Environ. Prog. Sustainable Energy*, 2023, **42**, e13982.

64 S. Wojcik, P. Indyka, Z. Sojka and A. Kotarba, *Catal. Today*, 2020, **348**, 111–117.

65 G. Grzybek, P. Stelmachowski, S. Gudyka, J. Duch, K. Ćmil, A. Kotarba and Z. Sojka, *Appl. Catal., B*, 2015, **168–169**, 509–514.

66 M. Inger, J. Rajewski, M. Ruszak and M. Wilk, *Chem. Papers*, 2019, **73**, 1979–1986.

67 B. M. Abu-Zied, S. A. Soliman and S. E. Abdellah, *J. Ind. Eng. Chem.*, 2015, **21**, 814–821.

68 S. Li, J. Zhao, Z. Song, H. Wang, T. Zhang, J. Liu and Q. Jiang, *Fuel*, 2024, **362**, 130745.

69 A. Inayat, L. Rocha-Meneses, M. Ayoub, S. Ullah, A. Z. Abdullah, S. R. Naqvi and A. H. Bhat, *Environ. Sci. Pollut. Res.*, 2023, 1–12.

70 T. Franken and R. Palkovits, *Appl. Catal., B*, 2015, **176–177**, 298–305.

71 A. Klyushina, K. Pacultová, K. Karásková, K. Jirátová, M. Ritz, D. Fridrichová, A. Volodarskaja and L. Obalová, *J. Mol. Catal. A: Chem.*, 2016, **425**, 237–247.

72 H. Yu, X. Wang, X. Wu and Y. Chen, *Chem. Eng. J.*, 2018, **334**, 800–806.

73 M. Tursun, X. Wang, F. Zhang and H. Yu, *Catal. Commun.*, 2015, **65**, 1–5.

74 S. Wójcik, G. Grzybek, P. Stelmachowski, Z. Sojka and A. Kotarba, *Catalysts*, 2020, **10**, 41.

75 M. Inger, B. Moszowski, M. Ruszak, J. Rajewski and M. Wilk, *Catalysts*, 2020, **10**, 987.

76 P. Hermawan, J. Kim, M. H. Jeong, S. A. Choi, S.-M. Hwang and S. K. Jeong, *Chemosphere*, 2024, **367**, 143642.

77 A. Klegova, K. Pacultová, T. Kiška, P. Peikertová, A. Rokicińska, P. Kuśtrowski and L. Obalová, *Mol. Catal.*, 2022, **533**, 112754.

78 B. Abu-Zied, S. Soliman and S. Abdellah, *Curr. Catal.*, 2020, **9**, 152–162.

79 B. Li, X. Duan, T. Zhao, B. Niu, G. Li, Z. Zhao, Z. Yang, D. Liu, F. Zhang and J. Cheng, *Environ. Sci. Technol.*, 2024, **58**(4), 2153–2161.

80 P. Lu, L. Ye, X. Yan, X. Chen, P. Fang, D. Chen, D. Chen and C. Cen, *J. Hazard. Mater.*, 2021, **414**, 125468.

81 S. Li, Y. Li, W. Shen, Y. Bai and L. Kong, *J. Cleaner Prod.*, 2022, **380**, 134961.

82 Y. Matsumura and J. B. Moffat, *J. Catal.*, 1994, **148**, 323–333.

83 S. Sugiyama, K. Abe, H. Hayashi and J. B. Moffat, *Appl. Catal., A*, 1999, **183**, 135–142.

84 Y. Cui, H. Liu, Y. Lin and Z. Ma, *J. Taiwan Inst. Chem. Eng.*, 2016, **67**, 254–262.

85 C. Huang, Z. Ma, P. Xie, Y. Yue, W. Hua and Z. Gao, *J. Mol. Catal. A: Chem.*, 2015, **400**, 90–94.

86 M. G. Galloni, S. Campisi, A. Gervasini, S. Morandi and M. Manzoli, *Appl. Catal., A*, 2023, **655**, 119101.

87 X. Tan, H. Chen, L. Shi, Q. Lu, S. Qi, C. Yi and B. Yang, *Catal. Lett.*, 2023, **153**, 3724–3733.

88 Y. Lin, T. Meng and Z. Ma, *J. Ind. Eng. Chem.*, 2015, **28**, 138–146.

89 Y. Wang, X. Zhou, X. Wei, X. Li, R. Wu, X. Hu and Y. Zhao, *Mol. Catal.*, 2021, **501**, 111370.

90 M. G. Galloni, *Development of metal functionalized hydroxyapatite catalysts for air-quality protection*, PhD Thesis, Università degli Studi di Milano, 2022.

91 M. Galloni, S. Campisi and A. Gervasini, *Iron functionalised hydroxyapatites as efficient eco-friendly catalysts for air-quality protection*, 2020.

92 X. Liu, Y. Wang, R. Wu and Y. Zhao, *Catal. Surveys Asia*, 2021, **25**, 168–179.

93 K.-M. Lee, G. Kwon, S. Hwang, J. A. Boscoboinik and T. Kim, *Catal. Sci. Technol.*, 2021, **11**, 7850–7865.

94 D. Jia, K. Hanna, G. Mailhot and M. Brigante, *Molecules*, 2021, **26**, 5748.

95 U. Quyyum, K. Rafiq, M. Z. Abid, F. Ahmad, A. Rauf and E. Hussain, *Environ. Sci.: Water Res. Technol.*, 2023, **9**, 1147–1160.

96 M. Jalil, K. Rafiq, M. Z. Abid, A. Rauf, S. Wang, S. Iqbal and E. Hussain, *Nanoscale Adv.*, 2023, **5**, 3233–3246.

97 K. U. Sahar, K. Rafiq, M. Z. Abid, A. Rauf, U. U. Rehman, M. A. Nadeem, R. Jin and E. Hussain, *Colloids Surf., A*, 2023, **674**, 131942.

98 A. Aslam, M. Z. Abid, K. Rafiq, A. Rauf and E. Hussain, *Sci. Rep.*, 2023, **13**, 6306.

99 H. Beyer, J. Emmerich, K. Chatziapostolou and K. Koehler, *Appl. Catal., A*, 2011, **391**, 411–416.

100 L. Han, M. Gao, J.-Y. Hasegawa, S. Li, Y. Shen, H. Li, L. Shi and D. Zhang, *Environ. Sci. Technol.*, 2019, **53**, 6462–6473.

101 C. Ratanatawanate, A. Chyao and K. J. Balkus Jr, *J. Am. Chem. Soc.*, 2011, **133**, 3492–3497.

102 T. Gaidei, A. Kokorin, N. Pillet, V. Sadov, M. Strukova, S. Filatov, E. Khaustova and N. Yaroshenko, *Russ. J. Appl. Chem.*, 2010, **83**, 1130–1138.

103 S. Imamura, J.-i Tadani, Y. Saito, Y. Okamoto, H. Jindai and C. Kaito, *Appl. Catal., A*, 2000, **201**, 121–127.

104 Y. Li, A. Sundermann, O. Gerlach, K.-B. Low, C. C. Zhang, X. Zheng, H. Zhu and S. Axnanda, *Catal. Today*, 2020, **355**, 608–619.

105 T. C. Peck, G. K. Reddy, M. Jones and C. A. Roberts, *J. Phys. Chem. C*, 2017, **121**, 8435–8443.

106 M. Konsolakis, *ACS Catal.*, 2015, **5**, 6397–6421.

107 Y. Ni, Z. Han, Y. Chai, G. Wu and L. Li, *EES Catal.*, 2023, **1**, 459–494.

108 H. Xu, Y. Ma, J. Chen, W.-X. Zhang and J. Yang, *Chem. Soc. Rev.*, 2022, **51**, 2710–2758.

109 M. Zabilskiy, P. Djinović, E. Tchernychova and A. Pintar, *Appl. Catal., B*, 2016, **197**, 146–158.

110 H. Zhu, Y. Li and X. Zheng, *Appl. Catal., A*, 2019, **571**, 89–95.

111 X. Fan, S. Kang, J. Li and T. Zhu, *RSC Adv.*, 2018, **8**, 26998–27007.

112 H. Zeng and X. Pang, *Appl. Catal., B*, 1997, **13**, 113–122.

113 M. Jabłońska, M. A. Arán, A. M. Beale, K. Góra-Marek, G. Delahay, C. Petitto, K. Pacultová and R. Palkovits, *RSC Adv.*, 2019, **9**, 3979–3986.

114 S. Carabineiro, E. Papista, G. Marnellos, P. Tavares, F. Maldonado-Hódar and M. Konsolakis, *Mol. Catal.*, 2017, **436**, 78–89.

115 M. Lykaki, E. Papista, N. Kaklidis, S. A. Carabineiro and M. Konsolakis, *Catalysts*, 2019, **9**, 233.

116 K. Karásková, K. Pacultová, K. Jirátová, D. Fridrichová, M. Koštejn and L. Obalová, *Catalysts*, 2020, **10**, 1134.

117 X. Hu, Y. Wang, R. Wu, L. Zhao, X. Wei and Y. Zhao, *Appl. Surf. Sci.*, 2020, **514**, 145892.

118 T. Zhao, Y. Li, Q. Gao, Z. Liu and X. Xu, *Catal. Commun.*, 2020, **137**, 105948.

119 P. H. Ho, M. Jabłońska, M. Nocuń, G. Fornasari, F. Ospitali, A. Vaccari, P. Benito and R. Palkovits, *ChemCatChem*, 2019, **11**, 5580–5592.

120 E. M. Iwanek, L. F. Liotta, G. Pantaleo, K. Krawczyk, E. Gdyra, J. Petryk, J. W. Sobczak and Z. Kaszkur, *Catalysts*, 2021, **11**, 325.

121 B. M. Abu-Zied, L. Obalová, K. Pacultová, A. Klegova and A. M. Asiri, *J. Ind. Eng. Chem.*, 2021, **93**, 279–289.

122 E. M. Kostyukhin, A. L. Kustov, N. V. Evdokimenko, A. I. Bazlov and L. M. Kustov, *J. Am. Ceram. Soc.*, 2021, **104**, 492–503.

123 D. Wang, Q. Yao, S. Hui and Y. Niu, *Fuel*, 2019, **251**, 23–29.

124 W. Muhammad, L. Wu, A. El Kasmi, A. Muhammad and Z. Tian, *J. Therm. Sci.*, 2023, **32**, 531–541.

125 Y. Zeng, Z. Wu, L. Guo, Y. Wang, S. Zhang and Q. Zhong, *Mol. Catal.*, 2020, **488**, 110916.

126 Y. Zeng, F. Lyu, Y. Wang, S. Zhang, Q. Zhong and Z. Zhong, *Mol. Catal.*, 2022, **525**, 112356.

127 L. Sheng, Z. Ma, S. Chen, J. Lou, C. Li, S. Li, Z. Zhang, Y. Wang and H. Yang, *Chin. J. Catal.*, 2019, **40**, 1070–1077.

128 Z. Z. Khan, I. A. Khan, I. Khan, M. H. S. Wattoo and A. Badshah, *Solid State Sci.*, 2019, **98**, 106035.

129 D. Wang, Q. Yao, C. Mou, S. Hui and Y. Niu, *Fuel*, 2019, **254**, 115719.

130 F. Zhao, D. Wang, X. Li, Y. Yin, C. Wang, L. Qiu, J. Yu and H. Chang, *Ind. Eng. Chem. Res.*, 2022, **61**, 13854–13862.

131 M.-x Xu, H.-X. Wang, H.-d Ouyang, L. Zhao and Q. Lu, *J. Hazard. Mater.*, 2021, **401**, 123334.

132 M. Zabilskiy, I. Arčon, P. Djinović, E. Tchernychova and A. Pintar, *ChemCatChem*, 2021, **13**, 1814–1823.

133 A. A. Khan, A. Ahmad, H. M. Al-Swaidan, S. Haider, M. S. Akhtar and S. U. Khan, *Mol. Catal.*, 2022, **527**, 112392.

134 C.-G. Liu, Y.-J. Chu, L.-L. Zhang, C. Sun and J.-Y. Shi, *Environ. Sci. Technol.*, 2019, **53**, 12893–12903.

135 M. Wang, W. Li and S. Wang, *J. Phys. Chem. C*, 2023, **127**, 20344–20353.

136 S. Xie, D. Kim, K. Ye, L. Tetard and F. Liu, *J. Rare Earths*, 2023, **41**, 941–951.

137 M. Jabłońska and R. Palkovits, *Catal. Sci. Technol.*, 2016, **6**, 49–72.

138 D. F. Swearer, H. Robatjazi, J. M. P. Martirez, M. Zhang, L. Zhou, E. A. Carter, P. Nordlander and N. J. Halas, *ACS Nano*, 2019, **13**, 8076–8086.

139 D. Tichit and B. Coq, *CATTECH*, 2003, **7**, 206–217.

140 Y. Zhang, X. Wang, Y. Zhu, B. Hou, X. Yang, X. Liu, J. Wang, J. Li and T. Zhang, *J. Phys. Chem. C*, 2014, **118**, 1999–2010.

141 X. Xing, N. Li, J. Cheng, Y. Sun, G. Wang, Z. Zhang, H. Xu, C. He and Z. Hao, *Ind. Eng. Chem. Res.*, 2019, **58**, 9362–9371.

142 F. Gholami, M. Tomas, Z. Gholami and M. Vakili, *Sci. Total Environ.*, 2020, **714**, 136712.

143 A. De Stefanis, M. Dondi, G. Perez and A. Tomlinson, *Chemosphere*, 2000, **41**, 1161–1165.

144 E. E. Kiss, T. J. Vulić and A. F. Reitzmann, *React. Kinet. Catal. Lett.*, 2005, **86**, 233–240.

145 M. C. Karaeyvaz and S. Balci, *Microporous Mesoporous Mater.*, 2021, **323**, 111193.

146 S. Kannan and C. Swamy, *Catal. Today*, 1999, **53**, 725–737.

147 M. Jabłońska, M. A. Arán, A. M. Beale, G. Delahay, C. Petitto, M. Nocuń and R. Palkovits, *Appl. Catal., B*, 2019, **243**, 66–75.

148 Y. Zhang, Y. Guo, N. Li and Y. Feng, *Pol. J. Environ. Stud.*, 2019, **28**, 4477–4484.

149 P. H. Ho, M. Jabłońska, R. Palkovits, E. Rodríguez-Castellón, F. Ospitali, G. Fornasari, A. Vaccari and P. Benito, *Chem. Eng. J.*, 2020, **379**, 122259.

150 S. Xiong, J. Chen, N. Huang, S. Yang, Y. Peng and J. Li, *Environ. Sci. Technol.*, 2019, **53**, 10379–10386.

151 M. Armandi, T. Andana, S. Bensaid, M. Piumetti, B. Bonelli and R. Pirone, *Catal. Today*, 2020, **345**, 59–70.

152 A. Inayat, M. Ayoub, A. Z. Abdullah, S. Ullah and S. R. Naqvi, *Environ. Prog. Sustainable Energy*, 2019, **38**, 13129.

153 D. Lopes, F. Zotin and L. A. Palacio, *Appl. Catal., B*, 2018, **237**, 327–338.

154 J. Akil, C. Ciotonea, S. Siffert, S. Royer, L. Pirault-Roy, R. Cousin and C. Poupin, *Catal. Today*, 2022, **384**, 97–105.

155 C. d O. P. Teixeira, S. da Silva Montani, J. C. S. Soares, L. A. Palacio and F. M. Z. Zotin, *Mol. Catal.*, 2024, **561**, 114157.

156 Z. Zhuang, B. Guan, J. Chen, C. Zheng, J. Zhou, T. Su, Y. Chen, C. Zhu, X. Hu and S. Zhao, *Chem. Eng. J.*, 2024, 150374.

157 Z. Tišler, A. Klegová, E. Svobodová, J. Šafář, K. Strejcová, J. Kohout, S. Šlang, K. Pacultová, D. Rodríguez-Padrón and R. Bulánek, *Catalysts*, 2020, **10**, 1398.

158 G. He, B. Zhang, H. He, X. Chen and Y. Shan, *Sci. Total Environ.*, 2019, **673**, 266–271.

159 L. J. Lobree, I.-C. Hwang, J. A. Reimer and A. T. Bell, *J. Catal.*, 1999, **186**, 242–253.

160 A. Ates, A. Reitzmann, C. Hardacre and H. Yalcin, *Appl. Catal., A*, 2011, **407**, 67–75.

161 M. Rutkowska, A. Jankowska, E. Różycka-Dudek, W. Dubiel, A. Kowalczyk, Z. Piwowarska, S. Llopis, U. Díaz and L. Chmielarz, *Catalysts*, 2020, **10**, 1139.

162 J. Zhang, X. Tang, H. Yi, Q. Yu, Y. Zhang, J. Wei and Y. Yuan, *Appl. Catal., A*, 2022, **630**, 118467.

163 Y. Li and J. N. Armor, *Appl. Catal., B*, 1992, **1**, L21–L29.

164 S. A. Yashnik, O. P. Taran, T. A. Surovtsova, A. B. Ayushev and V. N. Parmon, *J. Environ. Chem. Eng.*, 2022, **10**, 107950.

165 N. F. Biturini, A. P. N. Santos and M. S. Batista, *React. Kinet., Mech. Catal.*, 2019, **126**, 341–352.

166 P. J. Smeets, J. S. Woertink, B. F. Sels, E. I. Solomon and R. A. Schoonheydt, *Inorg. Chem.*, 2010, **49**, 3573–3583.

167 T. Žumbar, I. Arčon, P. Djinović, G. Aquilanti, G. Žerjav, A. Pintar, A. Ristić, G. Dražić, J. Volavšek and G. Mali, *ACS Appl. Mater. Interfaces*, 2023, **15**, 28747–28762.

168 B. Liu, D. Yao, F. Wu, L. Wei, X. Li and X. Wang, *Ind. Eng. Chem. Res.*, 2019, **58**, 20516–20527.

169 S. Yasumura, H. Ide, T. Ueda, Y. Jing, C. Liu, K. Kon, T. Toyao, Z. Maeno and K.-I. Shimizu, *JACS Au*, 2021, **1**, 201–211.

170 X. Zhang, Q. Shen, C. He, C. Ma, J. Cheng, L. Li and Z. Hao, *ACS Catal.*, 2012, **2**, 512–520.

171 M. Jin, P. Wang, L. Zhang, C. Ao and L. Lei, *Therm. Sci. Eng. Prog.*, 2023, **45**, 102088.

172 M. Jabłońska, M. E. Potter and A. M. Beale, *ChemCatChem*, 2024, **16**, e202301214.

173 C. Ruan, X. Wang, C. Wang, L. Zheng, L. Li, J. Lin, X. Liu, F. Li and X. Wang, *Nat. Commun.*, 2022, **13**, 718.

174 W.-S. Ju, M. Matsuoka and M. Anpo, *Catal. Lett.*, 2001, **71**, 91–93.

175 S. Dzwigaj, D. Reja, S. Koné-Guira, A. Miche, G. Costentin and C. Thomas, *Appl. Catal., A*, 2023, **657**, 119119.

176 M. Shukla, B. V. Chauhan, S. Verma and A. Dhar, *Solids*, 2022, **3**, 665–683.

177 B. Bromley, C. Pischetola, L. Nikoshvili, F. Cárdenas-Lizana and L. Kiwi-Minsker, *Molecules*, 2020, **25**, 3867.

178 B. Kang, M. Li, Z. Di, X. Guo, Y. Wei, J. Jia and R. Zhang, *Catal. Today*, 2022, **402**, 17–26.

179 B. Kang, R. Zhang, M. Guo, X. Guo, Z. Di, Y. Wei and J. Jia, *Energy Fuels*, 2023, **37**(23), 18019–18029.

180 D. Pietrogiacomi, M. C. Campa, L. Ardemani and M. Occhiuzzi, *Catal. Today*, 2019, **336**, 131–138.

181 G. A. Zenkovets, R. A. Shutilov, V. I. Sobolev and V. Y. Gavrilov, *Catal. Commun.*, 2020, **144**, 106072.

182 C. Gao, J. Li, J. Zhang and X. Sun, *Catalysts*, 2020, **10**, 646.

183 J. B. Lim, S. H. Cha and S. B. Hong, *Appl. Catal., B*, 2019, **243**, 750–759.

184 K. M. Farhan, A. N. Thabassum, T. M. Ismail and P. Sajith, *Catal. Sci. Technol.*, 2022, **12**, 1466–1475.

185 B. Zhang, G. He, Y. Shan and H. He, *Catal. Today*, 2019, **327**, 177–181.

186 Y. You, S. Chen, J. Li, J. Zeng, H. Chang, L. Ma and J. Li, *J. Hazard. Mater.*, 2020, **383**, 121117.

187 L. M. Kustov, S. F. Dunaev and A. L. Kustov, *Molecules*, 2022, **27**, 398.

188 S. Li, J. Wang, R. Shang, J. Zhao, Q. Xu, H. Wang and J. Liu, *Mol. Catal.*, 2024, **552**, 113706.

189 X. Liang, H. Tang, F. Yang, G. Tu, F. Zhang, Q. Xiao, Y. Zhong and W. Zhu, *Microporous Mesoporous Mater.*, 2019, **290**, 109655.

190 G. Zhao, E. Benhelal, A. Adesina, E. Kennedy and M. Stockenhuber, *J. Phys. Chem. C*, 2019, **123**, 27436–27447.

191 J. Zeng, S. Chen, Z. Fan, C. Wang, H. Chang and J. Li, *Ind. Eng. Chem. Res.*, 2020, **59**, 19500–19509.

192 J. Cheng, D. Zheng, G. Yu, R. Xu, C. Dai, N. Liu, N. Wang and B. Chen, *ACS Catal.*, 2022, **13**, 934–947.

193 T. Zhang, Y. Qiu, G. Liu, J. Chen, Y. Peng, B. Liu and J. Li, *J. Catal.*, 2020, **392**, 322–335.

194 J. Han, A. Wang, G. Isapour, H. Harelind, M. Skoglundh, D. Creaser and L. Olsson, *Ind. Eng. Chem. Res.*, 2021, **60**, 17826–17839.

195 S. Li, C. Zhang, J. Li, Y. Li, H. Wang, C. Li and Y. Song, *Res. Chem. Intermed.*, 2019, **45**, 3601–3616.

196 G. Sádovská, M. Bernauer, B. Bernauer, E. Tabor, A. Vondrová and Z. Sobalík, *Catal. Commun.*, 2018, **112**, 58–62.

197 M. L. Bols, B. E. Snyder, H. M. Rhoda, P. Cnudde, G. Fayad, R. A. Schoonheydt, V. Van Speybroeck, E. I. Solomon and B. F. Sels, *Nat. Catal.*, 2021, **4**, 332–340.

198 T. Wu, Y. Shen, L. Feng, Z. Tang and D. Zhang, *J. Chem. Eng. Data*, 2019, **64**, 3473–3482.

199 A. J. Shih, J. M. González, I. Khurana, L. P. Ramírez, A. Peña, L. A. Kumar and A. L. Villa, *ACS Catal.*, 2021, **11**, 10362–10376.

200 S. J. Lee, I. S. Ryu, S. G. Jeon and S. H. Moon, *Environ. Prog. Sustainable Energy*, 2019, **38**, 451–456.

201 M. C. Campa, D. Pietrogiacomi, C. Catracchia, S. Morpurgo, J. Olszowka, K. Mlekodaj, M. Lemishka, J. Dedecek, A. Kornas and E. Tabor, *Appl. Catal., B*, 2024, **342**, 123360.

202 E. Tabor, K. Mlekodaj, G. Sádovská, M. Bernauer, P. Klein, P. Sazama, J. Dědeček and Z. Sobalík, *Microporous Mesoporous Mater.*, 2019, **281**, 15–22.

203 E. Tabor, G. Sádovská, M. Bernauer, P. Sazama, J. Nováková, V. Fila, T. Kmječ, J. Kohout, K. Závěta and Z. Sobalík, *Appl. Catal., B*, 2019, **240**, 358–366.

204 N. Pal and A. Bhaumik, *RSC Adv.*, 2015, **5**, 24363–24391.

205 P. Verma, Y. Kuwahara, K. Mori, R. Raja and H. Yamashita, *Nanoscale*, 2020, **12**, 11333–11363.

206 Y. Qin, Z. Qu, C. Dong, Y. Wang and N. Huang, *J. Environ. Sci.*, 2019, **76**, 208–216.

207 M. Marafi and E. Furimsky, *Energy Fuels*, 2017, **31**, 5711–5750.

208 X. Wei, X.-F. Yang, A.-Q. Wang, L. Li, X.-Y. Liu, T. Zhang, C.-Y. Mou and J. Li, *J. Phys. Chem. C*, 2012, **116**, 6222–6232.

209 L. Yu, H. Hu, H. B. Wu and X. W. Lou, *Adv. Mater.*, 2017, **29**, 1604563.

210 K. Pacultová, A. Klegova, T. Kiška, D. Fridrichová, A. Martaus, A. Rokicińska, P. Kuśtrowski and L. Obalová, *Mater. Res. Bull.*, 2020, **129**, 110892.

211 M. C. Campa, A. M. Doyle, G. Fierro and D. Pietrogiacomi, *Catal. Today*, 2022, **384**, 76–87.

212 B. Bozorgi, J. Karimi-Sabet and P. Khadiv-Parsi, *Environ. Technol. Innovation*, 2022, **26**, 102344.

213 T. Umegaki, H. Katori, K. Otake, R. Yamamoto and Y. Kojima, *J. Sol-Gel Sci. Technol.*, 2019, **92**, 715–722.

214 S. Wang, B. Yan, J. Chai, T. Li, H. Yu, T. Li, P. Cao, F. Yang, X. Yuan and H. Yin, *Eur. J. Inorg. Chem.*, 2021, 2201–2210.

215 O. Muccioli, E. Meloni, S. Renda, M. Martino, F. Brandani, P. Pullumbi and V. Palma, *Processes*, 2023, **11**, 1511.

216 Z. Li, B. Li, C. Yu, H. Wang and Q. Li, *Adv. Sci.*, 2023, **10**, 2206605.

217 T. Boningari, D. K. Pappas and P. G. Smirniotis, *J. Catal.*, 2018, **365**, 320–333.

218 D. K. Pappas, T. Boningari, P. Boolchand and P. G. Smirniotis, *J. Catal.*, 2016, **334**, 1–13.

219 P. Nematollahi and M. D. Esrafili, *RSC Adv.*, 2016, **6**, 59091–59099.

220 J.-H. Lee, Y.-J. An, H. Choi, J. Lee, S.-Y. Lee and S.-J. Park, *Appl. Catal., O*, 2024, 206937.

221 M. D. Esrafili and N. Saeidi, *Appl. Surf. Sci.*, 2017, **403**, 43–50.

222 M. D. Esrafili and N. Saeidi, *Appl. Surf. Sci.*, 2018, **444**, 584–589.

223 M. D. Esrafili, *Phys. Lett. A*, 2017, **381**, 2085–2091.

224 B. Gao, J.-X. Zhao, Q.-H. Cai, X.-G. Wang and X.-Z. Wang, *J. Phys. Chem. A*, 2011, **115**, 9969–9976.

225 S. K. Tiwari, S. Sahoo, N. Wang and A. Huczko, *J. Sci.: Adv. Mater. Devices*, 2020, **5**, 10–29.

226 J. Li, M. Zhang, Q. Li and J. Yang, *Appl. Surf. Sci.*, 2017, **391**, 184–193.

227 P. Liu, X. Gu, K. Kang, H. Zhang, J. Cheng and H. Su, *ACS Appl. Mater. Interfaces*, 2017, **9**, 10759–10767.

228 T. Boningari, D. K. Pappas and P. G. Smirniotis, *J. Catal.*, 2018, **365**, 320–333.

229 M. D. Esrafili and N. Saeidi, *Appl. Surf. Sci.*, 2017, **403**, 43–50.

230 M. D. Esrafili and S. Heydari, *Mol. Phys.*, 2020, 1–8, DOI: **10.1080/00268976.2020.1759830,**.

231 M. D. Esrafili, *Phys. Lett. A*, 2017, **381**, 2085–2091.

232 M. D. Esrafili and S. Heidari, *Chem. Phys. Lett.*, 2019, **725**, 52–58.

233 J. Sun, L. Wang, L. Zhang, Y. Zhao, Y. Chi, H. Wang, C. Li, J. Liu and J. Liu, *ACS Appl. Energy Mater.*, 2021, **4**, 8496–8505.

234 X. Liu and L. Sheng, *Mater. Today Commun.*, 2021, **28**, 102585.

235 G. Fan, Q. Wang, H. Xu, X. Wang, X. Tu and X. Chu, *Appl. Surf. Sci.*, 2021, **544**, 148776.

236 Y. Xiong, Y. Zhao, W. Shan, X. Feng, J. Cui, Z. Lou, G. Shao, M. Dong and H. Yu, *Chemosphere*, 2022, **303**, 135257.

237 Y. Xiong, Y. Zhao, X. Qi, J. Qi, Y. Cui, H. Yu and Y. Cao, *Environ. Sci. Technol.*, 2021, **55**, 13335–13344.

238 E. Meloni, M. Martino, S. Renda, O. Muccioli, P. Pullumbi, F. Brandani and V. Palma, *Catalysts*, 2022, **12**, 1405.

239 X. Guan, H. Asakura, R. Han, S. Xu, H.-X. Liu, L. Chen, Z. Yao, J. H. C. Yan, T. Tanaka and Y. Guo, *ACS Catal.*, 2023, **13**, 13816–13827.

240 A. Hassanpour, M. Kamel, S. Ebrahimiasl, A. G. Ebadi, S. Arshadi and Z. Ghulinezhad Ahangari, *J. Mol. Model.*, 2022, **28**, 1–14.

241 X. Hu, E. Zhang, W. Li, L. Wu, Y. Zhou, H. Zhang and C. Dong, *Appl. Sci.*, 2022, **12**, 5034.

242 X. Tan, S. Qi, G. Cheng, C. Yi and B. Yang, SSRN, 2023, preprint, DOI: **10.2139/ssrn.4470798**.

243 M. Derdare, A.-G. Boudjahem and M. Boulbazine, *Struct. Chem.*, 2022, **33**, 2043–2062.

244 M. D. Esrafili, S. Asadollahi and S. Heydari, *J. Mol. Graphics Modell.*, 2019, **89**, 41–49.

245 A. A. Khan, M. D. Esrafili, F. Ali, R. Ahmad and I. Ahmad, *J. Mol. Graphics Modell.*, 2022, **114**, 108186.

246 P. Li, T. Zhang, H. Sun, Y. Gao, Y. Zhang, Y. Liu, C. Ge, H. Chen, X. Dai and X. Zhang, *Nano Res.*, 2022, **15**, 3001–3009.

247 J. Qi, X. Qi, Y. Pan, J. Cui, Y. Xiong, W. Shan and H. Yu, *Appl. Surf. Sci.*, 2023, **611**, 155657.

248 Y. Bai, Y. Hou, Y. Guo, N. Xiang, X. Han, H. Wang, Z. Wu and Z. Huang, *J. Colloid Interface Sci.*, 2022, **616**, 55–66.

249 Z. Liu, H. Wang, Y. Gao and J. Zhao, *Molecules*, 2023, **28**, 4485.

250 M. D. Esrafili and B. Nejadebrahimi, *Chem. Phys. Lett.*, 2019, **716**, 11–16.

251 X. Dai, Y. Cheng, T. Liu and L. Mao, *Energy Fuels*, 2024, **38**(11), 9262–9279.

252 T. Das, B. K. Sharma, A. K. Katiyar and J.-H. Ahn, *J. Semicond.*, 2018, **39**, 011007.

253 A. Akça, O. Karaman and C. Karaman, *ECS J. Solid State Sci. Technol.*, 2021, **10**, 041003.

254 X. Liu and L. Sheng, *Adv. Theory Simul.*, 2023, **6**, 2200680.

255 R. Gholizadeh, Y.-X. Yu and Y. Wang, *Appl. Surf. Sci.*, 2017, **420**, 944–953.

256 M. D. Esrafili, *Chem. Phys. Lett.*, 2018, **708**, 94–99.

257 M. D. Esrafili, *Chem. Phys. Lett.*, 2018, **705**, 44–49.

258 M. Vakili, R. Gholizadeh, A. Ghadi, E. Salmasi and M. Sinnokrot, *J. Mol. Graphics Modell.*, 2020, **101**, 107752.

259 Z. Liu, X.-r Cheng, Y.-m Yang, H.-z Jia, B.-q Bai and L. Zhao, *Materials*, 2019, **12**, 2611.

260 I. Majeed, U. Manzoor, F. K. Kanodarwala, M. A. Nadeem, E. Hussain, H. Ali, A. Badshah, J. A. Stride and M. A. Nadeem, *Catal. Sci. Technol.*, 2018, **8**, 1183–1193.

261 L. Hu, J. Yan, C. Wang, B. Chai and J. Li, *Chin. J. Catal.*, 2019, **40**, 458–469.

262 K. U. Sahar, K. Rafiq, M. Z. Abid, U. ur Rehman, A. Rauf and E. Hussain, *React. Chem. Eng.*, 2023, **8**, 2522–2536.

263 I. Troppová, M. Šihor, M. Reli, M. Ritz, P. Praus and K. Kočí, *Appl. Surf. Sci.*, 2018, **430**, 335–347.

264 D. Ma, X. Cao and Z. Cao, *J. Phys. Chem. C*, 2023, **127**, 5800–5809.

265 M. D. Esrafili, *Chem. Phys. Lett.*, 2018, **708**, 94–99.

266 M. D. Esrafili and E. Vessally, *Surf. Sci.*, 2018, **667**, 105–111.

267 R. Gholizadeh, Y.-X. Yu and Y. Wang, *Appl. Surf. Sci.*, 2017, **420**, 944–953.

268 M. D. Esrafili, F. Mohammadian-Sabet and P. Nematollahi, *RSC Adv.*, 2016, **6**, 64832–64840.

269 P. Praus, L. Svoboda, M. Ritz, I. Troppová, M. Šihor and K. Kočí, *Mater. Chem. Phys.*, 2017, **193**, 438–446.

270 K. Kočí, M. Reli, I. Troppová, M. Šihor, J. Kupková, P. Kustrowski and P. Praus, *Appl. Surf. Sci.*, 2017, **396**, 1685–1695.

271 M. Reli, L. Svoboda, M. Šihor, I. Troppová, J. Pavlovský, P. Praus and K. Kočí, *Environ. Sci. Pollut. Res.*, 2018, **25**, 34839–34850.

272 K. Kočí, M. Reli, I. Troppová, M. Šihor, T. Bajcarová, M. Ritz, J. Pavlovský and P. Praus, *Catalysts*, 2019, **9**, 735.

273 M. Reli, I. Troppová, M. Šihor, J. Pavlovský, P. Praus and K. Kočí, *Appl. Surf. Sci.*, 2019, **469**, 181–191.

274 P. Praus, J. Lang, A. Martaus, L. Svoboda, V. Matějka, M. Kormunda, M. Šihor, M. Reli and K. Kočí, *J. Inorg. Organomet. Polym. Mater.*, 2019, **29**, 1219–1234.

275 V. Matějka, M. Šihor, M. Reli, A. Martaus, K. Kočí, M. Kormunda and P. Praus, *Mater. Sci. Semicond. Process.*, 2019, **100**, 113–122.

276 P. Maitarad, A. Junkaew, V. Promarak, L. Shi and S. Namuangruk, *Appl. Surf. Sci.*, 2020, **508**, 145255.

277 S. Su, J. Ma, Z. Liu, D. Holiharimanana and H. Sun, *Catalysts*, 2023, **13**, 578.

278 M. D. Esrafili and S. Heydari, *Mol. Phys.*, 2020, **118**, e1759830.

279 X. Hu, Y. Wang, R. Wu and Y. Zhao, *Appl. Surf. Sci.*, 2021, **538**, 148157.

280 D. Masih, Y. Ma and S. Rohani, *Appl. Catal., B*, 2017, **206**, 556–588.

281 J. O. Ighalo, M. L. Smith, A. Al Mayyahi and P. B. Amama, *Appl. Catal., B*, 2024, 124352.

282 S. Zhao, D. Chen, N. Li, Q. Xu, H. Li and J. Lu, *J. Alloys Compd.*, 2023, **960**, 170830.

283 B. Huang, Y. F. Wu, Z. Zhang, R. Chen, G. Y. Ren, N. Zhou, N. Li and Y. Qian, *J. Mater. Chem. A*, 2025, **13**, 16970–16980.

284 Y.-X. Yu, *J. Colloid Interface Sci.*, 2025, 137799.

285 B. Huang, G. y Ren, R. Chen and N. Li, *Chem. Phys. Lett.*, 2025, **874–875**, 142178.

286 X. Hu, Y. Wang, Z. Ling, H. Song, Y. Cai, Z. Li, D. Zu and C. Li, *Appl. Surf. Sci.*, 2021, **556**, 149817.

287 A. Al Mayyahi, S. Sarker, B. M. Everhart, B. Tonyali, U. Yucel and P. B. Amama, *J. Phys. Chem. Solids*, 2022, **170**, 110875.

288 A. Hermawan, T. Hasegawa, Y. Asakura and S. Yin, *Sep. Purif. Technol.*, 2021, **270**, 118815.

289 A. A. Mayyahi, S. Sarker, B. M. Everhart, X. He and P. B. Amama, *Mater. Today Commun.*, 2022, **32**, 103835.

290 L. Kong, M. Wang and C.-M. L. Wu, *ACS Mater. Lett.*, 2024, **6**, 1711–1721.

291 H. D. Mai, K. Rafiq and H. Yoo, *Chem. – Eur. J.*, 2017, **23**, 5631–5651.

292 S. M. Rogge, A. Bavykina, J. Hajek, H. Garcia, A. I. Olivos-Suarez, A. Sepúlveda-Escribano, A. Vimont, G. Clet, P. Bazin and F. Kapteijn, *Chem. Soc. Rev.*, 2017, **46**, 3134–3184.

293 A. Bavykina, N. Kolobov, I. S. Khan, J. A. Bau, A. Ramirez and J. Gascon, *Chem. Rev.*, 2020, **120**, 8468–8535.

294 K. Rafiq, H. D. Mai, J. K. Kim, J. M. Woo, B. M. Moon, C. H. Park and H. Yoo, *Sens. Actuators, B*, 2017, **251**, 472–480.

295 F. Ahmad, K. Rafiq, T. Najam, E. Hussain, M. Sohail, M. Z. Abid, A. Mahmood, M. S. Javed and S. S. A. Shah, *Int. J. Hydrogen Energy*, 2023, **48**(90), 35075–35111.

296 S. Ketrat, T. Maihom, S. Wannakao, M. Probst, S. Nokbin and J. Limtrakul, *Inorg. Chem.*, 2017, **56**, 14005–14012.

297 P. Zhao, F. Qin, Z. Huang, C. Sun, W. Shen and H. Xu, *Chem. Eng. J.*, 2018, **349**, 72–81.

298 V. Paluka, T. Maihom, M. Probst and J. Limtrakul, *Phys. Chem. Chem. Phys.*, 2020, **22**, 13622–13628.

299 S. Chen, Y. Zhou, J. Li, Z. Hu, F. Dong, Y. Hu, H. Wang, L. Wang, K. K. Ostrikov and Z. Wu, *ACS Catal.*, 2020, **10**, 10185–10196.

300 H. Louis, T. C. Egemonye, T. O. Unimuke, B. E. Inah, H. O. Edet, E. A. Eno, S. A. Adalikwu and A. S. Adeyinka, *ACS Omega*, 2022, **7**, 34929–34943.

301 K. D. Vogiatzis, E. Haldoupis, D. J. Xiao, J. R. Long, J. I. Siepmann and L. Gagliardi, *J. Phys. Chem. C*, 2016, **120**, 18707–18712.

302 S. Ketrat, T. Maihom, S. Wannakao, M. Probst, S. Nokbin and J. Limtrakul, *Inorg. Chem.*, 2017, **56**, 14005–14012.

303 V. Paluka, T. Maihom, M. Probst and J. Limtrakul, *Phys. Chem. Chem. Phys.*, 2020, **22**, 13622–13628.

304 S. Chen, Y. Zhou, J. Li, Z. Hu, F. Dong, Y. Hu, H. Wang, L. Wang, K. Ostrikov and Z. Wu, *ACS Catal.*, 2020, **10**(17), 10185–10196.

305 D. Denysenko, J. Jelic, O. V. Magdysyuk, K. Reuter and D. Volkmer, *Microporous Mesoporous Mater.*, 2015, **216**, 146–150.

306 A. Dey, T. Albert, R. Y. Kong, S. N. MacMillan, P. Moënne-Loccoz, K. M. Lancaster and D. P. Goldberg, *Inorg. Chem.*, 2022, **61**, 14909–14917.

307 H. Tang, Y. He, P. Liu, J. Shao, F. Lin and Z. Wang, *Energy Fuels*, 2021, **35**, 18664–18679.

308 Z. Yao, D. Qu, Y. Guo, Y. Yang and H. Huang, *Adv. Mater. Sci. Eng.*, 2019, **2019**, 1–9.

309 N. J. Halas, P. Nordlander, H. Robatjazi, D. F. Swearer, C. Zhang, H. Zhao and L. Zhou, *US Pat.*, US10766024B2 2020.

310 D. F. Swearer, H. Zhao, L. Zhou, C. Zhang, H. Robatjazi, J. M. P. Martirez, C. M. Krauter, S. Yazdi, M. J. McClain and E. Ringe, *Proc. Natl. Acad. Sci. U. S. A.*, 2016, **113**, 8916–8920.

311 K. Rafiq, I. Sadia, M. Z. Abid, M. Z. Waleed, A. Rauf and E. Hussain, *ACS Biomater. Sci. Eng.*, 2024, **10**, 7268–7313.

312 R. Nava, B. Pawelec, P. Castaño, M. C. Álvarez-Galván, C. V. Loricera and J. L. G. Fierro, *Appl. Catal., B*, 2009, **92**, 154–167.

313 G. J. Kubas, *Chem. Rev.*, 2007, **107**, 4152–4205.

314 B. Kim, Z. Li, B. D. Kay, Z. Dohnálek and Y. K. Kim, *J. Phys. Chem. C*, 2014, **118**, 9544–9550.

315 S. Royer, D. Duprez, F. Can, X. Courtois, C. Batiot-Dupeyrat, S. Laassiri and H. Alamdari, *Chem. Rev.*, 2014, **114**, 10292–10368.

316 I. Fechete, Y. Wang and J. C. Védrine, *Catal. Today*, 2012, **189**, 2–27.

317 T. Selvaraj, P. Aghalayam and J. J. Varghese, *Ind. Eng. Chem. Res.*, 2024, **63**, 6591–6599.

318 E. Winter, *J. Catal.*, 1969, **15**, 144–152.

319 E. V. Kondratenko and J. Pérez-Ramírez, *J. Phys. Chem. B*, 2006, **110**, 22586–22595.

320 S. Subramanian and C. Swamy, *Catal. Lett.*, 1995, **35**, 361–372.